UNIVERSITEIT VAN PRETORIA
UNIVERSITY OF PRETORIA
YUNIBESITHI YA PRETORIA

MEASURING AND MODELLING OF PYROTECHNIC TIME DELAY ELEMENT BURN RATES

---

by

Yolandi Cecile Montgomery

Thesis submitted in partial fulfilment of the requirements for the degree of

Doctor of Philosophy

in

Chemical Engineering

In the

Department of Chemical Engineering

Faculty of Engineering, Built Environment and Information Technology

University of Pretoria

Pretoria

February 2018

MEASURING AND MODELLING OF PYROTECHNIC TIME DELAY ELEMENT BURN RATES

Author: Yolandi C. Montgomery

Supervisor: Professor Walter W. Focke

Department: Department of Chemical Engineering

University: University of Pretoria

Degree: PhD (Chemical Engineering)

ABSTRACT

Pyrotechnic time delay elements are used in non-electric detonators for blasting operations in the mining and military industries. The improvement of time delay element consistency has been limited by inconsistent measurement techniques, insufficient mathematical models describing the delay element behaviour and physical limitations of the experimental preparation and testing of delay elements. The first part of the investigation focused on finding a solution to the first problem. Currently several techniques have been published and used to measure the burn rates of pyrotechnic delay elements, but each has its own set of problems and limitations. A new method was developed to measure the burn rates of the delay elements using an infrared camera. The average burn rates for a range of compositions were compared to the industrial technique of assembling full detonators and to the commonly used laboratory technique of using two thermocouples. The results showed that the infrared camera method measured slightly lower burn rates than the commercial detonator tests, but higher values than the thermocouple technique. The standard deviations were of the same order in size as those with the full detonators. The thermocouple technique had very large standard deviations, which indicated that the thermocouples used were too large and did not have a fast enough response time.

The infrared camera method was found to be reliable for measuring the burn rates of pyrotechnic delay elements.

The infrared camera method not only provides a way of measuring the average burn rates, but also gives continuous temperature profile data. The temperature profiles measured for slow-burning delay compositions were found to be fully developed and therefore the average burn rates measured can be assumed to be reliable. The fast-burning delay compositions, on the other hand, had temperature profiles that were not fully developed. These compositions therefore required further modelling in order to confirm that the burn rates measured were accurate. This led to the second part of the investigation, which was to develop a full three-dimensional model of the entire delay element structure. A model was developed using COMSOL Multiphysics software for the slow-burning delay composition of Mn + Sb_2O_3. The reaction equation was determined through Ekvi thermodynamic simulations, and actual temperature-dependent properties from the literature were used as far as possible. The kinetic parameters were fitted to the infrared camera data to obtain the best-fit kinetics through a least squares method. The Ekvi thermodynamic simulations of the Mn + Sb_2O_3 composition revealed the formation of a MnSb alloy. This was confirmed using X-ray diffraction analysis of the product residues. The redox reaction of Mn + Sb_2O_3 was found to undergo a second intermetallic reaction for fuel-rich compositions.

The model was also applied to the fast-burning delay composition of Si + Pb_3O_4. Good agreement between the model and the infrared camera temperature profiles was obtained. The element wall material was found to have a significant impact on the burn rate only when the material thermal conductivity was very high and the volumetric heat capacity was very low. Preheating resulted only for tube materials of diamond and pyrolytic graphite, but no radial combustion was observed. External heat transfer parameters did not have any significant effect on the average burn rate. It was concluded that the ambient temperature, core diameter, volume fraction solids, wall thickness and heat of reaction are the factors that most significantly influence the average burn rate of the compositions.

KEYWORDS: pyrotechnic, delay element, burn rate, numerical model, intermetallic

ACKNOWLEDGEMENTS

I would first and foremost like to thank Professor Walter W. Focke for his contributions and support throughout the study. I would also like to thank him for being the best mentor that any young mind could ask for. His critical thinking and enthusiasm for research has encouraged me to make the world a better place through science.

I would also like to thank my two colleagues Ollie Del Fabbro and Dr Shepherd Tichapondwa. Our lengthy discussions trying to understand the behaviour of the unpredictable pyrotechnic reactions broadened my understanding of the field of pyrotechnics.

Maria Atanasova, Wiebke Grote (XRD) and Isbe van der Westhuizen (TGA) are thanked for their technical assistance.

Mr Carel Coetzee of the Department of Material Sciences and Metallurgical Engineering is greatly thanked for his support and giving access to the JEOL JSM-IT300LV scanning electron microscope (SEM).

I greatly appreciate the financial and technical support provided by AEL Mining services throughout this study. Financial support from the THRIP programme of the Department of Trade and Industry and the National Research Foundation is gratefully acknowledged.

I would like to thank every author cited in this thesis. Without their research, there would have been no basis for this work.

I am grateful for the support of my parents – their guidance helped me to become an independent thinker.

I would also like to thank my sister, who believes I can change the world, and because of her faith in me I can.

Lastly, I would like to thank my friend, partner and husband, Thomas, for giving me the technical support to overcome every obstacle that this study presented and for his unlimited emotional support to achieve my dreams.

CONTENTS

LIST OF TABLES

LIST OF FIGURES

LIST OF SYMBOLS AND ABBREVIATIONS

Abbreviations

2D	Two-dimensional
3D	Three-dimensional
BET	Brunauer-Emmett-Teller
IR	Infrared
LAN	Local area network
SEM	Scanning electron microscope
Std	Standard deviation
TGA	Thermogravimetric analysis
TMD	Theoretical maximum density
wt.	Weight
XRD	X-ray diffraction

Symbols	**Description**	**Units**
A_0	Effective pre-exponential constant for the diffusion coefficient	m^2s^{-1}
B	Diffusion constant	$s^{-1}K^{-n}$
C	Concentration	mol m^{-3}
C_p	Heat Capacity	J $kg^{-1}K^{-1}$
D	Diameter	m
D_{IR}	Distance between sample and IR camera	mm
d	Particle size	m
E_a	Activation energy	J mol^{-1}
E_D	Apparent activation energy for the diffusion coefficient	J mol^{-1}
FOV	Field-of-view of IR camera	°
H_{rx}	Molar heat of reaction	J mol^{-1} oxidant
h_{rx}	Mass heat of reaction	J kg^{-1} mixture

h_{conv}	Convective heat transfer coefficient	$W\ m^{-2}K^{-1}$
$\mathfrak{H}$	Relative humidity	-
i	Time step identification	-
J	Mathematical counting index	-
k	Reaction constant	
	(for autocatalytic reactions of orders m and n)	$mol^{-(n+m-1)}m^{3(n+m-1)}s^{-1}$
	(for reaction kinetics without reaction orders)	s^{-1}
k_o	Arrhenius constant	
	(for autocatalytic reactions of orders m and n)	$mol^{-(n+m-1)}m^{3(n+m-1)}s^{-1}$
	(for reaction kinetics without reaction orders)	s^{-1}
L	Latent heat	$J\ kg^{-1}$
ℓ	Length	m
ℓ_c	Characteristic length	m
m, n	Reaction orders	-
N	Constant equal to the reaction order	-
n_d	Normal direction component	-
P	Proportionality constant	-
Pixel	IR camera pixel dimensions	-
Q	Heat generated	$W\ m^{-3}$
q	Heat loss coefficient	$Wm^{-3}K^{-1}$
R	Universal gas constant	$J\ mol^{-1}K^{-1}$
r	Radius	mm
r_i	Reaction rate	$mol\ m^{-3}s^{-1}$
T	Temperature	K
t	Time	s
u	Linear burn rate	mms^{-1}
V	Volume	m^3
z	Filter order	

Greek

α	Reaction conversion	-
ε	Emissivity	-
δ	Pulse function	-
λ	Thermal conductivity	W $m^{-1}K^{-1}$
ρ	Density	kg m^{-3}
σ	Stefan-Boltzmann constant	W $m^{-2}K^{-4}$
τ_{wall}	Wall thickness	m
φ_s	Volume fraction solids	-
ω	Frequency	Hz

Subscripts

50	Volumetric mean for particle size
A	Component A
amb	Ambient conditions
B	Component B
C	Component C
c	Maximum combustion temperature
comp	Delay composition properties
D	Component D
eq	Equivalent properties
ext	External layer
f	Fluid properties
hd	Horizontal pixel width
hn	Number of pixels in horizontal direction
i	Pre-reaction conditions (t=0)
inside	Inside diameter
L	Lateral
m	Melting point
max	Maximum condition

outside	Outside diameter
p	Mean
packing	Packing density
paint	Paint layer properties
s	Solid powder properties
sampling	Sampling conditions

1 INTRODUCTION

1.1 BACKGROUND

The word ‘pyrotechnics’ is most commonly associated with fireworks and special effects created in movies. However, this is only a small part of the world of pyrotechnics. Pyrotechnics is differentiated from high explosives by the mechanism through which the reaction is sustained. In pyrotechnics the reaction propagation is sustained by a thermal combustion wave, whereas in high explosives the detonation leads to a shock wave which sustains the reaction propagation (Kosanke et al., 2004). In the mining industry, pyrotechnics are used to initiate the explosives used to displace rock material from the surface or from underground rock formations (Beck and Flanagan, 1992). When referring to explosions, one of the concepts most often encountered is sequential blasting. Among the many applications of sequential blasting, most are still encountered in the mining industry and military applications. Sequential blasting is a term used to refer to multiple blasts triggered in a series (or chain) format (Beck et al., 1984). The main concern when dealing with sequential blasting is to detonate the consecutive blasts in an exact time sequence to achieve the desired explosive effects.

One way of achieving this time delay between blasts is to use pyrotechnic time delay elements (Beck et al., 1984, Tichapondwa et al., 2010). Pyrotechnic time delay elements are just one of the ways in which the timing sequence in sequential blasting can be achieved. Others methods include igniter cord, detonating fuse and electronic timers (Beck et al., 1984). Some of the advantages of using pyrotechnic time delays is that they are all initiated simultaneously, and therefore the line of explosive units cannot be broken by preceding units that break the cords. Pyrotechnic delay elements are also inexpensive, rugged, small and simple to use (Beck et al., 1984, Danali et al., 2010). The principle of the time delay element is that the delay composition contained in the element will burn from one side of the unit, where ignition occurs, through to the other side containing the primary explosives. This is where the explosive charge is then detonated. The time that the composition takes to burn from one side of the delay element to the other side is the length of time delay achieved (Hedger, 1983, Beck et al., 1984). The time delay between ignitions will control the fragmentation, rock break, ground vibrations, air blast noise and the amount of fly-rock (Beck and Flanagan, 1992, Beck et al., 1984, Tichapondwa et al., 2010).

It is therefore vitally important to be able to accurately predict the amount of time that the specific delay composition is required to burn from one side of the element to the other under the applied conditions.

Over the last two decades the consistency of pyrotechnic delay elements has been improved from a 10% variation in burn rate to a variation within 4% (Danali et al., 2010). Several factors influence the time delay burn rate achieved by a specific pyrotechnic delay element. These factors include ambient conditions, packing density, geometrical layout of the element, construction materials and changes in composition (Kappagantula et al., 2011, Hedger, 1983, Jakubko, 1997). The extent to which each of these factors (and other as yet unidentified factors) influence the burn rate, has not been well studied. Three factors have been identified that hinder further improvement in the accuracy of pyrotechnic time delay elements.

The first factor is the problems experienced with measuring the burn rate of the pyrotechnic composition. The industrial method currently used for measuring the burn speed of pyrotechnic delay elements has two major disadvantages. The first is that it is destructive in nature and therefore the elements cannot be analysed after testing to establish reasons for inconsistencies in the burn rates measured. The second major disadvantage is that it involves the use of primary explosives; this poses a high safety risk to the personnel performing the tests. Other techniques such as using thermocouples or high-speed cameras require physical alterations to the samples.

A second factor identified to hinder the improvement of pyrotechnic delay accuracy is the physical construction of the elements, which does not allow control of multiple variables. There is typically only one variable that can be controlled with the other parameters depending on the technique used to fill and compress the powders. This lack of control makes it difficult to independently evaluate the variables that influence the burn rates of pyrotechnic time delay elements. Improvement is further hindered by a lack of mathematical models describing the behaviour of the time delay elements in their delay element structure. The models that have been developed are limited to a narrow application in composition and geometrical shape.

1.2 AIMS AND OBJECTIVES

The aim of this study was to find solutions to the problems that were identified as hindering the improvement in the accuracy of pyrotechnic time delay burn rates. This encompassed three objectives.

The first objective of the study was to develop a method for measuring the burn rates of pyrotechnic time delay elements that would eliminate the problems experienced with other methods. Considering the other methods available for measuring the burn rates of pyrotechnic delay elements, several criteria were developed for the new method to conform to. The new method had to be non-destructive so that the samples could be analysed afterwards and reveal the reasons for the inconsistencies observed. The method should not require any physical alterations (drilling holes, changing tube materials, etc.) to the sample before testing. It should be safe to perform and give repeatable burn rate measurements comparable to those measured with the industrial technique. The method should further deliver continuous measurements throughout the test as additional information.

The second objective was to develop a numerical model of the delay element. The model should include the pyrotechnic reaction of the delay composition as well as the delay element structure.

As mentioned, there are many factors that can influence the burn rate of the pyrotechnic delay element. From this, the third objective was to use the model to evaluate and quantify the effect that all the variables have on the burn rate of the delay composition. One variable that cannot be evaluated using the model is the packing arrangement of the particles in the mixture. Since the reaction between solid fuels and solid oxidants is not yet completely understood, it cannot be modelled. This factor would therefore have to be evaluated experimentally.

1.3 OUTLINE OF THE THESIS

The thesis is presented in six chapters. Each chapter is briefly described below.

Chapter 1 provides the background to pyrotechnic time delay elements and their application as initiators of explosives in sequential blasting. The overall aims and objectives of the project are also described.

Chapter 2 gives a summary of the existing literature on pyrotechnic time delay elements. The focus of the review is placed on the measurement techniques of the burn rates of delay elements, the modelling of the delay elements and the effect of various parameters on the burn rate.

Chapter 3 describes all the methods and techniques applied in all the experimental work performed during this study. The characterisation techniques and results of all the materials are also provided in this chapter. The new method developed for measuring the burn rates is also described in Chapter 3.

Chapter 4 describes all the aspects of the modelling performed in this study. The model equations, numerical solution techniques, initiation and mesh convergence are described in detail in this chapter. A separate list of symbols is provided before Chapter 1, which gives all the symbols and units for all the equations used in the study.

Chapter 5 presents and discusses the results of all the evaluations performed. This chapter is divided into three sections. The first describes the experimental investigation into the particle packing effect on the burn rate of the delay element. The second section describes the results obtained from the evaluation of the newly developed measurement technique. A comparison between the technique developed and other techniques is also given. The third section describes the results obtained from the numerical model. The effect of various factors on the burn rate are also discussed.

Chapter 6 presents all final remarks and conclusions on the study, along with recommendations for future work.

2 LITERATURE REVIEW

2.1 PYROTECHNIC DELAY ELEMENTS

A pyrotechnic delay element is a self-contained device which consists of an inert housing (typically lead or aluminium) in which the powder delay composition is packed. One end of the delay element is connected to some form of ignition source and the other end is connected to the rest of the detonator. In a complete electric or non-electric detonator, the delay element is placed inside an additional housing (typically aluminium) where it is followed by a column of output charge (secondary and primary explosives) as shown in **Figure 2-1** (Hedger, 1983, Danali et al., 2010).

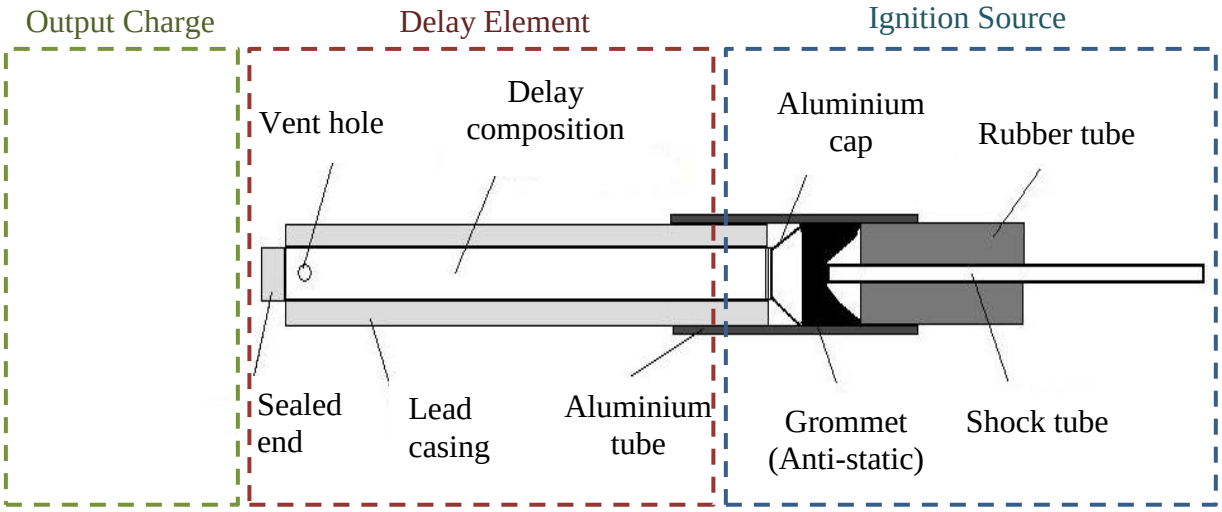

Figure 2-1: Structure of the delay element under investigation along with its position inside a non-electric detonator

2.1.1 Ignition of delay elements

Ignition of the delay composition can be achieved in several ways and various methods have been developed since the initial black powder safety fuses. Ignition was initially achieved through a simple mechanism in which a metal weight was dropped onto a stationary metal striker which then activated a percussion primer (Elischer et al., 1986). This later developed into an electric trigger that contains a fuse head which delivers a 5 A current to the delay element which then ignites the delay composition (Al-Kazraji and Rees, 1979).

From this a method progressed of using a nichrome wire (inserted into the end of the delay composition) which receives the electrical power and heats up to the ignition temperature of the composition (Kappagantula et al., 2011).

Detonator cord was (until recently) the preferred commercial initiation source. A detonator cord consists of a plastic tube filled with PETN (pentaerythritol tetranitrate) which burns at a rate of between 1 500 and 9 000 m/s (Thureson and Gladden, 1988). The current method of ignition (Swanepoel et al., 2010) is to use a shock tube in conjunction with a grommet. A shock tube consists of a small-diameter (average inner and outer diameters of 1.3 mm and 3 mm respectively) plastic (typically polyethylene) tube lined on the inside with a small amount of reactive material. The material conventionally used consists of a mixture of aluminium and HMX (Octahydro-1,3,5,7-tetranitro-1,3,5,7-tetrazocine) distributed to a load of between 15 and 30 mg per metre of shock tube (Brent and Harding, 1993). The material contained in the tube burns at a typical speed of 1 900 m/s, which is sufficient for use in current detonator devices that require a speed of above 1 500 m/s for ignition (Thureson and Gladden, 1988, Brent and Harding, 1993). Current developments in pyrotechnic device ignition are focusing on the use of light energy in the form of laser beams as a possible source of ignition. The use of a single laser ignition source would be a great move towards safer assembly and transportation as it would significantly reduce the chances of accidental ignition (Danali et al., 2010). This method has been explored by several authors (Granier and Pantoya, 2004, Ahmad and Russel, 2005, Ahmad and Russel, 2008). From these studies it can be concluded that it is a viable method of ignition, but is highly dependent on the particle sizes of the powders. Large particles can have long exposure times to ignition in the range of 6 s in comparison to nano-particles, which have short exposure times of around 12 ms (Ahmad and Russel, 2005, Ahmad and Russel, 2008, Granier and Pantoya, 2004, Danali et al., 2010). This method is expected to make its way into industrial applications once the current technological and financial constraints of the laser production, size and energy requirements are overcome.

2.1.2 Delay compositions

The characteristic component of the delay element is the delay composition, which is comprised of a mixture of fuels and oxidants in the form of powdered solids.

Several requirements have to be met by the fuel and oxidant mixture for it to be suitable for use as a confined pyrotechnic delay composition in non-electric detonators:

- The mixture should burn in a 'gasless' fashion. The amount of gas that is produced during the reaction should be less than 100 L per kg of mixture reacting (Swanepoel et al., 2010).
- It should be ignitable but must still be safe enough for stable storage and transport.
- The composition should be non-hygroscopic (Beck et al., 1984).
- It should have good flow properties for filling elements (Beck et al., 1984).
- It should be readily available and inexpensive (Beck et al., 1984).
- The burn rate of the delay element should be constant so that the delay time is linearly related to the length of the element.
- The composition should be 'green'. There should be no toxic components, heavy metals or other soil contaminants in the delay element (Danali et al., 2010, Tichapondwa et al., 2010).
- The composition should have a low temperature sensitivity.

Most of these requirements are related to the practicality of delay element preparation and usage. The main factor determining the performance of a time delay element is the burn rate at which the pyrotechnic composition reacts. This can vary from a few milliseconds to several seconds. The consistency of the burn rate is the main factor which has to be optimised in order for the delay element to detonate the explosive events in the predetermined timing sequence. Some of the commonly used fuels are listed in **Table 2-1** along with the oxidants they are commonly combined with. For the current study, both slow-burning and fast-burning delay compositions had to be evaluated to ensure that the methods and models developed are applicable over the entire range of burn rates. It was further decided to use one widely characterised composition and one novel composition. From this, the Si + Pb_3O_4 system was chosen as the fast-burning widely characterised composition. Although this composition is widely used in industry, it will in the near future likely become obsolete due to the environmental impact of heavy metals on the soil. The search for more environmentally acceptable compositions is an on-going effort in the field of pyrotechnic delay compositions. The novel slow-burning composition used was Mn + Sb_2O_3.

Table 2-1: Commonly used fuels and oxidants with which they are commonly combined in binary delay compositions

Fuel	Oxidants	References
Al	$KClO_3$, $KClO_4$, $Ba(NO_3)_2$, AlF_3, CuO, $NaClO_3$	(Laye and Charsley, 1987, Pourmortazavi et al., 2008, Vermeij et al., 2009)
B	KNO_3, MoO_3, Pb_3O_4, Bi_2O_3, PbO, Cr_2O_3, $K_2Cr_2O_7$, $Na_2Cr_2O_7$, $K_2Cr_2O_7$, $KClO_4$, SrO_2, $BaCrO_4$	(Ahmad and Russel, 2005, Ahmad and Russel, 2008, Boddington et al., 1989, Dugam et al., 1999, Li et al., 2010, Norgrove et al., 1994, Laye and Charsley, 1987, Berger, 2005)
Fe	BaO_2, SrO_2, MoO_3	(Brown et al., 1998, Laye and Charsley, 1987)
FeSi	MnO_2	(Sulacsik, 1974)
Mg	KNO_3, BaO_2, $NaNO_3$, $Sr(NO_3)_2$,$KClO_4$, CuO, $KMnO_4$	(Ahmad and Russel, 2008, Ahmad and Russel, 2005, Laye and Charsley, 1987, Pourmortazavi et al., 2008)
Mn	BaO_2, SrO_2, MnO_2, $KClO_4$, $BaCrO_4$, $PbCrO_4$, Sb_2O_5, PbO_2, CuO	(Brown et al., 1998, Drennan and Brown, 1992b, Drennan and Brown, 1992a, Drennan and Brown, 1992c, Kappagantula et al., 2011, Miklaszewski et al., 2014, Swanepoel et al., 2010, Laye and Charsley, 1987, Heiskell, 1955)
Mo	BaO_2, SrO_2	(Brown et al., 1998, Drennan and Brown, 1992b, Drennan and Brown, 1992a, Drennan and Brown, 1992c, Laye and Charsley, 1987)
Sb	$KMnO_4$	(Beck and Brown, 1986, Beck et al., 1984, Beck and Brown, 1983, Brown et al., 1998, Norgrove et al., 1994, Laye and Charsley, 1987, Tsang, 2005)
Si	Pb_3O_4, SnO_2, Fe_2O_3, KNO_3, Sb_2O_3, Bi_2O_3, Sb_6O_{13}, Cr_2O_3, MnO_2, $KMnO_4$, Na_2CrO_4, $KClO_3$, $NaNO_3$, $BaSO_4$, $Cu(SbO_2)\cdot xZn(SbO_2)_2$, $PbCrO_4$, PbO, Sb_2S_3, $K_2Cr_2O_7$	(Al-Kazraji and Rees, 1979, Al-Kazraji and Rees, 1978, Beck et al., 1984, Beck and Brown, 1986, Brown et al., 1998, Hedger, 1983, Jakubko, 1997, Jakubko and Cernoskova, 1997, Jakubko, 1999, Kalombo et al., 2007, Koch and Clement, 2007, Ricco et al., 2004, Tichapondwa et al., 2010, Tichapondwa et al., 2016, Laye and Charsley, 1987, Rugunanan and Brown, 1994, Rugunanan and Brown, 1991, Tsang, 2005)
Ta	PbO, Pb_3O_4, $PbCrO_4$, $KClO_4$	(Laye and Charsley, 1987)
Ti	MoO_3, TiN, BaO_2, $NaNO_3$, $Sr(NO_3)_2$, $KClO_4$, $KClO_3$, $BaCrO_4$	(Laye and Charsley, 1987)

TiH_2	$KClO_4$, $KClO_3$, $Ba(NO_3)_2$	(Shamsipur et al., 2013)
V	MoO_3	(Laye and Charsley, 1987)
W	$K_2Cr_2O_7$, $KClO_4$, $BaCrO_4$	(Boddington et al., 1982, Boddington et al., 1986, Boddington et al., 1989, Charsley et al., 1978, Laye and Charsley, 1987)
Zn	$KClO_4$	(Laye and Charsley, 1987)
Zr	MoO_3, Fe_2O_3, SiO_2, $KClO_4$, KNO_3, SrO_2, $BaCrO_4$, Pb_3O_4	(Laye and Charsley, 1987, Berger, 2005)

2.2 BURN RATE MEASUREMENTS

In order to accurately determine the performance of a time delay element, the burn rate has to be measured accurately. Several laboratory scale techniques have been developed to measure the average burn rate of pyrotechnic delay compositions. The first method is the commercial measurement technique in which complete delay detonators are assembled (Hedger, 1983). In this method, a timer is started when the detonator is initiated with an electric firing device and is stopped by the triggering of a photoelectric cell when the reaction in the detonator reaches its end. To determine the burn rate, the length of the delay element is then divided by the time measured between initiation and detonation. A detailed description of this method is given by Tichapondwa et al. (2010). The same method was applied extensively in laboratories to the delay elements alone because it is simple to set up and inexpensive to construct (Beck et al., 1984, Al-Kazraji and Rees, 1979, Elischer et al., 1986, Beck and Brown, 1986). This method was, however, based on the use of an electronic igniter to initiate the delay composition, which in recent years has been widely replaced by shock tubes.

A variation of this method applied when shock tubes are used, involves a sound sensor as the starting condition of the timer (Swanepoel et al., 2010, Kalombo et al., 2007). The sound trigger originates from the electric firing device used to ignite the shock tube, which emits an explosive noise when the shock tube is ignited. The optical sensor was also replaced with a thermocouple. The thermocouple is placed at the end of the delay element and a sudden peak in temperature serves as the signal to stop the timer (Swanepoel et al., 2010). A method also used in laboratory scale tests makes use of two photoelectric cells (Li et al., 2010). The first photoelectric cell starts the electronic timer when ignition occurs and the second cell stops the timer when the burning front has reached the end of the element. This requires the measurement of delay elements that are open on both sides in order to emit the light. The characteristics of an open-ended burning delay element in comparison to closed-ended burning has however not yet been quantified and could result in significant inconsistencies.

Another method developed in recent years is to use a high-speed camera to capture images of the luminescent burning of the pyrotechnic composition inside a glass tube (Kappagantula et al., 2011).

The ignition in this case is achieved by thermal stimulus of a nichrome wire connected to an external voltage source which is inserted into the powder at one end of the delay element. The high-speed camera captures images of the reacting pyrotechnic delay composition (through the glass tube walls) as it burns from one end of the element to the other. The camera is placed perpendicular to the burning direction and is also used to detect the absolute ignition time by the glowing of the nichrome wire. The variation in pixel intensity is related to the flame radiance and is assumed to be a maximum at the propagation front (Kappagantula et al., 2011). The absolute distance that the propagation front has travelled in a certain time is then used to calculate the average burn rate.

For certain evaluations, more information is required than only the 'endpoint' average burn rate. One such technique is to use a series of thermocouples to measure the temperature continuously along the length of the delay element. The thermocouples are pressed into the pyrotechnic delay composition and high-speed analogue-to-digital converters are used to capture the data. The result is that at each instance that data is captured, a temperature profile at certain points along the element length is measured. These temperature profiles can be used to calculate the average burn rate and can also yield additional information such as the heat evolution throughout the element (Boddington et al., 1986, Ricco et al., 2004, Charsley et al., 1978, Boddington et al., 1982). The data from this measurement technique is often used to fit data to numerical prediction models (Boddington et al., 1986, Boddington et al., 1989).

2.3 PYROTECHNIC REACTION MECHANISMS AND KINETICS

2.3.1 Reaction mechanisms

The mechanism by which solid particles undergo chemical reactions is a topic of much debate. Almost sixty years have passed since the book *Chemistry of the Solid State* (Garner, 1955) was published, and ever since then publications of progress made in solid-state chemistry have been scarce. Finally in 2006 a review article was published by Khawam and Flanagan (2006), in which the various solid-state theories were discussed. These, however, focused on the selection of appropriate kinetic models. Due to the large amount of phase changes present in a pyrotechnic

reaction, the mechanisms and kinetic data cannot be directly extracted. The intermediate reaction steps are typically not known and very difficult to derive.

The first step in pyrotechnic reactions is usually the decomposition of the oxide, where the release of the oxygen initiates a reaction with the fuel. This leads to heat being generated and the temperature increasing (Hedger, 1983, Tichapondwa et al., 2010). Further progression of the reaction is different for each composition. The phase transitions and products formed are analysed through thermal analysis or post-reaction product analysis. This information is then used in conjunction with phase diagrams to postulate a reaction mechanism (Tichapondwa et al., 2010, Hedger, 1983). There are a few problems that can be expected from this process. The first is that the post-reaction products that are analysed could have undergone further changes during the cooling-down phase, which results in different products than those actually formed during the reaction. Another problem that is experienced is that during thermal analysis, the temperature and pressure rises typically occur at a much slower rate. This could lead to secondary reactions forming in intermediate temperature ranges, which will not occur in the sudden exponential temperature increase of the pyrotechnic reaction. Phase diagrams of all the compositions are furthermore not readily available (Hedger, 1983, Khawam and Flanagan, 2006, Tichapondwa et al., 2010).

2.3.2 Reaction kinetics

Kinetic models are usually classified in one of two ways: according to the reaction mechanism assumed or according to the shape of the resulting isothermal curves. When looking specifically at pyrotechnics, a classification based on the shape of the isothermal curves seems more logical. Even though the mechanisms through which the reactions occur are not yet certain, the effects of temperature on the reactions are well defined. The approach followed here is therefore based on defining which kinetic models would lead to a shape expected to occur in the pyrotechnic reaction. When kinetic models are based on the shape of their isothermal curves, the shapes can be divided into four groups, namely acceleratory, deceleratory, linear or sigmoidal models (Khawam and Flanagan, 2006). Pyrotechnic reactions are expected to generally result in sigmoidal isothermal profiles and acceleratory temperature profiles (Brown, 1997).

For a mechanism to be plausible in its application to pyrotechnic systems, two criteria are used here:

i. The model must be theoretically aligned with known pyrotechnic chemistry.
ii. The model must produce temperature profiles similar to the sigmoidal and acceleratory profiles observed experimentally in pyrotechnic analysis.

The first reaction models to be considered in solid-state chemistry are the nucleation models. The first nucleation models is nucleation and nuclei growth models. In nucleation models, solid crystal structures are known to have imperfections such as impurities and surface and edge defects. Due to the reaction activation being minimised in these regions, these imperfections are assumed to be the sites of reaction nucleation. Nucleation is most commonly associated with decomposition reactions, which is not the case with pyrotechnic delay compositions. Further nucleation models, such as the Avrami-Erofeyev models and power-law models, are just nucleation models with different assumptions as to the restrictions preventing nucleation (Khawam and Flanagan, 2006). These models are not used in pyrotechnic applications as they do not allow for the fast Arrhenius-type increase in reaction rate encountered in pyrotechnics. The only nucleation-based model that has been proposed for pyrotechnic application is the autocatalytic model. The general form representing the autocatalytic nucleation is given in Equation 2–1 (Khawam and Flanagan, 2006).

$$\frac{d\alpha}{dt} = k\alpha(1-\alpha) \qquad 2\text{-}1$$

The order of the autocatalytic equation can be varied when it is required to incorporate another parameter for fitting experimental data. Even though thermal analysis and several theoretical discussions have suggested the use of an autocatalytic model, researchers have to a large extent ignored it. This is most likely due to the highly exponential nature of autocatalytic models, which would cause numerical instability in numerical integration techniques.

The next type of solid-state models to be considered are the geometrical contraction models. In geometrical contraction models it is assumed that the nucleation occurs rapidly on the surface of the crystal, and the rate at which the reaction occurs depends on how the reaction interface progresses toward the centre of the crystal (Khawam and Flanagan, 2006). When the particles have a relatively constant and fixed shape, the contraction model can be derived for the specific shape.

These models are highly dependent on the accuracy of the particle size, shape and the variation in these two parameters. In pyrotechnics, the particle sizes usually range over a distribution of sizes and almost never have well-defined and consistent particle shapes. Therefore these models are not typically used in pyrotechnic applications even though they deliver the correct form of isothermal and temperature profiles.

The third type of solid-state models to be discussed is order-based models. Order-based models are used most often due to their simplicity and because the order can be manipulated to change the shape of isothermal reaction profiles to a desired fit. Equation 2–2 below is the general equation describing order-based models (Khawam and Flanagan, 2006).

$$\frac{d\alpha}{dt} = k(1-\alpha)^n \qquad 2\text{-}2$$

The theory behind order-based models is simply that the rate at which the reaction occurs is only related to the concentration of the reactant materials. Other than the concentration, the model is only based on mathematical relations and not on physical reaction mechanisms. This model is by far the one that is the most commonly applied to numerical fitting of experimental data. Several studies have employed a simple order-based model with some success (Boddington et al., 1989, Shkadinskii et al., 1971, Boddington et al., 1982, Ivleva et al., 1983, Dunmead et al., 1989, Shkadinskii, 1971, Strunina et al., 1974, Strunina et al., 1981, Boddington et al., 1986, Swanepoel et al., 2010) to fit numerical models to temperature profiles. The main reason for using this model is its simplicity as no theoretical basis is needed to choose the reaction mechanism.

The last type of model to be discussed is the diffusion model which is particularly applicable to reactions between two solid reactants. For diffusion to occur between two solid particles, molecules must permeate through adjacent crystal lattices and is therefore controlled by mass transfer. This, however, could be overcome in pyrotechnics due to the large heat evolution during the reactions, which could reduce the product layer that forms on the interface of the reaction via phase changes (Khawam and Flanagan, 2006). Various attempts have been made to incorporate diffusion effects in solid-state reactions. One such model was proposed in a complex rate law form (Boddington et al., 1990). The model is given in Equation 2–3 below, where B represents a diffusion coefficient.

The model incorporates diffusion through the rate constant in a simple order-based model similar to that given in Equation 2–2. The mechanism is based on the idea that at the early stages of the reaction, when the temperature is still low, the reaction is governed by the Arrhenius relationship. At later stages in the reaction the rate becomes diffusion controlled by a dominating diffusion term at higher temperatures.

$$\frac{1}{k} = \frac{1}{k_o exp(-E_a/RT)} + \frac{1}{BT^n} \qquad 2\text{-}3$$

This change in dominating term between kinetics-controlled and diffusion-controlled reactions may help to explain why two different groups of activation energies are typically predicted through thermal analysis and temperature profile analysis (Boddington et al., 1990). In thermal analysis, the heating rate is low, whereas in temperature profile analysis the heating rate is significantly higher. This could indicate that at low heating rates the reaction is governed by the temperature-dependent Arrhenius relationship, whereas at high heating rates the reaction is dominated by diffusion.

The last factor related to solid state chemistry that is of major importance is the temperature dependence of the rate constant (k). The most conventional and widely used temperature dependence in reaction engineering is the apparent Arrhenius temperature dependence. The standard form of the Arrhenius equation is given in Equation 2–4 below.

$$k = k_o exp(-E_a/RT) \qquad 2\text{-}4$$

The Arrhenius equation works well for most chemical reactions due to the manipulability through the pre-exponential constant and the activation energy, which is related to the individual temperature-dependent characteristics of the reaction involved. The Arrhenius equation is widely used in pyrotechnic applications, but does pose some problems when used in conjunction with numerical solution techniques (Boddington et al., 1986, Boddington et al., 1982, Boddington et al., 1989, Shkadinskii et al., 1971, Shkadinskii, 1971, Ivleva et al., 1983, Dunmead et al., 1989, Strunina et al., 1974, Strunina et al., 1981, Swanepoel et al., 2010, Armstrong, 1990).

Due to the exponential shape of the Arrhenius equation and the high temperatures involved in pyrotechnics, the rate constant can increase extremely rapidly, and this causes great difficulty in maintaining convergence of a numerical solution technique. **Table 2-2** gives a summary of all the modelling techniques discussed in this section, along with references to where they have been applied.

2.4 MODELING OF DELAY ELEMENTS

The mathematical predictions of delay element burn rates under varying conditions have a few significant advantages. One of the major advantages is the reduction in resource requirements, which include raw materials, time and equipment. Furthermore, the great advantage of using modelling in the pyrotechnic field is specifically that the safety risks involved in experimental testing are minimised as some reliable predictions would be available to substantiate the experiment. Several researchers have attempted to various extents to derive mathematical relationships between various parameters and the burn rates of the delay compositions. A few authors have derived models for the complete combustion of the composition inside the delay element under various assumptions. The next section describes the existing models and their assumptions.

2.4.1 Analytical models

The analytical models that predict relationships between various factors and the burn rates of pyrotechnic delay elements are all based on different assumptions and take some factors into account while ignoring others completely. The simplest theory was derived by Khaikin and Merzhanov (1966), which analytically relates the burn rate of the delay composition to its physical and surrounding properties. This model is based on the assumption that the reaction only occurs in a thin reaction zone. It is further assumed that the physical properties are independent of both concentration and temperature, and that there are no phase transitions present. The temperature dependence of the reaction is assumed to act according to the standard Arrhenius equation. Equation 2–5 gives the analytical relationship between the burn rate and the various parameters influencing it, as derived by Khaikin and Merzhanov (1966). The function $g(n)$ is a function of the reaction order, which varies between 1 and 2.

$$u = \sqrt{\frac{\lambda k_o R T_c^2}{\rho E_a h_{rx} g(n)} exp(-\frac{E_a}{RT_c})} \quad 2\text{-}5$$

In 1974 an analytical model was developed by Aldushin and Khaikin (1974) based on a completely different theory. In this model, it is assumed that the composition is packed in neatly stacked layers of reactive material perpendicular to the direction of flame propagation. The reaction is assumed to take place due to a growing layer of reaction products which provides the medium for inter-diffusion to take place. Two other notable assumptions made during the development of this model are that the particles are assumed to be flat, and also that the reaction rate is governed by the parabolic law[a] and not by the standard Arrhenius relationship with an n^{th} order reaction rate. The analytical model derived from these assumptions is given in Equation 2–6 (Aldushin and Khaikin, 1974).

$$u = \sqrt{\frac{6RT_c^2}{E_D(T_c - T_i)} \frac{\lambda A_0}{\rho C_p d^2} exp(-E_D/RT_c)} \quad 2\text{-}6$$

Another model was developed almost 20 years later by Armstrong (1990) which was based on completely different assumptions and on a different reaction mechanism, but resulted in a mathematical relationship almost identical to the one previously discussed. This model is based on the theory that the two constituents present in the delay composition co-diffuse and thereby release heat by means of mixing on a molecular level to form either a solid or a liquid solution. This theory is fundamentally parallel to the classical flame theory used in gaseous combustion. In this case the reaction is governed by the mass diffusivity of the delay compositions' constituents similar to the way in which the temperature overcoming the activation energy in classic flame theory is rate limiting. The model is derived in a sequential form where the components are first assumed to be stacked parallel to the flame propagation axis and then perpendicular. From these two bounding cases, the model is derived by assuming a random packing orientation for the particles (Armstrong, 1990).

[a)] The condition where two mathematical boundaries reach their limiting values simultaneously, which in this application is the concentrations of the components (Aldushin and Khaikin, 1974).

When comparing this model to the previous model given in Equation 2–6, it can be seen that it is different only by a numerical factor. This is surprising as the model derived by Aldushin and Khaikin (1974) did not use the flat particle or parabolic law assumptions. It therefore gives more credence to the models that simply employ these two assumptions alongside their existing theories. When comparing these models with the first model by Khaikin and Merzhanov (1966), it can be seen that the relationship is also very similar. The major difference is that the first model is based simply on conductive heat transfer and the heat of reaction, whereas the other two models are based on thermal diffusivity and the thickness of the diffusion zone.

One model that differed significantly from these presented models is based on the assumption that the two solid reactants form a homogeneous liquid before reacting. The model is given in Equation 2–7 (Dunmead et al., 1989).

$$u = \sqrt{\frac{N\lambda k_o R T_c^2}{\rho h_{rx} E_a} exp(-E_a/RT_c)} \qquad 2\text{-}7$$

The method proved effective in predicting burn rates to some extent, but problems were encountered due to the model being highly dependent on the reaction order (Dunmead et al., 1989). The analytical models are also summarised in **Table 2-2**.

2.4.2 Numerical models

The propagation of the burning reaction along the length of the delay element is a transient state mechanism and therefore a time-dependent variable is always present. In the analytical models discussed previously, this time-dependent variable is eliminated through mathematical elimination and averaging. The time-varying factors would, however, give additional information that could increase the accuracy of the burn rate prediction and is therefore incorporated in numerical models of the delay element. The numerical models are based on obtaining temperature and concentration profiles along the length of the delay element over time. A temperature profile would therefore be calculated at each interval of time over the entire delay element as the reaction progresses along its length.

All the numerical models used to predict the propagation of the combustion front in pyrotechnic delay elements are based on straightforward heat balances (Beck et al., 1984, Strunina et al., 1974, Strunina et al., 1981, Ivleva et al., 1983, Boddington et al., 1986, Boddington et al., 1989, Boddington et al., 1990, Shkadinskii et al., 1971, Shkadinskii, 1971, Dunmead et al., 1989, Boddington et al., 1982, Hardt and Phung, 1973). In Mallard and Le Chatelier's theory of the propagation of the combustion of gaseous mixtures, the combustion is assumed to be propagated only by the forward conduction of heat over a small reaction zone (Beck et al., 1984). In the first numerical model, the same theory is applied to solid pyrotechnic delay compositions where only a small amount of material is assumed to be reacting in a defined reaction zone in which the heat conducted through adjacent material is at a maximum. Since most of the numerical theories developed later over time also originated from this mechanism, a graphical description of the theory is shown in **Figure 2-2** below (Beck et al., 1984). Also shown in **Figure 2-2** is a typical temperature profile that could be expected at any instant of time. The shape of this temperature profile is expected to remain constant as it moves with the reaction zone along the length of the delay element.

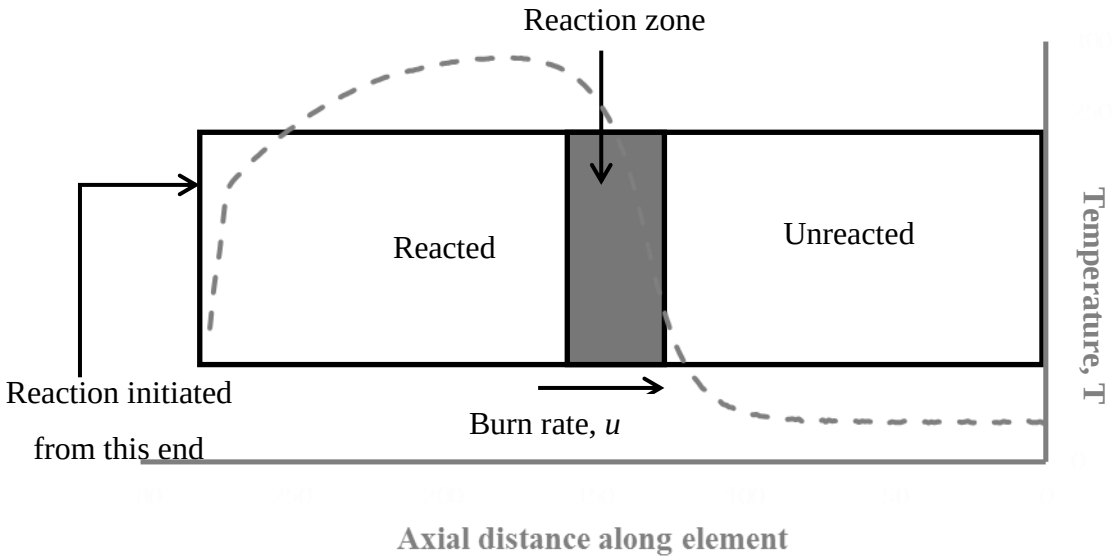

Figure 2-2: Representation of the reaction zone model along with the typical temperature profile expected along the length of the delay element (Adapted from Beck et al. (1984)).

The model is derived from a heat balance where the rate of heat generation along with the rate of heat gained by conduction is set equal to the rate of heat loss through the walls of the tube and the rate of temperature increase. The two key assumptions that are crucial in this model are that no mass transfer effects are included, and that the solid particle reaction is assumed to be without any gas formation. Other assumptions include a planar propagation waveform, a single source of heat generation and the only heat loss from the element occurring from convection and radiation (Dunmead et al., 1989). The numerical model derived from these assumptions is given in Equation 2–8 (Beck et al., 1984). The lateral heat loss coefficient (q_L) is either assumed to be constant or is completely neglected.

$$\rho h_{rx}\frac{d\alpha}{dt} + \frac{\lambda}{u^2}\frac{d^2T}{dt^2} - q_L(T - T_i) = \rho C_p\frac{dT}{dt} \qquad 2\text{-}8$$

The differential equation can now be solved numerically over time (t), through which a temperature profile (as shown in **Figure 2-2**) along the length of the delay element would be obtained for every time step taken. Although this model was simple and neglected a lot of vital information, it formed the basis for almost all numerical models that have been developed to date.

Soon after the first publication of this strategy, Boddington et al. wrote three articles (Boddington et al., 1986, Boddington et al., 1989, Boddington et al., 1990) in which they developed a numerical model to predict the average temperature across a section of the pyrotechnic using a pseudo-one-dimensional approach. The model developed, once again originating from an identical heat balance to Equation 2–8, for the first time placed emphasis on the difficulty of the numerical solution techniques used to solve this model. The problem with numerical modelling of pyrotechnics is that the solutions are highly exponential and can therefore become unstable within only a few iterations. The main reason for this is that the temperature dependence of the reaction is sharply exponential and large changes in parameters occur in only small time steps. The heat transfer effects, on the other hand, act on a much slower timescale. The integration criteria are therefore key in solving the differential equations. The approach used by Boddington et al. was to normalise the entire heat balance, thereby linearising the equation (Boddington et al., 1986, Boddington et al., 1989, Boddington et al., 1990, Boddington et al., 1982).

The only additional information added to Equation 2–8 in this case is that the fractional conversion of the reagents is not taken as a constant value. Furthermore, radial and lateral heat conduction are included in the heat loss term (Boddington et al., 1982). Due to the inadequate computing capabilities available at the time, several other researchers (Strunina et al., 1974, Strunina et al., 1981) also used the dimensionless form for solving the equations.

Another headache in these numerical models is the numerical initiation of the reaction. One such method (Shkadinskii, 1971, Shkadinskii et al., 1971) is to assume that a hot physical object is placed at the end of the element and the heat is transferred to the delay composition via conduction. There exists, however, a thermal resistance between the heated object and the adjacent material, which results in a time delay of the transfer of heat. The exact time of ignition is therefore uncertain, which adds a small amount of uncertainly to the burn rate. Another method (Ivleva et al., 1983) employed applies a heat pulse to the end of the element which then initiates the reaction. This method has been applied with major success, and only negligibly small specific heat deviations are encountered. Due to the heat pulse being applied directly to the composition, the thermal resistance problem is not present and the ignition time is easier to identify. A last study by Knapp et al. (2014) modelled the ignition and propagation of an open-flame pyrotechnic propagation by measuring the hot-spots in the combustion front. The model also evaluated the effect of the distribution of fuel and oxidant particles which lead to a very interesting model. This method can however not be used in a confined pyrotechnic setup and its application is therefore currently still limited to open-flame propagations.

The last consideration when using numerical models is the method by which the model is fit to temperature profile data obtained experimentally. In the first publication by Boddington et al. (1982), the authors used a least mean squares fit of 25 consecutive data points to a second-order polynomial to smooth the experimental data and then applied a 15-point quadratic fit to obtain the first and second derivatives for the numerical model. In the later publications they used several different iterative numerical integration techniques, which all proved successful in numerically integrating the models and were shown to identify true minima for residuals (Boddington et al., 1986, Boddington et al., 1990, Boddington et al., 1989).

The major problem experienced by all the authors is that the numerical methods are undeniably dependent on the reaction kinetics. Almost all the authors used an order-dependent rate equation due to its simplicity, even though it might not represent the correct reaction mechanism (Strunina et al., 1981, Boddington et al., 1989, Strunina et al., 1974, Boddington et al., 1986, Shkadinskii et al., 1971, Shkadinskii, 1971, Ivleva et al., 1983, Dunmead et al., 1989).

Another method of obtaining temperature profile information was proposed through which the temperature profile at a single point was measured in order to fit kinetic parameters (Boddington et al., 1990). The kinetic parameters were then used in a numerical model to predict average burn rates. The method consisted of placing an inert septum with the same radius as the delay element in the middle of the delay element. The temperature of the surface of the septum was then measured by infrared pyrometry where an analogue signal is provided proportional to the temperature. The method was found to be suitable for determining design criteria for through-barrier systems, but the kinetic information is not sufficient as a standalone technique for measuring the burn rate and should be coupled with a method for measuring temperature profiles directly (Boddington et al., 1990).

Table 2-2: Summary of mathematical models describing pyrotechnic delay elements

Key assumptions	Mathematical description	References
Analytical Models		
1) Reaction occurs in thin reaction zone only 2) Physical properties not dependent on concentration or temperature 3) Arrhenius temperature dependence	$u = \sqrt{\frac{\lambda k_o R T_c^2}{\rho E_a h_{rx} g(n)} exp(-E_a/RT_c)}$	(Khaikin and Merzhanov, 1966, Swanepoel et al., 2010)
1) Composition stacked in neat layers 2) Growing layers of products provide medium for diffusion 3) Particles are flat and reaction rate is governed by parabolic law 4) Arrhenius temperature dependence	$u = \sqrt{\frac{6RT_c^2}{E_D(T_c - T_i)} \frac{\lambda A_0}{\rho C_p d^2} exp(-E_D/RT_c)}$	(Aldushin and Khaikin, 1974, Armstrong, 1990)
1) Solid reactants melt and form homogeneous liquid mixture 2) Order-based kinetic reactions 3) Arrhenius temperature dependence	$u = \sqrt{\frac{N\lambda k_o R T_c^2}{\rho h_{rx} E_a} exp(-E_a/RT_c)}$	(Dunmead et al., 1989)
Numerical Models		
1) Reaction occurs in thin reaction zone only and mass transfer effects are neglected 2) Gasless reactions with planar propagation front 3) Single heat source with heat loss through convection and radiation only	$\rho h_{rx} \frac{d\alpha}{dt} + \frac{\lambda}{u^2} \frac{d^2T}{dt^2} - q_L(T - T_i) = \rho C_p \frac{dT}{dt}$	(Beck et al., 1984, Boddington et al., 1982, Boddington et al., 1986, Boddington et al., 1989, Boddington et al., 1990, Dunmead et al., 1989, Strunina et al., 1974, Strunina et al., 1981, Ivleva et al., 1983, Shkadinskii et al., 1971, Shkadinskii, 1971, Hardt and Phung, 1973)
Reaction Kinetics		
Autocatalytic reaction kinetics	$\frac{d\alpha}{dt} = k\alpha(1 - \alpha)$	(Khawam and Flanagan, 2006)
Order-based reaction kinetics	$\frac{d\alpha}{dt} = k(1 - \alpha)^n$	(Swanepoel et al., 2010, Boddington et al., 1982, Boddington et al., 1986, Boddington et al., 1989, Dunmead et al., 1989, Strunina et al., 1974, Strunina et al., 1981, Ivleva et al., 1983, Shkadinskii et al., 1971, Shkadinskii, 1971, Khawam and Flanagan, 2006)
Temperature-dependent Reactions		
Arrhenius relationship	$k = k_o exp(-E_a/\mathrm{RT})$	(Boddington et al., 1986, Boddington et al., 1982, Boddington et al., 1989, Shkadinskii et al., 1971, Shkadinskii, 1971, Ivleva et al., 1983, Dunmead et al., 1989, Strunina et al., 1974, Strunina et al., 1981, Swanepoel et al., 2010, Armstrong, 1990)
Temperature and diffusion-based dependency	$\frac{1}{k} = \frac{1}{k_o \exp(-E_a/RT)} + \frac{1}{BT^n}$	(Boddington et al., 1990)

2.5 FACTORS AFFECTING BURN RATES

Several factors have been identified that can affect the burn rate of pyrotechnic delay elements. Very few of these factors have been quantified and in most cases only qualitative trends have been identified. This section discusses the current literature on the factors affecting the burn rates of pyrotechnic delay elements.

2.5.1 Ambient temperature

The ambient temperature was identified early on as a factor that has an effect on the burn rate of pyrotechnic delay elements. However, to date very few studies have been conducted to determine the extent of this effect. The first study to determine the relationship between the burn rate and the ambient temperature was conducted by Elischer et al. (1986), where the burn rates were experimentally measured at three temperatures, namely 60 °C, ambient and -40 °C. A decrease in the burn rate was observed when the ambient temperature decreased. The burn rate was found to change approximately 15% for a 50 °C change in ambient temperature. Another experimental study conducted by Li et al. (2010) found that a decrease in the ambient temperature caused a decrease in burn rate by between 3.1% and 8.2% for a 50 °C decrease in temperature depending on the composition. It was found that the burn rate changed linearly with ambient temperature and also that the amount of fuel used played a significant role on the composition of B + Pb_3O_4. Jakubko (1997) evaluated the effect of ambient temperature on the Si + Pb_3O_4 composition and found an 8.52 % increase in burn rate for a 50 °C increase in ambient temperature.

A numerical study was conducted by Boddington et al. (1989) to investigate this effect and the results agreed with the finding of experimental studies that an increase in ambient temperature by 50 °C would result in burn rate increases of about 9.7%. The study did, however, result in a less linear relationship than measured in the other two studies. These results are all consistent with what can be expected from Equation 2–8. From Equation 2–8 it can be seen that at higher ambient temperatures the convection and radiation heat transfer rate would decrease due to a lower temperature gradient. This would increase the temperature inside the element, resulting in faster burn rates. The reaction rate would be further increased by a higher rate constant according to the Arrhenius relationship in Equation 2–4.

2.5.2 Composition

The effect of varying the ratio of fuel and oxidant in binary mixtures is well-studied – extensive composition studies have been done on a large number of delay compositions (Kappagantula et al., 2011, Brown et al., 1998, Swanepoel et al., 2010, Al-Kazraji and Rees, 1979, Drennan and Brown, 1992b, Ricco et al., 2004, Kalombo et al., 2007). Almost all the compositions follow a trend where an increase in the amount of fuel added causes an increase in the burn rate up to a certain maximum burn rate, after which further increase in the amount of fuel leads to a reduction in the burn rate. The burn rates tend to reach a maximum when the fuel content is just above or below the stoichiometric ratio, depending on the composition. This is, however, not always true for compositions with metal fuels. Due to the high thermal conductivity and diffusivity of the solid metal, the energy transfer through the pyrotechnic composition is much more efficient. This increases the heat transfer between solid particles and thereby also the burn rate propagation.

2.5.3 Particle size of the reactant

The effect of the particle size of the reactant on the burn rate of delay compositions is one of the factors that has also been identified to have an effect on the burn rate of pyrotechnic delay elements. The reaction between two solid pyrotechnic particles is assumed by most researchers to occur by means of mass transfer or diffusion of the species through the product layer formed in order to attain contact between the particles (Kappagantula et al., 2011, Shimizu and Hao, 1997, Boddington et al., 1990). The theory regarding the effect of particle size is based on the number of contact points between the fuel and the oxidant particles. When considering the unreacted core model, and from classical combustion theory, an increase in the number of contact points and an increase in the surface-to-volume ratio should decrease the mass transport distance ratios, and thereby increase the burn rate of the composition (Shimizu and Hao, 1997, Kappagantula et al., 2011). One of the main problems experienced in predicting the effect of particle contact points on the burn rate is that there is no reliable method of calculating the number of contact points between different particles. Studies conducted on the estimation of contact points have shown that the Hao-Tanaka model delivers the best predictions for the number of contact points in binary solid particle mixtures. The Hao-Tanaka model is based on statistical predictions of the random packing of spherical particles (Shimizu and Hao, 1997).

One interesting finding is that in all the studies conducted on particle size effects, the size of the fuel particles was varied and not the size of the oxidant particles. Only one study by Dugam et al. (1999) touched on the effect of the oxidant particle size, but concentrated more on the effect of the size distribution on the mixing capabilities. The main studies conducted on varying the fuel particle size used Si as the fuel (Ricco et al., 2004, Kalombo et al., 2007, Al-Kazraji and Rees, 1979, Hedger, 1983). Since Si has long been the fuel of choice, a lot of research has gone into evaluating the different sized Si particles. Commercial Si particle sizes vary from around 0.9 μm to 75 μm, which is in the range of particle sizes investigated in the four studies.

The first study by Al-Kazraji and Rees (1979) on the effect of silicon fuel on the burn rate, was conducted using three silicon sizes (1.9 μm, 3.9 μm and 5.0 μm). Burn tests done on delay elements containing these three different sized Si particles revealed that even in this small range of sizes, a difference in burn rate of up to 360% was possible. The Si with the smallest particles burned significantly faster than the Si with the largest particles. The same effect was found in a similar study by Kalombo et al. (2007), where three different Si sizes (0.91 μm, 2.35 μm and 3.90 μm) were also tested. In this case the smallest size Si particle burned up to 500% faster than the largest Si particle size. A third study by Ricco et al. (2004), which was also conducted on three different size Si particles (1.83 μm, 3.80 μm and 11.5 μm), found a burn rate increase of up to 200% when the particle size was decreased. One extensive study by Hedger (1983) was performed on the particle size effect of Si as the fuel, where a range of nine differently sized Si powders were used to compare the burn rates. These particles ranged from 50 μm to 75 μm (with surface areas ranging between 0.08 m^2/g and 5.36 m^2/g), and it was found that there was a change in the extent of the particle size effect at some critical particle sizes. At small fuel particle sizes (high surface areas), the burn rate was independent of the fuel particle sizes, but at large particle sizes (lower surface areas) the increase in burn rate was linear to the increase in surface area.

A study was conducted which compared the burn rates of pyrotechnic delay elements published by various sources to the number of contact points as calculated using the Hao-Tanaka model (Brown et al., 1998). In some of the compositions the maximum burn rate and maximum number of contact points coincided, but in other cases the maximums were at different fuel contents (Brown et al., 1998).

This indicates that the number of fuel contact points does in fact seem to affect the burn rate, but that other factors also influence the burn rates.

In 2005 a study was performed by Bockmon et al. (2005) in which the burn rate of very loosely packed particles was evaluated. A significant increase in burn rate was observed when the particle size of both reactants was reduced from micro to nano scale. A study conducted by Granier and Pantoya (2004) on the same composition as investigated by Bockmon et al. (2005), showed that when the particles were compressed in the form of pellets the burn rate actually decreased when the particle size was decreased. The authors attributed this to the excessively large oxidation layer present on the nano-sized fuel as a result of the increased surface area, which inhibits energy propagation. Kappagantula et al. (2011) found that the compositions containing nano-sized fuel burned two times faster than the compositions containing micro-sized fuel. In this case the authors also ascribed the phenomenon to the excessively large oxidation layer present on the nano-fuel, as this resulted in excess oxygen being released during the reaction. The conclusions from these two studies are contradictory, as in both cases an oxidation layer is present on the fuel but in one scenario the burn rate increased and in the other case the burn rate decreased. This agrees with the conclusions from the study by Brown et al. (1998) that there are other factors that also influence the burn rate when particle sizes are changed.

The synthesis, characterisation and application of nanoparticles (<100 nm) in highly energetic materials are being explored in all parts of the field. The effect of implementing these nanomaterials in pyrotechnic delay elements is, however, still under investigation by various researchers in the field (Granier and Pantoya, 2004, Danali et al., 2010, Sarawadekar and Agrawal, 2008, Yagodnikov et al., 2017). However, one conclusion that has been reached is that the ignition of small nano-sized particles is much easier and faster (Granier and Pantoya, 2004).

2.5.4 Geometry and tube material

The evaluation and testing of delay elements with different geometries and tube materials is very tricky. The tube material determines the filling and pressing procedure, which is typically developed for one specific set of geometric parameters. Very few studies have been published that contain comparisons of different tube materials or geometrical dimensions.

Boddington et al. evaluated different cross-sectional areas for square channels and found an increased burn rate for larger column areas, and concluded that the cross-sectional area is the most important factor for lateral heat loss (Boddington et al., 1986, Boddington et al., 1989). The data are, however, not suitable for quantitative evaluation. In the study by Kalombo et al. (2007), both the core diameter and wall thickness were varied simultaneously in opposite directions in order to maintain a constant outside diameter. The results therefore include the effects of both variables. The resulting gradient resulted in a ± 2.3 mm/s increase in burn rate per mm increase in inside diameter.

The tube wall material also influences the radial heat loss, and would therefore be expected to influence the burn rate. Due to the economical and physical difficulties in preparing identical elements from different tube materials, almost no experimental results have been published on comparisons between wall materials. Kalombo et al. (2007) carried out comparative burn rate measurements using lead and aluminium tubes, and found a significantly slower burn rate in aluminium tubes than in lead tubes. There was, however, some difference in the wall thickness of the tubes, and furthermore the preparation methods used would have led to different packing densities. The lack of published information on the effects of these factors indicates a clear gap in the research of pyrotechnic delay elements.

3 EXPERIMENTAL

The experimental work conducted in this study is presented in three sections. The first section describes the characterisation performed on all the raw materials acquired and purchased. The materials were characterised in terms of size, shape, purity and oxidation characteristics in order to verify the expected properties. The procedure for preparing the delay compositions is also described and a detailed characterisation of the compositions is given. The compositions were evaluated using bomb calorimetry and scanning electron microscopes (SEM). The second section describes the preparation methods applied to prepare the lead and aluminium tube delay elements. The methods used to measure the burn rates of the time delay compositions are described in the third section along with the IR camera method developed.

3.1 RAW MATERIAL CHARACTERISATION

The study was conducted using 18 different raw materials. The materials are listed in **Table 3-1** along with the suppliers and material numbers used throughout the thesis.

3.1.1 X-ray diffraction (XRD)

X-ray diffraction (XRD) analysis was performed on all the raw materials in order to determine their purity. The XRD analysis was performed on a Siemens D-501 automated diffractometer using CuKα radiation (λ = 1.5406Å) operated at 40 kV and 40 mA. This apparatus is equipped with a divergence slit of 1° and a receiving slit of 0.05°. The samples were scanned from between 3 to 90° on the 2θ-scale with a counting time of 1.5 s at room temperature. The summary of the results from the XRD analysis of all the materials is given in **Table 3-1** below. The detailed diffractograms of each sample are given in Appendix A.

3.1.2 Particle size and surface area

Particle size distributions were measured using a Mastersizer Hydrosizer 2000. The Brunauer-Emmett-Teller (BET) surface area of the powders was determined using the five-point technique with a Micromeritics TriStar II instrument. A summary of the particle size results and surface area measurements for all the materials are shown in **Table 3-1**. The average particle size distributions of all the Mn samples are shown in **Figure 3-1**. From **Figure 3-1** it can be seen that all the Mn samples are in the micro range. Even the material specified as nano-particles was found to be large agglomerates of the nano-particles. This is especially true for the sample of Mn_A that has a BET surface area that is two orders in size

bigger than the other Mn samples. This is due to the very high porosity of the sample. The Mn_A sample consists of agglomerates of particles that are about 100 nm in size but has a measured particle size of 14 µm. The FESEM images of this sample as well as all the other materials are shown in Appendix B. This sample was however too oxidised (as seen in **Table 3-1**) and did not react with any oxides. The average particle size distributions for the MnO_2 and Sb_2O_3 samples are also shown in **Figure 3-2** and **Figure 3-3** respectively. The oxides were found to have much wider distributions than the metal fuels. This is mainly due to the oxide particles consisting of agglomerates of smaller particles. This is especially apparent in **Figure 3-3** for the antimony trioxides. The average distributions for the Pb_3O_4 and Si samples are shown in **Figure 3-4**.

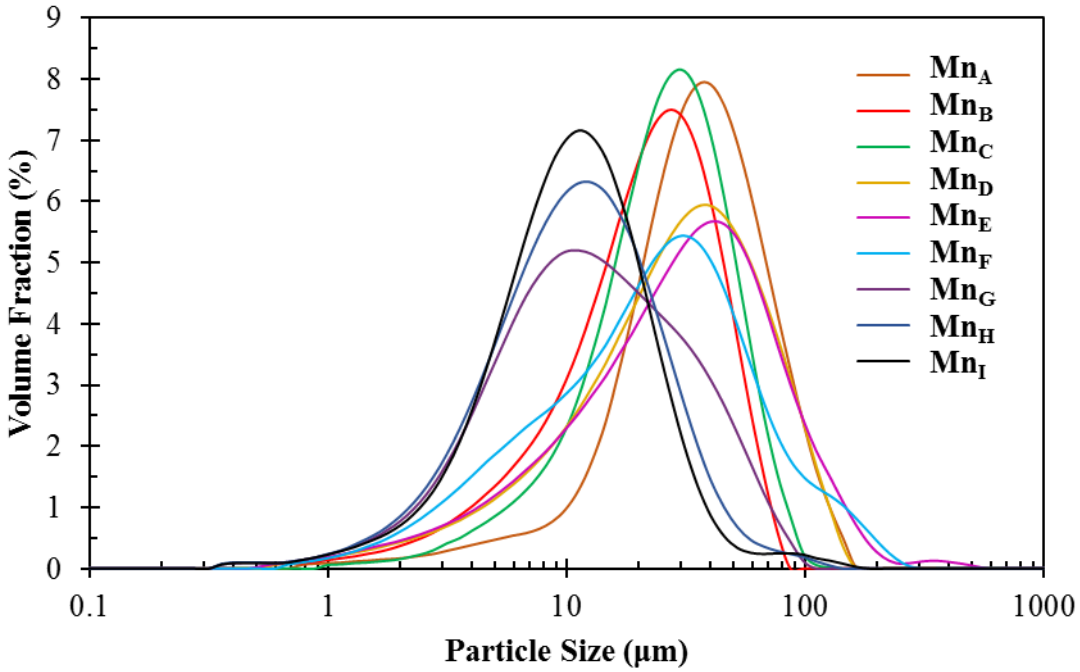

Figure 3-1: Average particle size distribution of each Mn sample

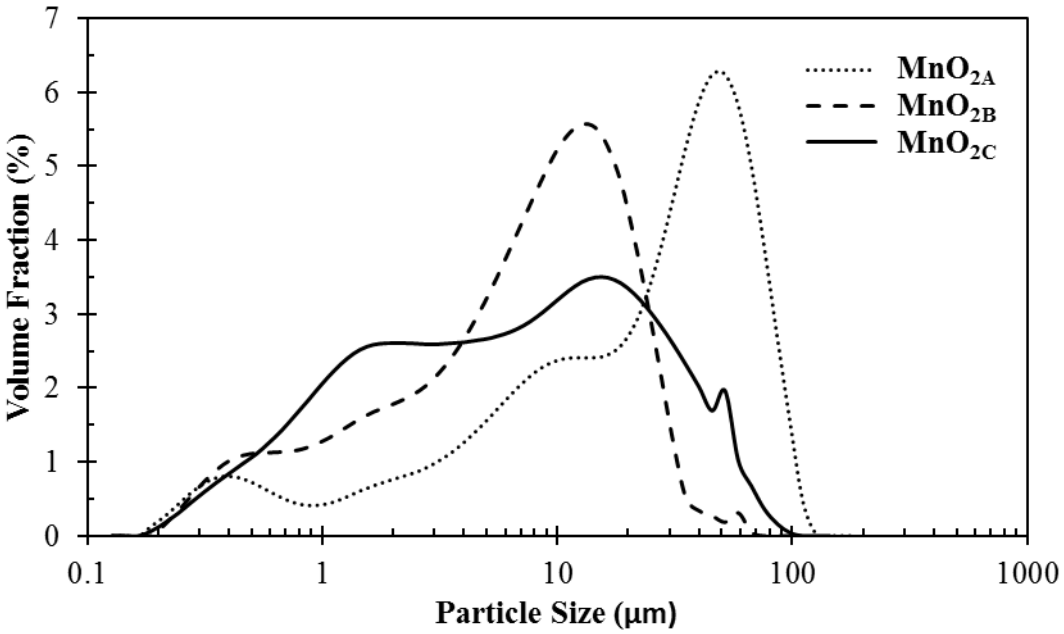

Figure 3-2: Average particle size distribution of each MnO_2 sample

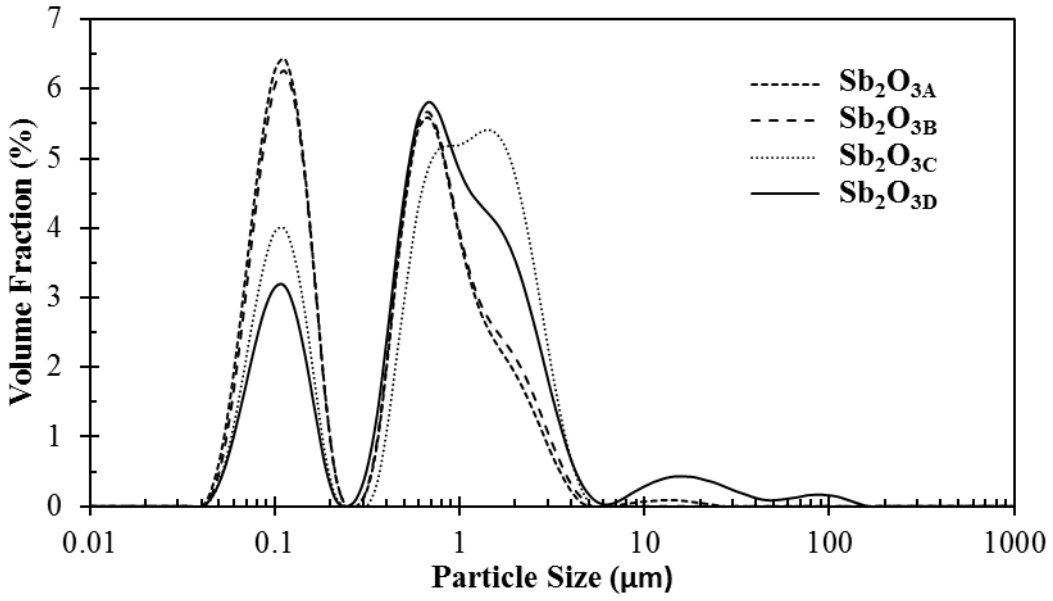

Figure 3-3: Average particle size distribution of each Sb_2O_3 sample

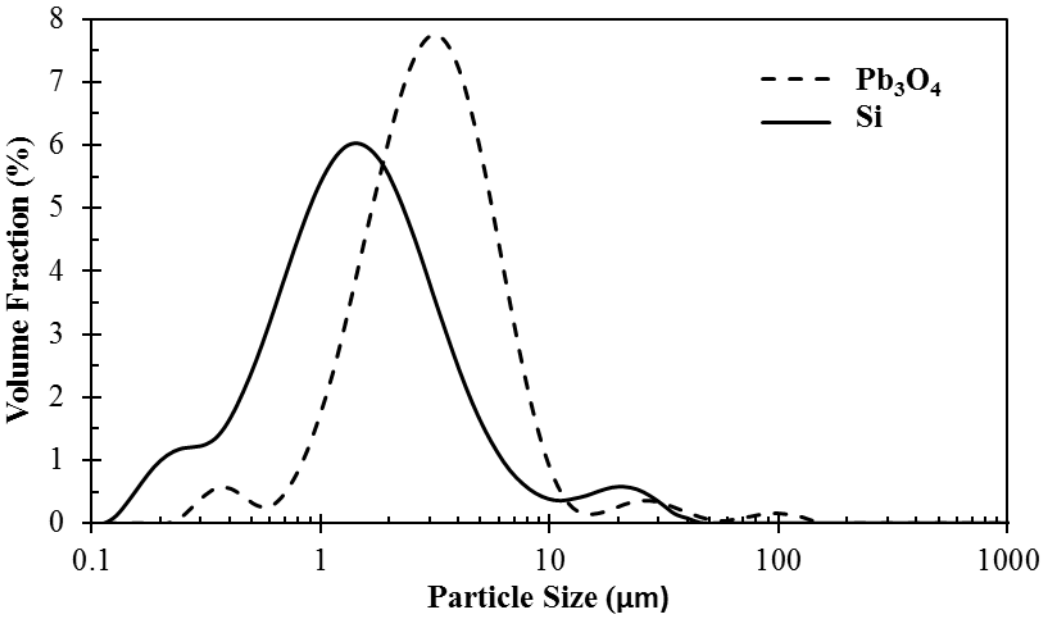

Figure 3-4: Average particle size distribution of the Pb_3O_4 and Si samples

Table 3-1: List of materials used in this study with a summary of the particle characterisation results

Material No.	**Component**	**Manufacturer**	**Manufacturer Specification**	**Composition (XRD)**	**Particle Size (d_{50} ± std, µm)**	**Surface area (BET, m^2/g)**
Mn_A	Mn	Quantum Sphere	Mn (50-80 nm)	33.67% Mn + 66.33% MnO	14 ± 0.06	28 ± 1
Mn_B	Mn	Atlantic Equipment Engineers	Mn (2 µm)	100% Mn	23 ± 0.7	0.29 ± 0.01
Mn_C	Mn	Aldrich	Mn (45 µm)	100% Mn	27 ± 0.8	0.29 ± 0.02
Mn_D	Mn	Henan Huier Nano Technology Co Ltd.	Mn (10-30 nm)	100% Mn	31 ± 4.4	0.18 ± 0.003
Mn_E	Mn	Henan Huier Nano Technology Co Ltd.	Mn (50-60 nm)	100% Mn	32 ± 4.8	0.18 ± 0.01
Mn_F	Mn	BOC Sciences	Mn (70 nm)	100% Mn	25 ± 2.7	0.38 ± 0.01
Mn_G	Mn	Manganese Metal Company	Mn (32-45 µm)	100% Mn	13 ± 0.2	0.61 ± 0.001
Mn_H	Mn	Manganese Metal Company	Mn (25-32 µm)	100% Mn	11 ± 0.09	0.65 ± 0.01
Mn_I	Mn	Manganese Metal Company	Mn (<25 µm)	100% Mn	11 ± 0.1	0.65 ± 0.003
MnO_{2A}	MnO_2	Source unknown	MnO_2 (600-800 nm)	53.47% MnO_2 + 46.53% Mn_2O_3	25 ± 0.2	12 ± 0.9
MnO_{2B}	MnO_2	Sigma Aldrich	MnO_2 (5 µm)	100% MnO_2	7.4 ± 0.80	77 ± 3

MnO_{2C}	MnO_2	Sigma Aldrich	MnO_2 (10 μm)	92.69% MnO_2 + 7.31% Mn_2O_3	6.9 ± 1	15 ± 0.4
Sb_2O_{3A}	Sb_2O_3	Aldrich	Sb_2O_3 (<250 nm)	100% Sb_2O_3	0.50 ± 0.02	3.3 ± 0.2
Sb_2O_{3B}	Sb_2O_3	Inframat Advanced Materials	Sb_2O_3 (300 nm)	100% Sb_2O_3	0.53 ± 0.01	3.1 ± 0.06
Sb_2O_{3C}	Sb_2O_3	Aldrich	Sb_2O_3 (5 μm)	100% Sb_2O_3	0.92 ± 0.02	2.4 ± 0.1
Sb_2O_{3D}	Sb_2O_3	Source unknown	Sb_2O_3 (wide)	100% Sb_2O_3	0.85 ± 0.10	2.1 ± 0.003
Pb_3O_4	Pb_3O_4	AEL Mining Services	Pb_3O_4	100% Pb_3O_4	3.2 ± 0.02	0.74 ± 0.08
Si	Si	Milrox	Si (Type 4)	100% Si	1.5 ± 0.02	11 ± 0.4

3.1.3 Scanning Electron Microscopy (SEM)

The morphology of the powders was studied with a Zeiss Ultra 55 FESEM field emission scanning electron microscope (FESEM) fitted with an InLens detector, at an acceleration voltage of either 1 kV or 2 kV. The SEM revealed the large agglomerates of smaller fused nano-particles in some of the components. This is especially important for the Mn samples. Since this agglomeration of nano-particles forms a large porous particle, it is expected that the combustion mechanisms would differ from that of a solid Mn particle of the same size. An example of the porous (fused nano-particles) and the solid Mn particles is shown in **Figure 3-5**.

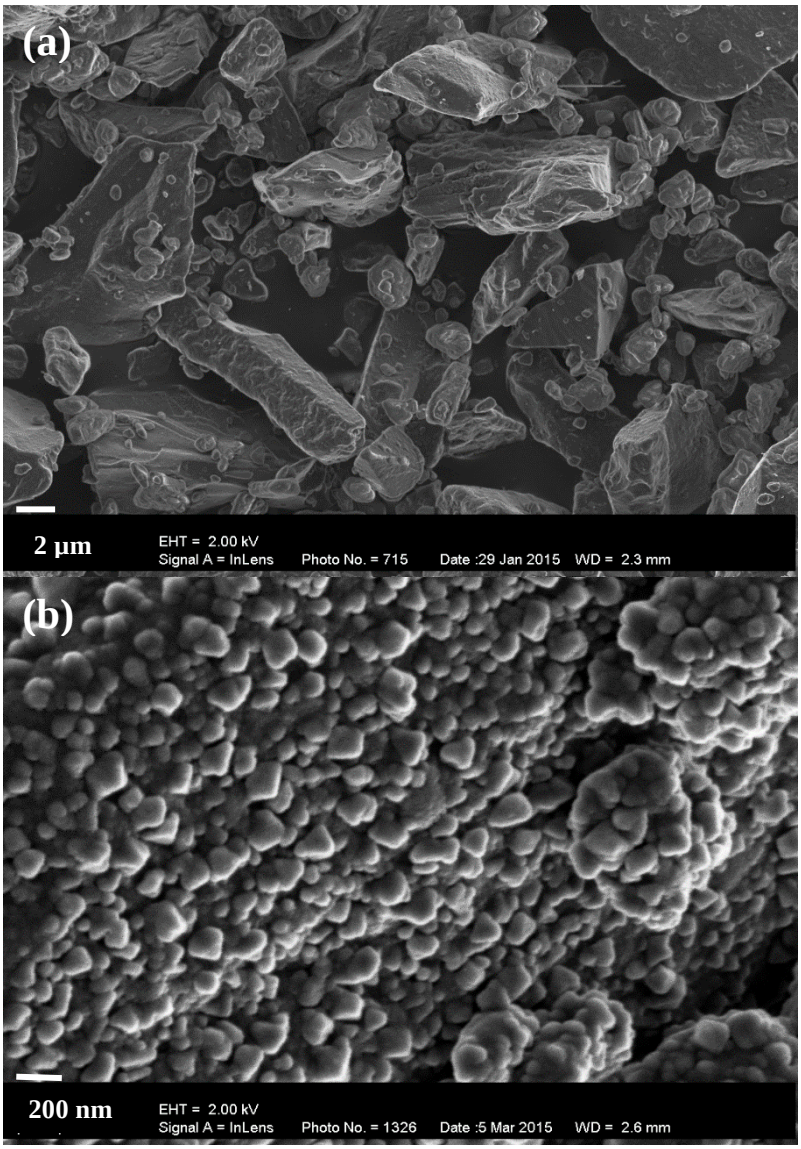

Figure 3-5: FESEM images of the (a) solid Mn_D and (b) the porous Mn_F samples

The oxide materials all show this agglomeration of smaller particles. **Figure 3-6** shows an example of a MnO_2 sample and a Sb_2O_3 sample.

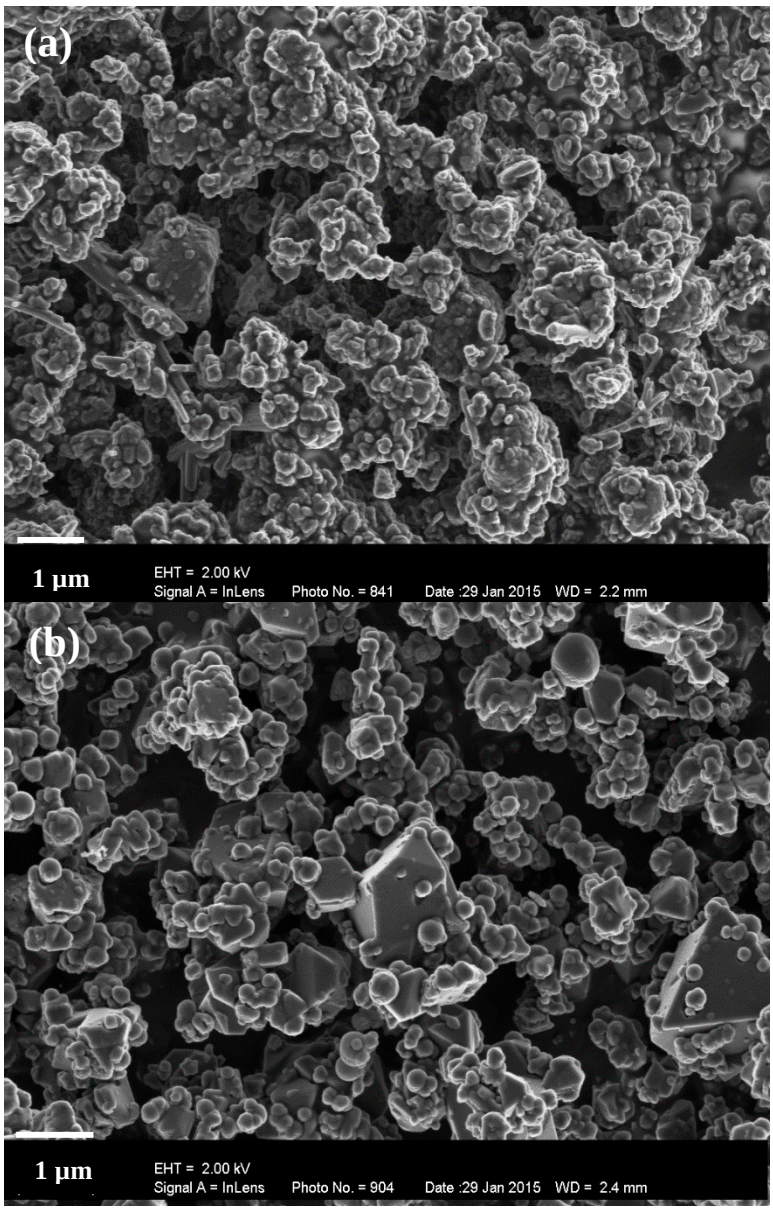

Figure 3-6: FESEM images of (a) MnO_{2C} and (b) Sb_2O_{3A} samples

The FESEM images of all the materials are given in Appendix B.

3.1.4 Thermogravimetric analysis (TGA)

Thermogravimetric analysis (TGA) was used to evaluate the extent of oxidation of the fuel and oxidant particles. TGA was performed on a Mettler Toledo A851 simultaneous TGA/SDTA instrument. About 20 mg of powder sample was placed in open 70 μL alumina pans. The temperature was scanned from 25 to 1 300°C at a rate of 20 °C min^{-1} with oxygen flowing at 50 mL min^{-1}. The analysis was performed on both of the fuels as well as the Sb_2O_3 and MnO_2 samples. The thermogravimetric behaviour of the Pb_3O_4 was not analysed.

A. Manganese

The profiles obtained from the TGA for each of the Mn samples are shown in **Figure 3-7.**

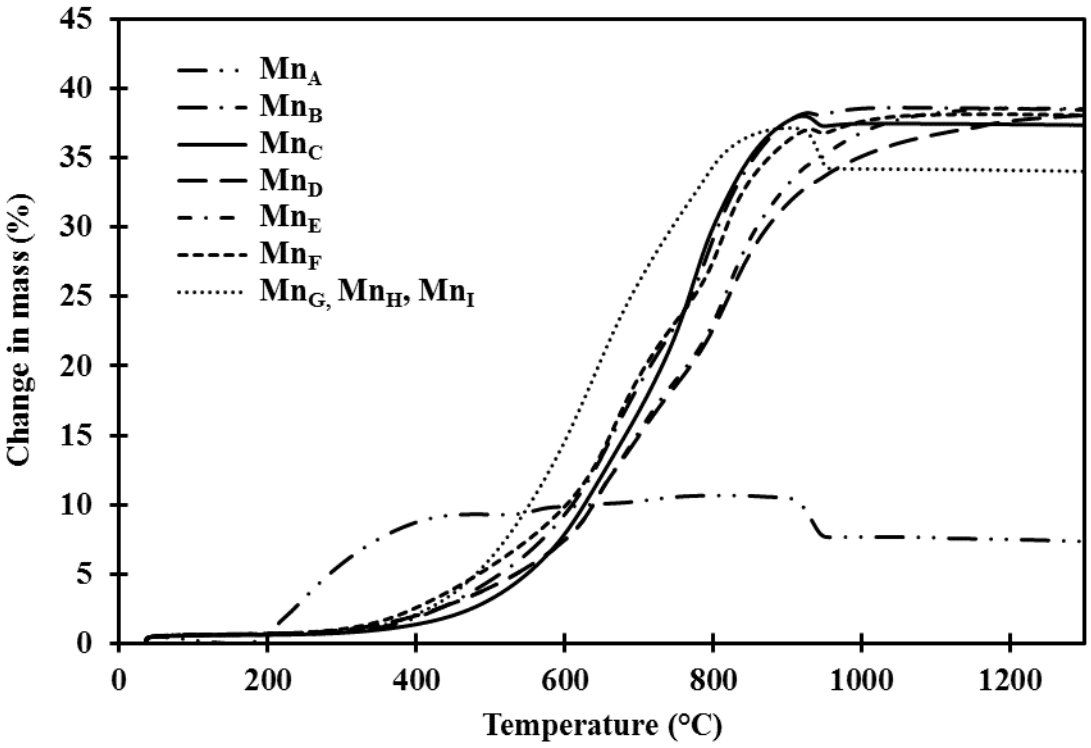

Figure 3-7: TGA results for each of the Mn samples

The most likely sequence of change that occurs during the oxidation of Mn can be described by **Scheme 3–1** below with the corresponding fractional changes in mass in brackets (Swanepoel et al., 2010).

$$\mathrm{Mn}\ (1.00) \rightarrow \mathrm{MnO}\ (1.29) \rightarrow \mathrm{Mn_2O_3}\ (1.44) \rightarrow \mathrm{Mn_3O_4}\ (1.39) \qquad \textbf{Scheme 3–1}$$

The first event described in **Scheme 3–1** is the oxidation of Mn to MnO, which occurs at around 560 °C and results in a 29% mass increase. The second event corresponds to the

oxidation of MnO to Mn_2O_3 at around 800 °C, with a further mass increase of 15%. The final event of Mn_2O_3 reducing to Mn_3O_4 occurs at around 950 °C and causes a mass decrease of 5%. This sequence results in a final mass increase of 39% when full oxidation of Mn to Mn_3O_4 occurs (Swanepoel et al., 2010). From **Figure 3-7** it can be seen that samples Mn_B - Mn_I all have no significant oxidation present. Sample Mn_A, however, had a very large amount of oxidation present before the test was conducted. This can be seen from the final weight increase of only 6.55% that indicates less oxidation has occurred than expected.

B. Manganese dioxide

The thermogravimetric profiles obtained for each of the MnO_2 samples are shown in **Figure 3-8**.

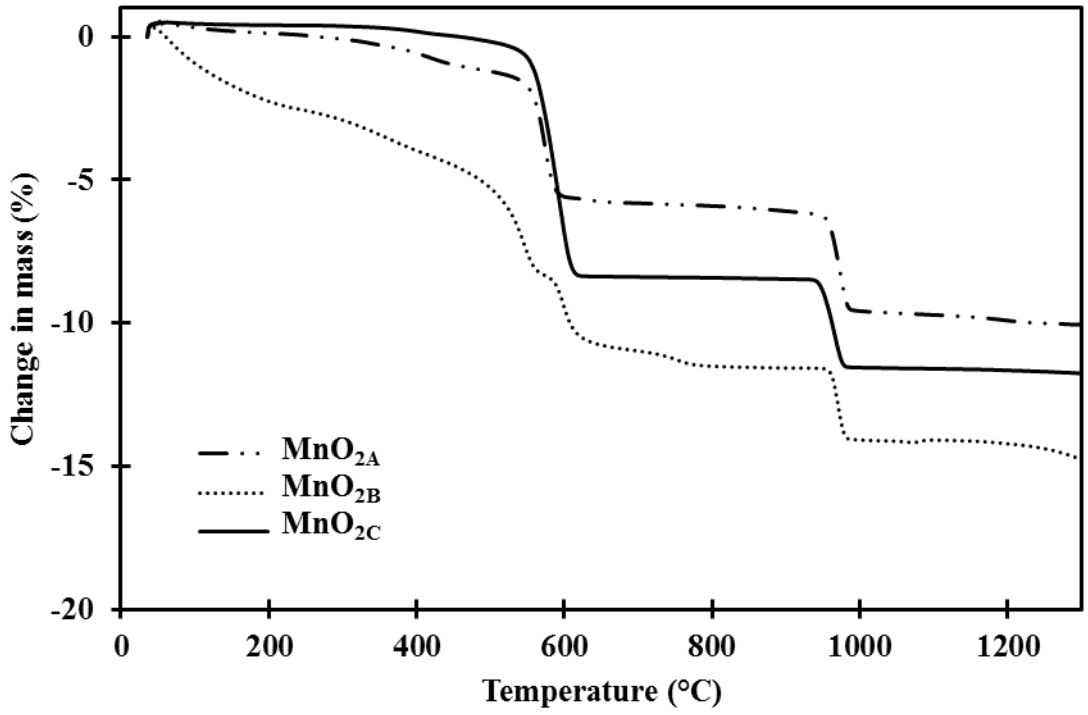

Figure 3-8: TGA results for each of the MnO_2 samples

The MnO_2 shows two distinct steps of reduction in mass which occurs at the reduction of MnO_2 to Mn_2O_3 and the reduction of Mn_2O_3 to Mn_3O_4. The reduction of Mn_3O_4 to MnO only starts to occur above 1 200 °C and therefore only the start of this step is visible in **Figure 3-8** (Swanepoel et al., 2010).

C. Antimony trioxide

The thermogravimetric profiles obtained for each of the Sb_2O_3 samples are shown in **Figure 3-9**. The Sb_2O_3 starts to slowly sublimate at around 450 °C along with oxidation to Sb_2O_4 at around 460 °C. The Sb_2O_4 is converted to Sb_4O_6 (g) above 1 050 °C, which leads to a mass decrease until all the material is in the gaseous phase (Golunski and Jackson, 1989).

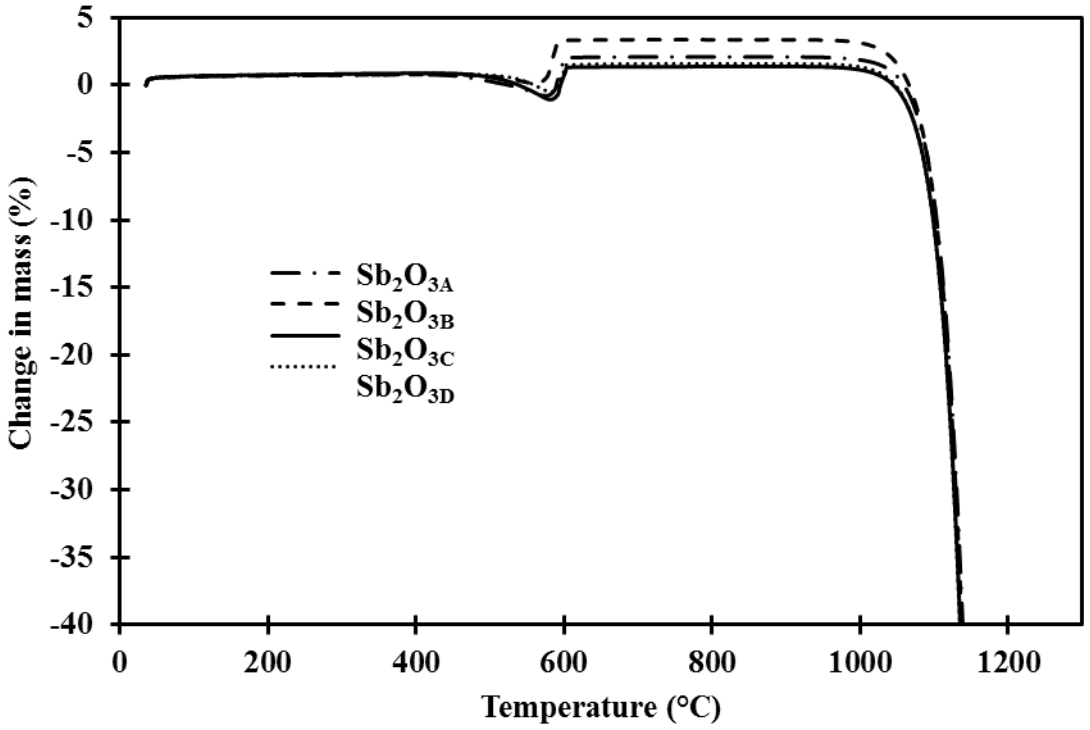

Figure 3-9: TGA results for each of the Sb_2O_3 samples

D. Silicon

The thermogravimetric profile obtained for the Si sample is shown in **Figure 3-10**. The TGA results indicated no significant mass changes between 25 and 600 °C, but the formation of silicon nitride is observed above 600 °C by some mass increase (Tichapondwa et al., 2010).

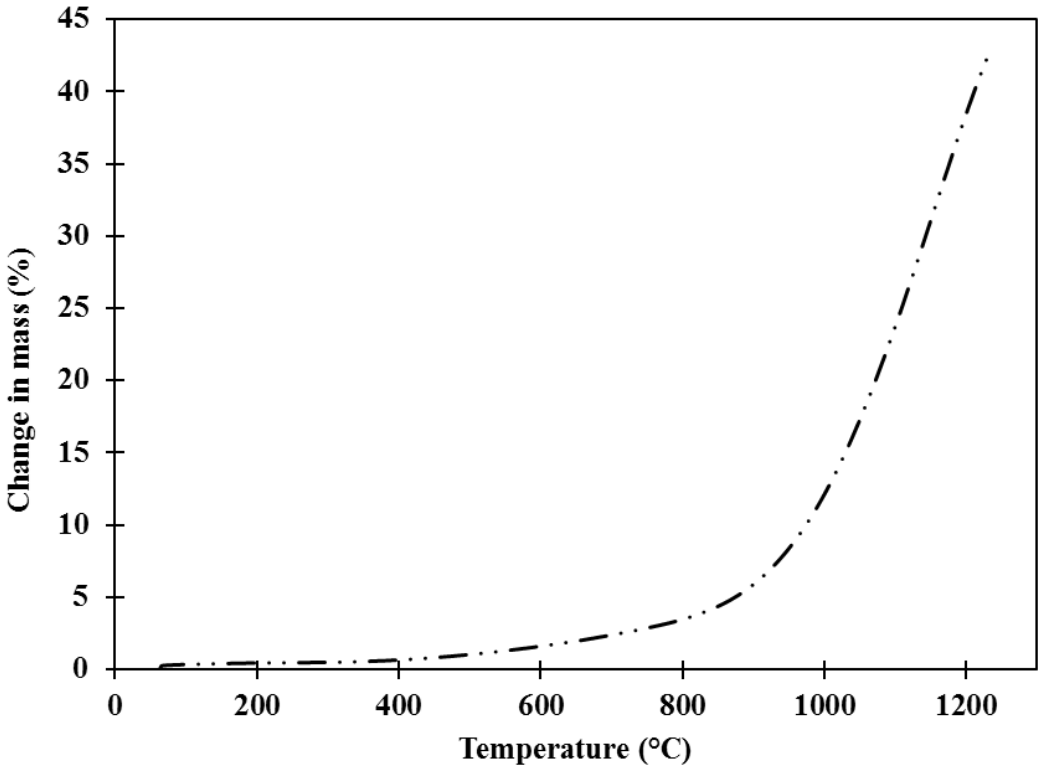

Figure 3-10: TGA results for the Si sample

3.2 DELAY ELEMENT PREPARATION

The delay compositions were prepared by brush-mixing 5 times through a 63 µm sieve. This technique helps to break down agglomerates and facilitate proper mixing. The study was conducted on both lead tube delay elements and aluminium tube delay elements. The filling, compacting and assembly of these two types of delay elements are described in detail in this section.

3.2.1 Lead delay elements

A fixed amount of mixed composition (4 g, 11 g and 11 g for Si/Pb_3O_4, Mn/Sb_2O_3 and Mn/MnO_2 mixtures respectively) was poured into a 166 mm long lead tube with initial inner and outer diameters of 7.0 mm and 11.5 mm respectively. The ends were crimp sealed to prevent any powders from escaping from the tubes during extrusion. The tubes were then subjected to a ten-step proprietary rolling machine in order to compress and consolidate the powders. The final outer diameter was 6.4 mm and the core diameter and overall length depended on the packing density of the filled composition.

The lead tube was then cut into 100 mm and 44 mm sections to form long and short-delay elements. The length of the delay elements was determined by the burn rate measurement technique.

The lead delay elements were assembled for testing by fixing an aluminium tube to one end of the lead tube and adding an aluminium cap, a rubber grommet, a rubber seal and a shock tube. The aluminium tube was then crimped onto the lead tube to ensure a secure fit. The other end of the tube was crimp sealed and a small hole drilled at the end to ensure that any gas produced could vent and did not build up in the element. The Mn/Sb_2O_3 and Mn/MnO_2 compositions required a starter composition. The starter composition was added by scraping out a small amount of composition from the element and replacing it with the starter composition. **Figure 3-11** shows the assembly of the entire lead-drawn delay element.

3.2.2 Aluminium delay elements

The aluminium delay elements were prepared by pressing the mixed delay composition into the aluminium tubes using a hydraulic press. Only the Si/Pb_3O_4 composition was tested using aluminium tube elements. The filling process was performed at 100 kg load, with ±0.2 g increments being filled and pressed until the tube was completely filled to the top (±11 increments). The aluminium tubes were manufactured to contain an extension that could accommodate all the ignition components. The ignition components used for the aluminium tubes were the same as for the lead tubes. The assembly of the aluminium delay elements is shown in **Figure 3-12**.

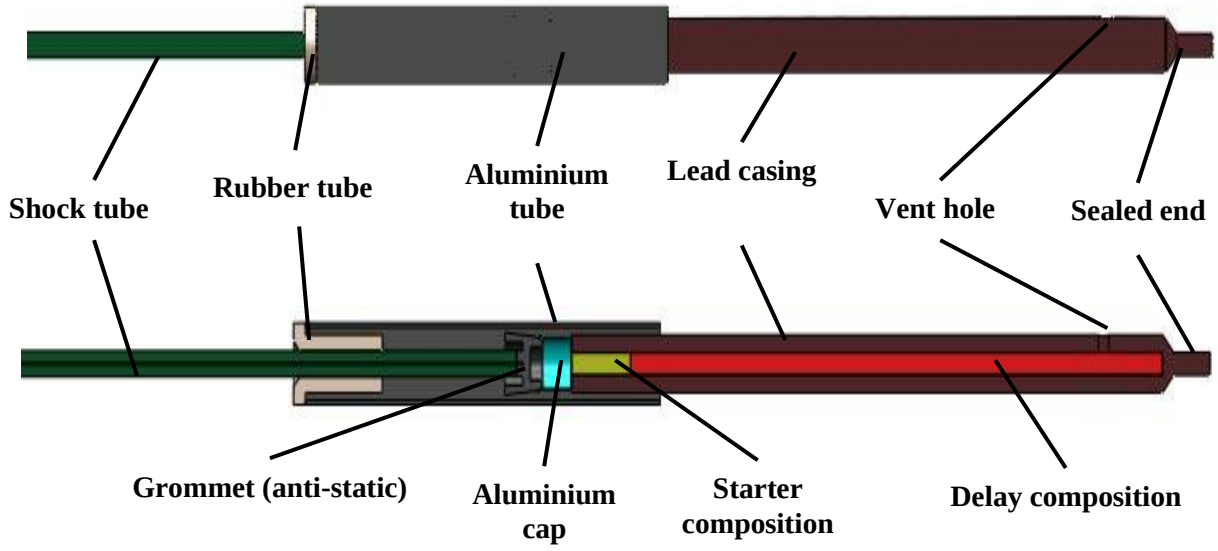

Figure 3-11: Assembly of the lead delay elements

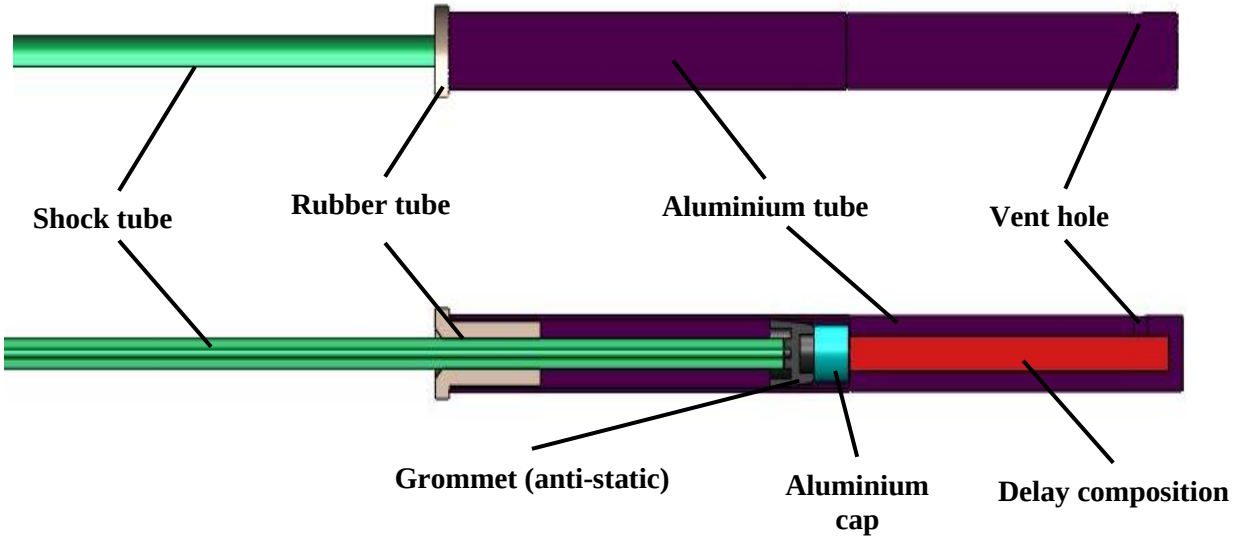

Figure 3-12: Assembly of the aluminium delay elements

3.3 BURN RATE MEASUREMENTS

The burn rates measured for pyrotechnic delay elements depend to some extent on the technique used for the measurement. One of the objectives of this study was to develop a safe, reliable and accurate method of testing the burn rates of the elements.

The commercial method of testing the burn rates of delay elements used in the mining industry consists of testing the time between ignition and detonation in a fully assembled detonator. The use of primary and secondary explosives in the detonators poses a high safety risk to the personnel performing the tests, especially in a laboratory-scale setup. The most commonly used laboratory-scale testing technique uses two thermocouples. These thermocouples are placed inside the delay element and the burn rates are calculated from the temperature profiles measured by the thermocouples. However, the burn rates measured using this technique differs significantly from those obtained using the commercial testing technique. The new IR camera technique that was developed here will therefore be evaluated against both of these techniques to determine the accuracy of the method. The setup and methodology of each technique is discussed in this section.

3.3.1 Commercial testing technique

One of the methods applied to measure the burn rates was to assemble the delay elements into commercial detonators. The detonators consisted of an aluminium shell containing a section of a primary explosive (lead azide) and a high explosive (pentaerythritol tetranitrate). These sections of explosives are followed by the lead-drawn delay element. The detonators were initiated via shock tubes and ignited by an electric firing device. An aluminium cap, rubber grommet and rubber tube were also inserted into the aluminium shell as shown in **Figure 3-11** and **Figure 3-12**. The burn rate was determined from the time interval recorded between the triggering of a photoelectric cell and receiving a terminating signal from a pressure transducer. Tichapondwa et al. (2010) provide a more detailed description of the test procedure.

3.3.2 Thermocouple technique

The delay elements were also tested using the common laboratory technique of utilising thermocouples as triggers. The delay elements were assembled as shown in **Figure 3-11**. Two 'Type S' thermocouples (one 2 mm (TC_1) and one 3 mm (TC_2)) were placed 70 mm apart in the lead elements. In order to ensure that the thermocouples could make proper contact, small holes were drilled into the element and the thermocouples were inserted into the holes. The burn rate was calculated from the time difference between a specific threshold temperature rise detected by the thermocouples. **Figure 3-13** shows the typical temperature profiles measured using the two thermocouples. The effect of the depth of the thermocouples and also the distance between the thermocouples were investigated.

Figure 3-13 shows the difference between the profiles measured with thermocouples placed deep in the core and with thermocouples placed at the interface between the lead tube wall and the composition core. **Figure 3-13** also compares these profiles to those obtained from the core of the tube with a shorter distance between the two thermocouples.

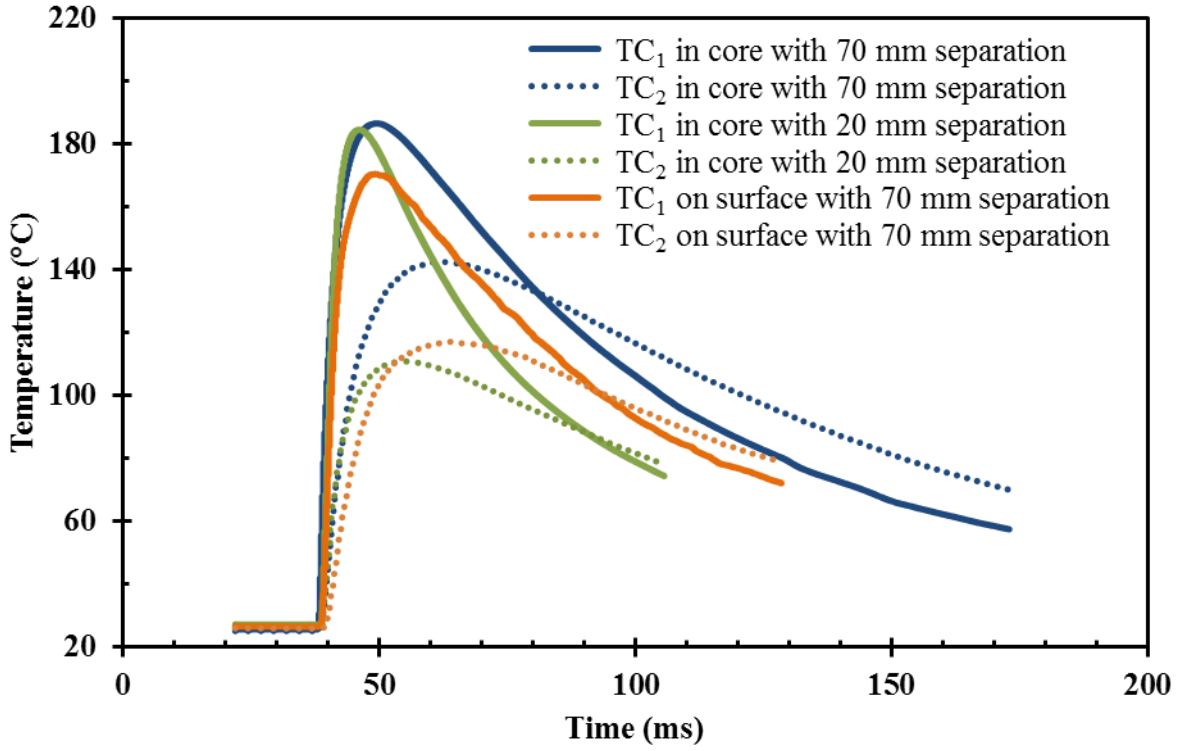

Figure 3-13: Temperature profiles measured using the thermocouple technique – the depth of the thermocouples (core vs. surface) and the distances (20 mm and 70 mm) between them are compared. TC_1 and TC_2 represent the thermocouples with diameters of 2 mm and 3 mm respectively.

In **Figure 3-13** it can be seen that the measurement is highly dependent on the placement of the thermocouples as well as on their size. The smaller size thermocouple (TC_1) has a much faster response than the thicker thermocouple (TC_2). This agrees with other studies, which indicate that the diameter of the thermocouple significantly influences the calculated burn rate (Jakubko, 1999, Boddington et al., 1982, Boddington et al., 1986). The profile is further highly dependent on the depth at which the thermocouple is placed. When the thermocouple is not placed exactly at the core of the element, the response is also delayed and the magnitudes measured are significantly reduced.

The final measurements were therefore made with the two thermocouples placed in the core of the element with a spacing of 70 mm between them. This provides enough space between the thermocouples while still eliminating the ends of the element.

The threshold temperature that acts as the start and end triggers on the two thermocouples is also an important factor. **Figure 3-13** shows that the profiles of the two thermocouples are not parallel due to the response time being dependant on the size of the thermocouples. The burn rate calculated is therefore expected to change depending on the threshold temperature that activates the trigger. **Figure 3-14** shows how the calculated burn rate varies as the threshold temperature used to trigger the timer is varied. This investigation was performed on fast-burning (36 wt.% Si + Pb_3O_4), medium-burning (50 wt.% Si + Pb_3O_4) and slow-burning (36 wt.% Mn + Sb_2O_3) compositions. Since these burn rates differ in orders of magnitude, in each case the burn rate was normalised to its respective peak burn rate to allow comparison. These measurements were furthermore performed over a period of two weeks and the ambient conditions varied significantly during this period. To eliminate this effect in the thermocouple measurements, the temperatures were also normalised to the ambient temperature.

Figure 3-13 shows that the temperature profiles become less parallel as the temperature increases. The response of TC_2 in comparison to TC_1 slows down faster as the temperature increases. This is also evident from **Figure 3-14**: the calculated burn rate decreases as the threshold temperature is increased. It was therefore decided that the lowest response temperature, corresponding to the maximum peak burn rate measured, would be used to calculate the burn rate as it is the least influenced by the thermocouple response time and external heat transfer.

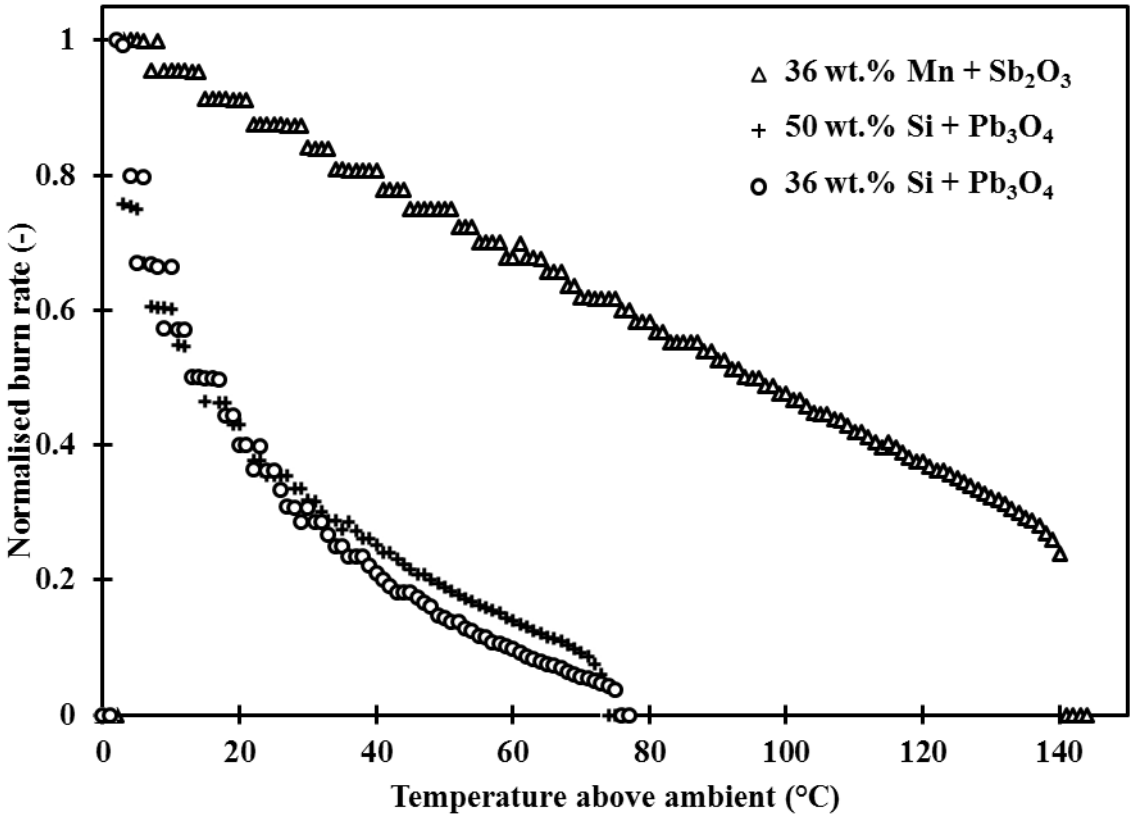

Figure 3-14: Effect of the threshold temperature on the burn rate calculated for fast-burning (36 wt.% Si + Pb_3O_4), medium-burning (50 wt.% Si + Pb_3O_4) and slow-burning (36 wt.% Mn + Sb_2O_3) compositions.

3.3.3 IR camera technique

The first objective of the study was to develop a new test method for measuring the burn rates of pyrotechnic time delay elements. The following requirements of the new testing technique were determined:

i. The method should be safer than the commercial test method and therefore must not require the use of primary or secondary explosives.
ii. The burn rates measured using the new technique should be comparable to the burn rates measured using the commercial technique.
iii. The method should deliver continuous results throughout the duration of the reaction.
iv. The elements tested using the new method should require minimal physical alterations for testing.

Due to the highly exothermic nature of pyrotechnics, the use of IR sensors was thought to be ideal for application in this field.

The application of IR cameras in high-temperature processes has increased significantly over the last two decades (Carlomagno and Cardone, 2010, Nagarajan et al., 1989). From the requirements set out above, it was decided that an IR camera would be a suitable method of measuring the burn rates of pyrotechnic delay elements. Since pyrotechnic reactions are highly exothermic in nature, the reaction should produce a large amount of radiative IR energy that can be measured using IR sensors. Since an IR camera consists of a large array of IR sensors rather than a single cell, it would be the best option for obtaining continuous information as required. The IR camera used in this study was the Dias Pyroview 380L compact. Its technical specifications are listed in **Table 3-2**. The other pieces of equipment required to apply this measurement technique were:

- ✓ A personal computer or laptop
- ✓ A local area network (LAN) cable
- ✓ Two small pieces of metal wire to connect the shock tube to the positive and negative wires of the ignition charge.
- ✓ A thermometer to measure the ambient temperature as input data to the IR camera.
- ✓ A long ruler, triangle or set square that could be used to ensure that the sample was parallel and straight in relation to the lens of the camera.

Since the surface of the lead is shiny and irregular after extrusion, it produces a lot of spectral scattering in the IR measurements. The delay elements were therefore all sprayed with a matt black high-temperature paint. This reduces the spectral scattering in the data and also changes the emissivity of the surface to a value close to 1 (black body radiation), which is optimum for IR measurements. The test setup, sequence and data analysis are discussed in the following sections.

Table 3-2: Manufacturer's specifications of the IR camera used in all burn rate measurements in this study (DIAS Infrared Systems, 2010).

Manufacturer's Specifications	**Dias Pyroview 380L compact**
Frame rate	50 Hz (max)
Uncooled IR array	384 x 288 pixels
Field of view	30° x 23° approx.
Measurement ranges	(-20 °C to 120 °C) or (0 °C to 500 °C)
Measurement uncertainty	2 °C or 2% of measured value
Operating temperature range	-10 °C to 50 °C
Temperature resolution	<80 mK @ (30 °C; 50 Hz)
Spectral range	8 μm to 14 μm
Operating voltage	10 VDC to 36 VDC

A. Testing setup and sequence

To ensure safety during testing, all the testing was performed inside a fume cupboard. A 7.5 mm polycarbonate sheet was placed inside the front cover of the fume cupboard for additional protection. The camera was placed inside the fume cupboard with the sample and connected to a laptop computer situated outside the cupboard via a Local Area Network (LAN) cable. The shock tube used to initiate the delay element was connected to the initiating charge, which was also situated outside the fume cupboard.

The input data to the IR camera had to be gathered before initiating the test. The first data required was the ambient temperature around the sample. The ambient temperature is used as a reference point for all calculations of IR energy to temperature. The other input data was the exact distance between the delay element and the lens of the IR camera. This was required to determine the size that each pixel would occupy in the test space. The sample was placed horizontally in front of the camera, with the vent hole facing upwards and away from the lens of the camera. This was to ensure that if some of the reacting material sprayed from the vent hole it would not spray onto the lens of the camera. The sample had to be parallel to the lens to ensure that no accuracy was lost due to miscalculations in the pixel dimensions.

Once the sample was secured in place, the polycarbonate sheet was placed over the opening of the fume cupboard. All input data to the camera were provided, including:

- ✓ Ambient temperature
- ✓ Data acquisition frame rate
- ✓ Sample emissivity
- ✓ Sample absorptivity

Once everything was in place and all safety measures had been taken, the shock tube of the sample was connected to the ignition charge. There was about a 2 s delay between initiating data acquisition and actually capturing the data. The camera therefore had to be activated at least 3 s before initiating the shock tube. Once it was clear that the material reaction was finished and that the element had started to cool, the data acquisition was stopped. The sample was then left in position until it had completely cooled down and could be safely removed.

B. Data analysis

The IR camera measures emittance and converts the measured values to display a set of temperature values. The software of the IR camera that was used for data analysis was 'Pyrosoft Professional'. The data is displayed as a temperature value for every pixel of every frame at which data were captured. The IR camera has a fixed number of uncooled IR sensors resulting in an array of 384 pixels horizontally and 288 pixels vertically. The pixels were assumed to be rectangular. The array can therefore be seen as taking 110 592 small rectangular isothermal control volumes within the image. Each pixel represents a single measurement and therefore the area contained in one pixel is specified at a single temperature value. The pixel is taken as a pseudo steady-state control volume from the time that the frame is captured until the next frame is captured. **Figure 3-15** shows an example of how the temperature array is displayed on a colour scale.

One very important factor that must be taken into account when using the IR camera is that the measured data are sampled data. One very important theorem when dealing with sampled data states that in order to obtain dynamic information about a system the frequency at which the data are sampled should be at least twice that of the maximum frequency of the system (Luyben, 1989). This theorem is mathematically represented in Equation 3–1.

$$\omega_{sampling} \geq 2\,\omega_{max} \qquad 3\text{-}1$$

This, however, was not always possible, since the burn rate of the fast-burning delay elements is very fast. The data acquisition frequency would therefore be a limiting factor in determining up to which burn rate this IR camera would be adequate.

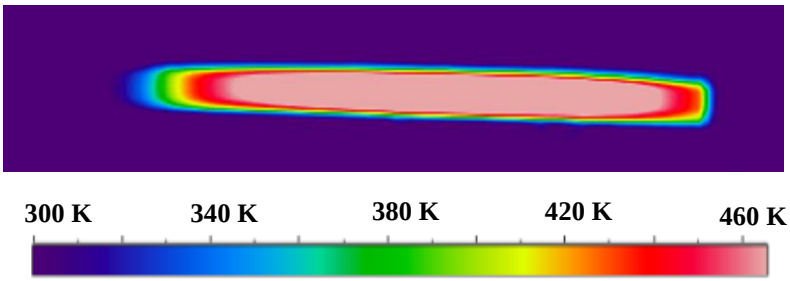

Figure 3-15: Example of a captured IR image of the delay composition –the temperature data from the camera is displayed on the colour scale alongside the image

The IR camera is equipped with its own spectral filters which ensure that most of the electromagnetic radiation from the visible spectrum as well as the ultra-violet spectrum has already been filtered out to minimise high-frequency noise. The sampled data did, however, still have some scattering present. The acquired data were therefore further filtered to ensure that occasional stand-out values did not interfere with further analysis. Such stand-out values could be caused by a wide variety of factors, to name only a few:

- Artificial light reflecting from the surrounding area
- Interference from large dust particles in the surrounding air
- Inconsistencies in the surface roughness and finish of the elements.

The data was filtered by using a 3rd-order moving average filter which was sufficient to remove occasional stand-out values. The output values after applying the filter were calculated from Equation 3–2.

$$T(\mathrm{i}) = \frac{1}{z}\sum_{j=0}^{z-1} T(i+j) \qquad 3\text{-}2$$

The MATLAB program written for the filtering of the data is given in Appendix C (named *IRdatafilter.m*).

The average burn rate was calculated by determining the axial distance that the reaction travelled in a certain amount of time. The average burn rates of all the samples were analysed from the centre of the sample.

When considering a single line in the centre of the sample at any given time, a temperature profile along the length of the sample at a single instant can be compiled. **Figure 3-16** shows two temperature profiles developed along the length of a sample at two instances in time (t_1 and t_2) along with their corresponding IR images. A temperature profile similar to the ones shown in **Figure 3-16** can be compiled for every consecutive frame that the IR camera captures. It is important to keep in mind that the IR images with the temperature data acquired are from the outer surface of the tube. This means that the heat generated by the exothermic reaction must first be transferred through the wall of the tube before the IR camera can measure it. When considering the different profiles in **Figure 3-16**, it can be observed that these profiles are almost parallel at very low temperatures. At higher temperatures, the shape of the different temperature profiles starts to deviate between frames (time). This is likely due to the fact that the higher temperatures are measured behind the actual combustion wave. They are therefore affected by the cooling of the reacted material earlier in the tube, along with heating from the reacting material further down the tube through conduction and convection mechanisms.

By calculating the distance that the wave has travelled over time at a specific threshold temperature, the average burn rate can be calculated. The distance the wave travelled can be directly related to the number of pixels passed in a certain time. The size of the pixels is a function of the distance that the sample is placed from the lens of the camera. The relationship between the size of the pixel and the distance between the sample and the camera in these experiments is described by Equation 3–3 (DIAS Infrared Systems, 2010).

$$Pixel_{hd} = \frac{2D_{IR}\, tan(FOV/2)}{Pixel_{hn}} \qquad 3\text{-}3$$

Once the horizontal length of the pixels has been determined, the distance that the temperature wave has travelled can be calculated by multiplying the size of the pixel by the number of pixels passed. The time that the wave took to cover this distance can be determined from the number of frames that the camera captured over this distance and the frame rate of the acquisition. The MATLAB program written for the calculations of the average burn rate is attached in Appendix C (named *averageburnrate.m*).

In order to accurately and consistently calculate the burn rate for different elements, the factors affecting this calculation had to be evaluated and defined. The first factor is the effect of the threshold temperature on the profile that is used to calculate the burn rate.

Since the effect is expected to be similar to the evaluation performed on the threshold trigger temperature in the thermocouple technique (**Figure 3-14**), the same approach was followed. The burn rates calculated at different threshold temperatures are shown in **Figure 3-17** for a slow-burning composition (36 wt.% Mn + Sb_2O_3), a medium-burning composition (50 wt.% Si + Pb_3O_4) and a fast-burning composition (36 wt.% Si + Pb_3O_4).

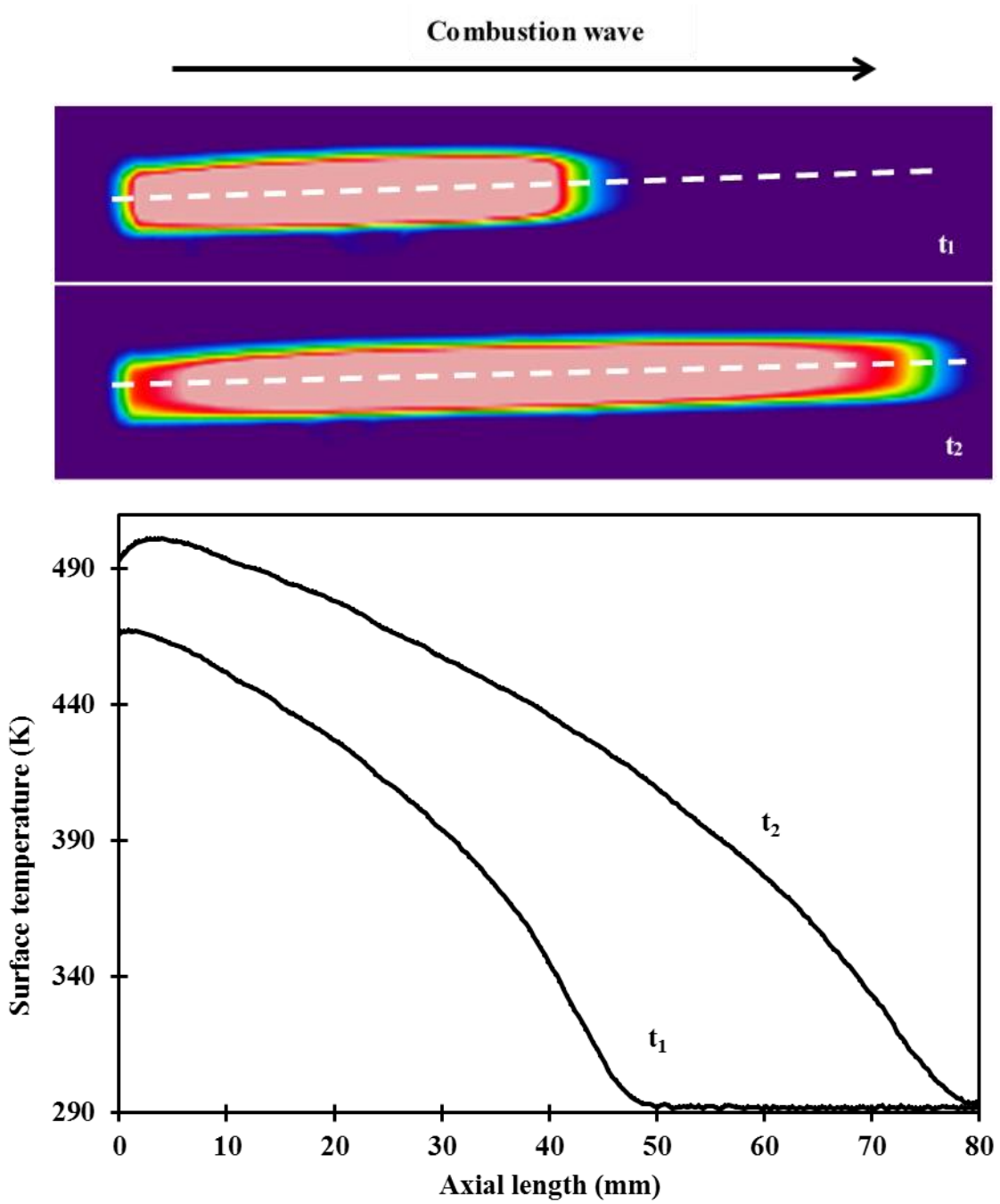

Figure 3-16: Example of two temperature profiles developed over the length of the element at two instances in time (t_1 and t_2) as derived from the IR camera data

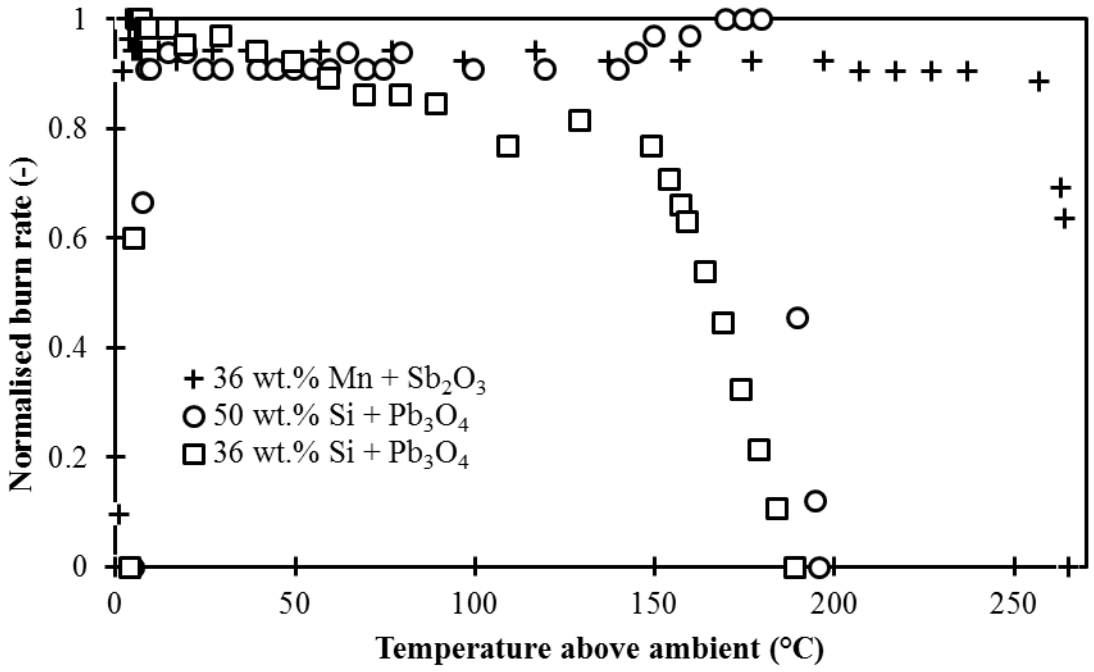

Figure 3-17: Calculated normalised burn rates using different threshold temperatures to determine the burn rate from the temperature profiles

From **Figure 3-17** it can be seen that the IR camera measurements are significantly less dependent on the threshold temperature used for calculating the average burn rate than the thermocouple technique. The slow-burning composition is almost independent of the calculation temperature and even the fast-burning delay composition has less of a gradient in change of threshold temperature than with the thermocouple technique. Another significant observation is that the peak temperature measured using the IR camera is about 110 °C higher than the peak temperatures measured using the thermocouples. Since melting of the inner layer of the lead was physically observed, it is expected that the surface temperature is in the range measured using the IR camera and not the thermocouples. The thermocouples likely measure lower temperatures due to a much slower response time than the reaction time. The contact between the thermocouples and the delay element is also likely not sufficient to properly conduct the heat. The most consistent results were obtained when the lowest possible temperature was chosen. The temperature should, however, still be high enough to ensure that fluctuations in ambient temperature measurements do not interfere with the calculations. The lowest temperature that was found viable was 5 °C above the ambient temperature.

The fluctuation in ambient temperature was always found to be less than 4 °C and therefore 5 °C above ambient was safe enough to avoid the influence of fluctuations and yet still low enough that the minimal amount of the heat transfer effects would be taken into account. To ensure that the calculations were accurate, five different threshold temperatures were used to calculate the burn rate, and the average burn rate of the calculations was used. The first threshold temperature was taken as 5 °C above the ambient temperature, and the other threshold temperatures were taken at 3 °C intervals above the first temperature.

The first and last sections of each element were also expected to have some effect on the burn rate. To eliminate these effects from the results, only the middle section of the samples was used in the calculation of the average burn rate. The length of the sample that was omitted at both ends had to be the same for all samples to ensure consistency in the calculations. In order to determine the length of element that should be eliminated, the instantaneous velocity profile over the length of the elements was calculated. **Figure 3-18** shows the instantaneous velocity profile over the full length of the element. The MATLAB program written for the evaluation of the instantaneous velocity profile is given in Appendix C (named *instantaneousvelocityprofile.m*).

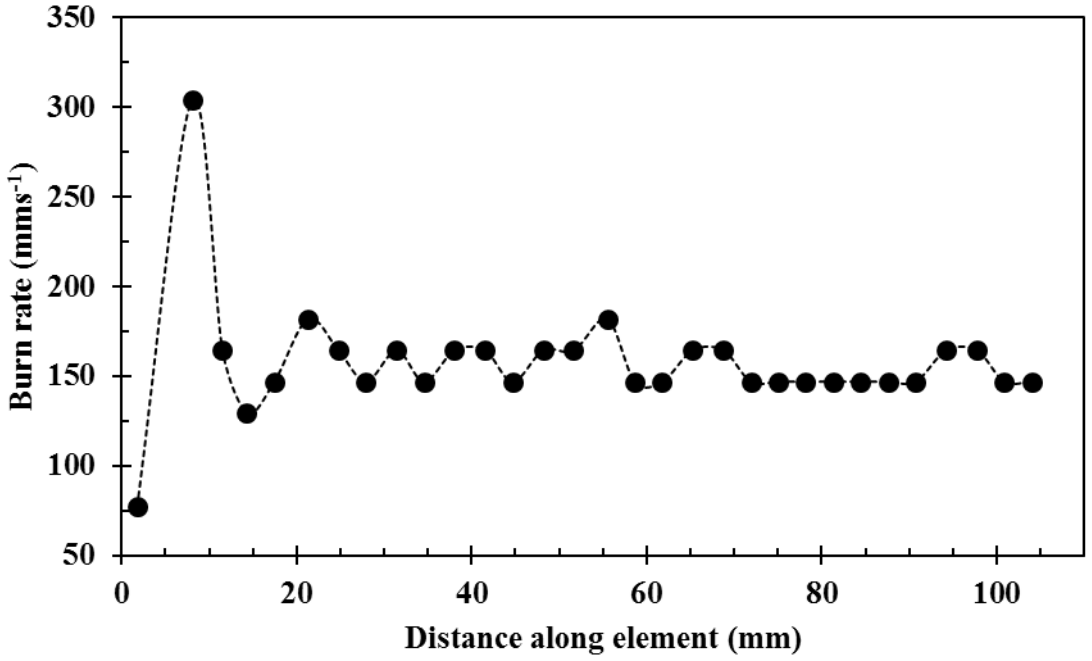

Figure 3-18: Instantaneous velocity profile along the axial length of the delay element for a lead tube delay element containing 36 wt.% Si + Pb_3O_4

From **Figure 3-18** it was found that the first 15 mm of the element had a different burn rate than the rest of the element. This is likely due to the ignition system at the beginning of the element having different heat transfer rates, and the heat is thus transferred to the outside surface at a different rate than the rest of the element. The ignition mechanism can also influence the first section of the element, and therefore it was decided to exclude these sections when calculating an average burn rate.

4 NUMERICAL MODELING OF DELAY ELEMENTS

A finite element model of the pyrotechnic reaction inside the delay elements was created using COMSOL Multiphysics (COMSOL, 2013). The model incorporates both the pyrotechnic mixture inside the element as well as the physical structure of the element. The geometry, meshing, governing equations and numerical solver are discussed in this section.

4.1 GOVERNING EQUATIONS

The mathematical equations used to simulate the reactions are divided into two groups: the first group contains all the equations describing how the chemical reaction occurs and is contained within the first governing equation, which is the conservation of mass. The second group of equations are concerned with the heat transfer present in the model and falls under the second governing equation describing the complete energy balance. Two reactions (one fast and one slow) were chosen to evaluate the model. The first was the reaction of Mn (Mn_H) with Sb_2O_3 (Sb_2O_{3D}) and the second was Si with Pb_3O_4. In both cases a fuel content of 36 wt.% was used.

4.1.1 Conservation of mass

This section contains all the equations used to describe the chemical (pyrotechnic) reaction, including all aspects of the mass balance. In order to predict the reaction kinetics, the first thing that was required was the chemical reaction equation, which describes how the combustion reactions take place. In order to predict the chemical reaction equations, Ekvi (Noläng, 2004) simulations were done to determine the most thermodynamically stable reaction equations favoured. The results of these simulations for both the compositions are shown in **Figure 4-1**. From these simulations, the reaction equations describing the reactions of the two compositions were predicted as presented in **Scheme 4–1** and **Scheme 4–2** for the Mn + Sb_2O_3 and Si + Pb_3O_4 reactions respectively.

$$2Si + Pb_3O_4 \rightarrow 3Pb + 2SiO_2$$ **Scheme 4-1**

$$4Mn + Sb_2O_3 \rightarrow MnSb + Sb + 3MnO$$ **Scheme 4-2**

Scheme 4–1 indicates that the Si + Pb_3O_4 reaction proceeds via the expected thermite (redox) reaction (Jakubko and Cernoskova, 1997, Al-Kazraji and Rees, 1978, Al-Kazraji and Rees, 1979). The reaction for Mn with Sb_2O_3 in **Scheme 4–2**, on the other hand, appears to undergo a thermite reaction along with an exothermic intermetallic reaction, producing alloys of Mn

and Sb. This was, however, an exceptional finding and needed to be further compared with experimental data in order to confirm the existence of this exothermic intermetallic reaction.

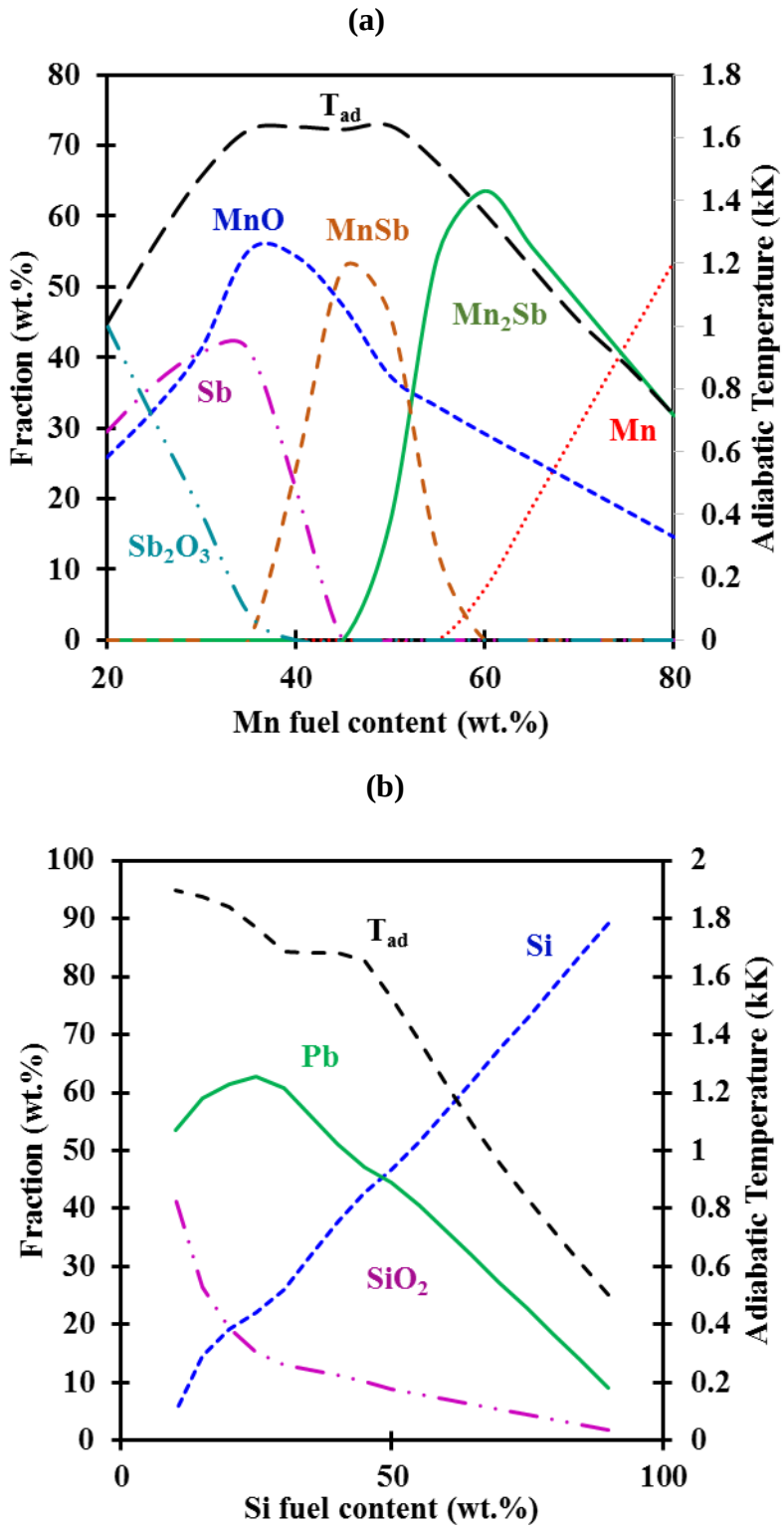

Figure 4-1: The Ekvi simulation predictions of the different reaction products obtained and the adiabatic combustion temperature for (a) the reaction of Mn + Sb_2O_3 and (b) Si + Pb_3O_4

In order to validate the predictions of the Ekvi simulations, XRD analysis was performed on the reaction product residues of the Mn + Sb_2O_3 reaction, containing various fuel contents. The XRD diffractograms of the residues produced after burning for the samples that contained 25 wt.%, 35 wt.% and 45 wt.% Mn prior to combustion are shown in **Figure 4-2**. The XRD diffractograms of all the samples are shown in Appendix D.

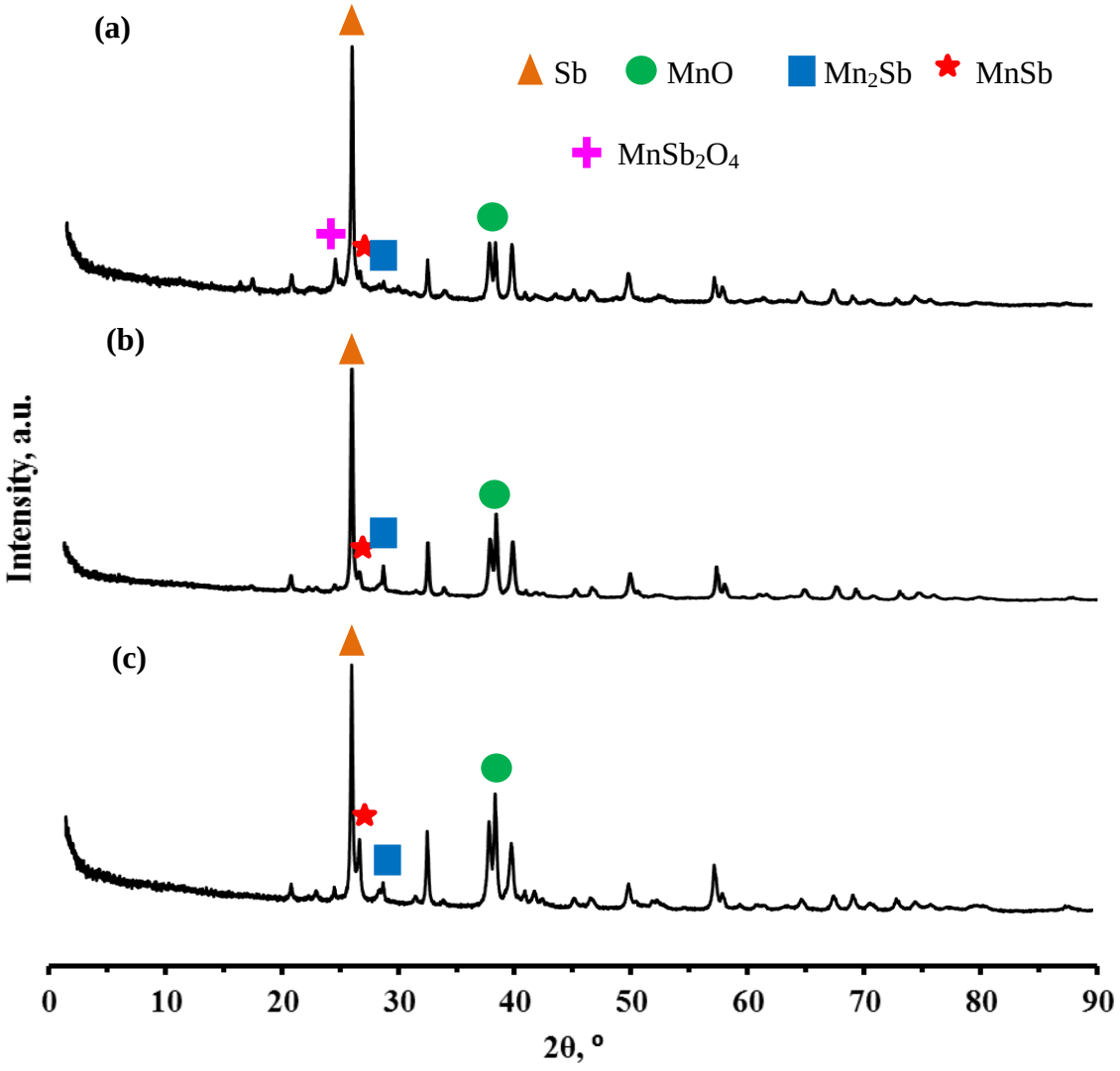

Figure 4-2: XRD diffractograms of the residues obtained after combustion for samples that contained (a) 25 wt.%, (b) 35 wt.% and (c) 45 wt.% Mn with Sb_2O_3

The Ekvi simulations shown in **Figure 4-1** indicate the presence of unreacted Sb_2O_3 for samples that are fuel lean (<36 wt.% Mn). This is expected for the first redox reaction depicted in **Scheme 4-3**.

$$3Mn + Sb_2O_3 \rightarrow 2Sb + 3MnO$$ **Scheme 4-3**

The XRD analysis, on the other hand, indicates the presence of $MnSb_2O_4$ with a peak at $2\theta \approx 27.3°$. This peak was found for samples that contained 35 wt.% or less fuel.

A local peak in adiabatic flame temperature (>1630 K) was found at this composition of the Ekvi simulations in **Figure 4-1**. Above this composition the formation of MnSb and Mn_2Sb was predicted by the Ekvi simulations, which were confirmed through the XRD results shown in **Figure 4-2**. The XRD analysis indicated that all the samples contained, to some extent, the MnSb intermetallic product. Even the samples that only contained 25 wt.% Mn as fuel also showed a small presence of MnSb. The presence of the Mn_2Sb is visible through a peak at $2\theta \approx 31.3°$, which was also always accompanied by a second structure of Mn_2Sb with a main peak at $2\theta \approx 36.3°$. The overall peak in adiabatic flame temperature occurred at about 49 wt.% Mn. This composition is consistent with the stoichiometric value of the standard thermite reaction, combined with an additional exothermic reaction represented in **Scheme 4-4.**

$$5Mn + Sb_2O_3 \rightarrow 2MnSb + 3MnO \qquad \textbf{Scheme 4-4}$$

At even higher fuel contents the presence of unreacted Mn could also be observed with a peak at $2\theta \approx 43°$. Another significant observation from the Ekvi simulations of the Mn + Sb_2O_3 system, was that the adiabatic flame temperature reached close to a plateau value between the fuel contents of 35 wt.% and 55 wt.%. This is a highly favourable characteristic as it indicates that steady self-propagation of the reaction can be expected over a wide range of fuel contents. This plateau can be attributed to the formation of the Mn with Sb alloys through exothermic reactions. The XRD diffractogram of the sample containing 25 wt.% also show the formation of $MnSb_2O_4$ which is not predicted with the EKVI thermodynamic simulations. This component is likely formed during the cooling period between unreacted reagents. It is only present in the most oxidant-rich composition. The XRD diffractograms of all the samples containing from 25 wt.% Mn to 50 wt.% Mn are shown in Appendix D.

In the numerical model developed, the reaction of the composition is modelled as a stationary batch reactor with its corresponding mass balance described in Equation 4-1.

$$\frac{dC}{dt} = r_i \qquad 4\text{-}1$$

The reaction rate is described through an autocatalytic reaction rate between the oxide reagent (B) and the main thermite (redox) reaction product (D) as indicated in Equation 4-2.

$$r_i = k C_B^n C_D^m \quad 4\text{-}2$$

The initial concentrations of all the components are given in **Table 4-1**. The initial concentrations of component D in both cases are actually zero, but for initiation of the numerical solver this has to be a non-zero value. The initial concentration of component D in both cases was therefore set at 1% of the limiting reagent concentration.

Table 4-1: Initial concentrations of all reagents used in the two models

Component	**Initial Concentration (**mol/m^3**)**
C_{Si_i}	31 049.00
C_{Pb3O4_i}	2 213.00
C_{Pb_i}	0.00
C_{SiO2_i}	22.13
C_{Mn_i}	26 251.00
C_{Sb2O3_i}	8 795.00
C_{MnSb_i}	0.00
C_{Sb_i}	262.50
C_{MnO_i}	0.00

The temperature dependence of the reaction rate is described by the Arrhenius equation given in Equation 4-3.

$$k = k_0 exp\,(-E_a/RT) \quad 4\text{-}3$$

The heat generated by the reaction over the time progression of the reaction is described by Equation 4-4, where the heat of reaction was experimentally measured using a bomb calorimeter.

$$Q = r_i H_{rx} \quad 4\text{-}4$$

The heats of reaction for the two reactions measured were 1.211 (±0.023) MJ/kg for the Si + Pb_3O_4 reaction and 1.163 (±0.014) MJ/kg for the Mn + Sb_2O_3 reaction. These values, however, differed by more than 20% from the expected theoretical values. This created some doubt as to the reliability of the bomb calorimetry measurements for this application. For this

reason the theoretical heats of reaction used in the model were 1 098.15 kJ/mol oxidant and 513.35 kJ/mol oxidant for the Si + Pb_3O_4 and Mn + Sb_2O_3 reactions respectively.

4.1.2 Heat transfer

There are several heat transfer mechanisms present in the numerical model that contribute to the energy balance over the delay element. The different heat transfer mechanisms that are present in the energy balance are described in **Figure 4-3.**

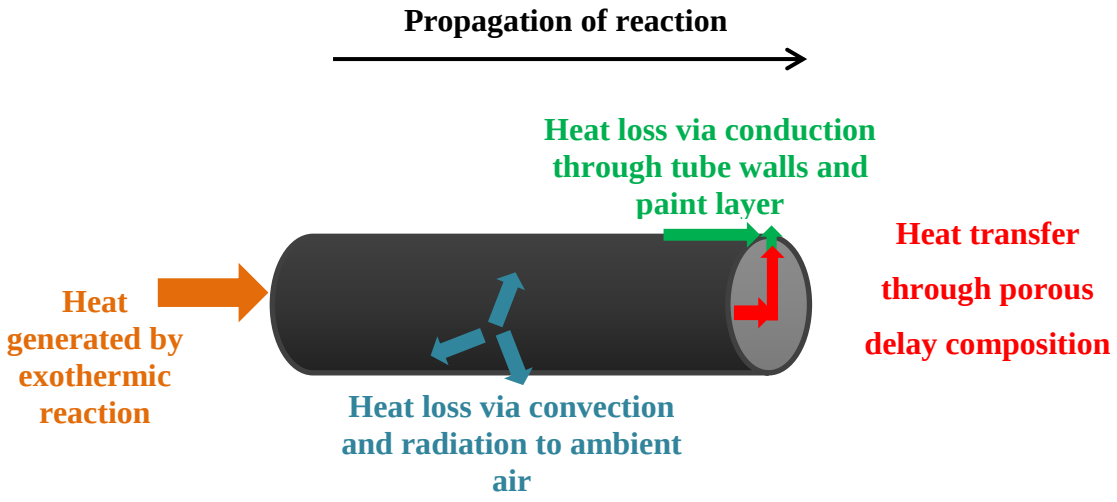

Figure 4-3: The heat transfer mechanisms present in the energy balance over the delay element

The first mechanism is the heat generated by the combustion reaction. This heat is the driving force for the reaction to propagate along the length of the tube. The heat generated is transferred radially and longitudinally through the delay composition to allow the reaction of the composition to propagate. The heat is further transferred through the solid lead tube and the solid paint layer through the conduction mechanism. The heat is lost from the paint layer to the surrounding air via convection and radiation.

The heat generated through the reaction is the heat source necessary for the reaction to progress. The heat is transferred through the powder mixtures longitudinally via conduction. This conduction mechanism, however, has to take into account that the powder mixture is not a solid material, but consists of a mixture of metal and metal oxide powders with air spaces in between. The model should therefore describe the conduction of heat through a porous medium. The energy balance over this porous mixture of the filled powder is described as follows:

$$(\rho C_p)_{eq} \frac{\partial T}{\partial t} = \nabla \cdot (\lambda_{eq} \nabla T) + Q \quad 4\text{-}5$$

This conduction model incorporates the porosity of the material through equivalent thermal properties $(\rho C_p)_{eq}$ and λ_{eq}. The equivalent thermal conductivity and equivalent heat capacity are calculated using a parallel mixing model where heat transfer is assumed to occur parallel to the direction in which the mixture and the air are packed alternatingly (Mujumdar, 2006). The parallel model for calculating the equivalent thermal conductivity and equivalent volumetric heat capacity of the packed delay composition is given in Equations 4–6 and 4–7 respectively.

$$\lambda_{eq} = \theta_s \lambda_s + (1 - \theta_s) \lambda_f \quad 4\text{-}6$$

$$(\rho C_p)_{eq} = \theta_s \rho_s C_{p,s} + (1 - \theta_s) \rho_f C_{p,f} \quad 4\text{-}7$$

The subscript *s* indicates the properties of the solid powder mixture, and *f* indicates the fluid properties, which in this case is air. In order to calculate the equivalent thermal conductivity, the individual properties first had to be determined. Pyrotechnic reactions occur at very high temperatures and physical phenomena such as phase changes occur during the process. It was therefore decided that the model should contain temperature-dependent properties as far as possible. There are currently no reliable thermal conductivity data available in the literature for Pb_3O_4 and no models for predicting thermal conductivity (Mujumdar, 2006). Pb_3O_4, however, decomposes to PbO + O_2 above 813 K, which is far below the expected reaction temperature (Jakubko and Cernoskova, 1997, Al-Kazraji and Rees, 1978, Sulacsik, 1974). The thermal conductivity of PbO is available in the literature and was therefore used instead. The error resulting from this assumption is expected to be significant only below 813 K and not in the expected temperature range (+1 000 K) for the reaction. Also notable is that very little data have been published on the properties of the materials above melting point. The properties were in these cases assumed to remain constant over all temperatures in the liquid phase. Since the changes in properties over phase changes are orders bigger than the variation over temperature in a single phase, this is not expected to influence the model significantly. The thermal conductivity of the solid mixture of Si + Pb_3O_4 is represented by Equation 4–8 (derived from data obtained from Anisimova et al. (2004) and Magomedov and Gadjiev (2008)). A graphic representation of the derivation of all the thermo-physical relationships for all the material properties is given in Appendix E.

$$\lambda_s = 3.415 \times 10^{-5} T^2 - 0.0896 T + 67.011 \quad \text{for } T < 1700$$
$$\lambda_s = 20.067 \quad \text{for } T \geq 1700 \qquad 4\text{-}8$$

There was also no reliable thermal conductivity data available for Sb_2O_3. Since Sb_2O_3 is used extensively as a fire retardant, it is expected to have an even lower thermal conductivity than other metal oxides (0.01- 40 $Wm^{-1}K^{-1}$). The lower end of this range was therefore assumed. The Sb_2O_3 further sublimates and decomposes at a low temperature and is expected to be in the gaseous phase when the reaction occurs, which would lead to an even lower thermal conductivity. The thermal conductivity of the solid mixture of Mn + Sb_2O_3 is represented in Equation 4–9 as derived from data obtained in International Atomic Energy Agency (2008).

$$\lambda_{Mn} = 0.0032 T + 1.8187 \quad \text{for } T \leq 1000\ K$$
$$= 5.04 \quad \text{for } T > 1000\ K \qquad 4\text{-}9$$

The density of the Si + Pb_3O_4 solid mixture is calculated as 4 276 kg/m^3 and the volume fraction of solids is 0.559. The heat capacity of the solid Si + Pb_3O_4 composition is derived as described in Equation 4–10 (Green and Perry, 2008, Desai, 1986, Dean, 1999, Garnier et al., 1979)

$$C_{p,0}(T) = 0.1089 T + 404.585 \quad \text{for } T < 1685\ K$$
$$C_{p,0}(T) = 537.933 \quad \text{for } T \geq 1685\ K \qquad 4\text{-}10$$

In order to account for the phase transitions undergone by the reagents and products, the latent heats are taken into account using the method described by Aldushin et al. (1987). This method is shown in Equation 4–11. The delta function in Equation 4–11 ($\delta(T–T_m)$) was approximated by a narrow Gaussian distribution centred on the applicable transition temperatures (T_m).

$$C_{p,s}(T) = C_{p,0}(T) + L\delta(T\text{-}T_m) \qquad 4\text{-}11$$

When first considering the Si + Pb_3O_4 composition, it is seen that the reaction mechanisms have been well explored. The reaction of Si + Pb_3O_4 is assumed to occur in the stages represented in **Schemes 4–5** to **4–7** (Al-Kazraji and Rees, 1979):

$$Pb_3O_4 \rightarrow 3PbO + ½O_2 \qquad \textbf{Scheme 4-5}$$

$$Si + O_2 \rightarrow SiO_2$$ **Scheme 4-6**

$$2PbO + Si \rightarrow SiO_2 + 2Pb$$ **Scheme 4-7**

As discussed earlier and described in **Scheme 4–5**, Pb_3O_4 will decompose to form PbO and O_2. PbO also undergoes the first phase transition and melts at 1163 K with a heat of fusion of 52.86 J/kg (Green and Perry, 2008). The next phase transition occurs at 1 700 K, where the Si melts with a heat of fusion of 1 411 J/kg (Green and Perry, 2008). When this temperature is reached, any unreacted PbO will further vaporise at a temperature of 1 745 K and a heat of vaporisation of 962 J/kg (Green and Perry, 2008). The SiO_2 will also melt when the temperature reaches 1 973 K with a heat of fusion of 146 J/kg (Green and Perry, 2008). The three resulting products can also vaporise if the temperature exceeds the boiling point. The lead product, which boils at 2 017 K with a heat of vaporisation of 849 J/kg, is the most likely to vaporise (Green and Perry, 2008). There is also the possibility of the SiO_2 boiling at a boiling point of 2 503 K with a heat of vaporisation of 5 751 382 J/kg (Yaws, 2010). The unreacted Si is not likely to vaporise as this only occurs at a temperature of 3490 K, but if the temperature reaches this point the heat of vaporisation (12 782 397 J/kg) will also be accounted for (Yaws, 2010). The effective heat capacity for the solid mixture is therefore derived as presented in Equation 4–12.

$$\begin{aligned} C_{p,s}(T) = Cp_0(T) &+ x_{Si}(1411)\,\delta(T\text{–}1700) + x_{Pb3O4}(52.86)\,\delta(T\text{–}1163) \\ &+ x_{SiO2}(147)\,\delta(T\text{–}1973) + x_{Pb}(849)\,\delta(T\text{-}2017) \\ &+ x_{SiO2}(5751382)\,\delta(T\text{–}2503) + x_{Pb3O4}(962)\,\delta(T\text{–}1745) \\ &+ x_{Si}(12782397)\,\delta(T\text{–}3490) \end{aligned}$$ 4-12

Now considering the Mn + Sb_2O_3 composition, the nature of this reaction is complex and a range of phase changes are possible. The first phase change expected is the sublimation of the Sb_2O_3 at 723 K with a heat of vaporisation of 631 504 J/kg (Centers, 1988, Golunski and Jackson, 1989)). The next phase change possible is the melting of the Mn at 1 493 K with a heat of fusion of 262 747 J/kg (Green and Perry, 2008). Furthermore, the Sb product will vaporise at 1 713 K with a heat of vaporisation of 1 603 706 J/kg (Green and Perry, 2008). Next, the MnO product will melt at 2 112 K with a heat of fusion of 766 873 J/kg (Yaws, 2014). The Mn will also vaporise if the reaction temperature reaches 2 425 K with a heat of

vaporisation of 4 200 146 J/kg (Green and Perry, 2008). The vaporisation of MnO only occurs at temperatures above 3 400 K, which is highly unlikely to occur, and will only do so if the reaction temperatures are found to reach close to this temperature. Two other possible phase changes are the MnSb and the MnO vaporising. There is, however, no information available about the boiling point or heat of vaporisation for MnSb, and it was therefore assumed to remain in the liquid phase within the reaction zone. The effective heat capacity of the solid mixture of Mn + Sb_2O_3 is therefore derived to Equation 4–13 from Equation 4–11.

$$C_{p,s}(T) = Cp_0(T) + x_{Sb2O3}(631504)\delta(T–723) + x_{Sb}(1604)\delta(T–1713) + x_{Mn}(263)\delta(T–1493) + x_{Mn}(4200)\delta(T–2425) + x_{MnO}(766873)\delta(T–2112) \quad 4\text{-}13$$

The density of the solid Mn + Sb_2O_3 mixture is calculated as 5 780 kg/m^3 and the volume fraction of solids measured was 0.693. The heat capacity of the solid composition is derived to Equation 4–14 (derived from Green and Perry (2008).

$$\begin{aligned} C_{p,0}(T) &= 0.3406\,T + 289.06 && for\ T < 1108\ \text{K} \\ &= 0.1203\,T + 446.24 && for\ 1108\ \text{K} \leq T < 1493 \\ &= 623.0982 && for\ 1493\ \text{K} \leq T \end{aligned} \quad 4\text{-}14$$

Sb_2O_3 is assumed to have completed the sublimation phase by 929 K, and a constant heat capacity is assumed above this temperature.

The solid heat transfer through the lead walls of the tube is described through the solid conduction model described in Equation 4–15.

$$\rho C_p \frac{\partial T}{\partial t} = \nabla \cdot (\lambda \nabla T) + Q \quad 4\text{-}15$$

The thermal conductivity of the lead tube wall was derived from experimental data by Hemminger (1989) as given in Equation 4–16.

$$\begin{aligned} \lambda_{lead} &= 41.186 - 0.02\,T && for\ T < 600\ \text{K} \\ \lambda_{lead} &= 7.8404 + 0.0129\,T && for\ T \geq 600\ \text{K} \end{aligned} \quad 4\text{-}16$$

The heat capacity of the lead in solid and liquid phase is given in Equation 4–17 (Green and Perry, 2008).

$$C_{p,0} = 0.04079\,T + 116.5139 \qquad for\ T < 600\ \text{K}$$

$$= 137.313 \qquad for\ T \geq 600\ \text{K} \qquad \text{4-17}$$

To account for the lead melting, the heat of fusion is taken into account as described by Aldushin et al. (1987) in Equation 4–11 and used in Equations 4–12 and 4–13. The heat of fusion of the lead is 24 716 J/kg at a melting point of 600 K (Green and Perry, 2008). The temperature-dependent heat capacity of the lead wall is described in Equation 4–18.

$$C_{p,\ Pb}(T) = C_{p,0}(T) + (24\,716)\,\delta(T–600) \qquad \text{4-18}$$

The solid heat conduction through the paint layer is described by the same solid conduction model as for the lead wall – the constant thermal properties used are listed Appendix F (Raghu and Philip, 2006).

The heat loss to the ambient atmosphere is expected to occur via natural convection and radiative heat transfer. The radiative heat transfer and convective heat loss from the paint surface is calculated with Equation 4–19. The emissivity of the paint is taken as 0.98 and the temperature-dependent heat transfer coefficient is described by Equation 4–20 (Cengel, 2006, American Society of Heating, 1997).

$$n_d \cdot(\lambda \nabla T) = \epsilon\sigma(T_{amb}^4 – T^4) + h_{conv}(T_{ext} – T) \qquad \text{4-19}$$

$$h_{conv} = 1.32\ (\Delta T/\ell_c)^{0.25} \qquad \text{4-20}$$

The characteristic length (ℓ_c) was, in this case, taken as the outside diameter of the element due to the small and thin nature of the paint layer on the tube. ΔT indicates the difference in temperature between the surface of the paint and the surrounding air. The values of all other constant parameters are listed in **Table F.1** of Appendix F.

4.2 GEOMETRY AND MESHING

The results obtained from the numerical model were compared to those from the IR camera. The model was therefore set up under precisely the same conditions as the delay elements produced for the IR camera measurements. The delay elements produced for experimental testing consisted of 100 mm long lead-drawn elements coated on the outside with high temperature-resistant matt black enamel paint. The assembly of these elements is shown in **Figure 3-11**. The dimensions and characteristics of the lead-drawn elements produced and modelled for the two reactions under investigation are given in Appendix F. The geometry of the lead-drawn delay element model is shown in **Figure 4-4** in both 2D and 3D views.

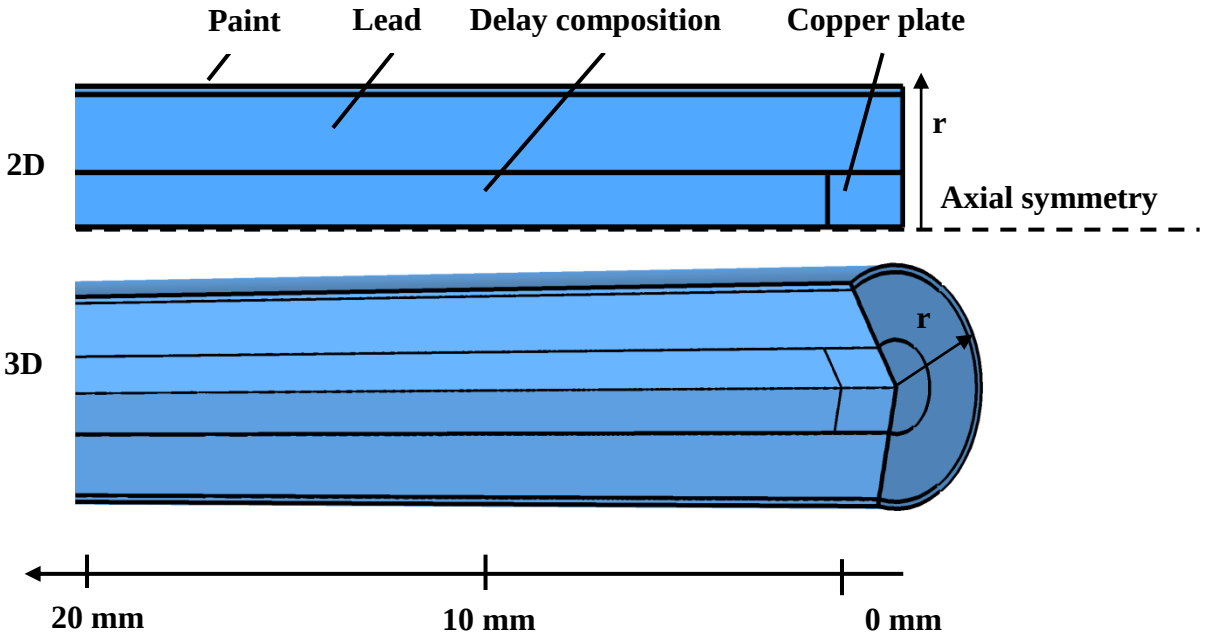

Figure 4-4: Geometry of the lead-drawn delay element model in 2D and 3D views

The mesh was created from triangular elements and the size was kept almost constant throughout the model. Adaptive mesh refinement was also evaluated. In this technique, the mesh is redrawn after every time step according to the variable gradients calculated for the previous time step. However, since very small time steps had to be used to solve the non-linear equations, this technique added additional time to find the solution. The use of differently sized elements in the different model domains was also evaluated, but optimum solutions were found for a uniform element size distribution. In order to determine the optimum element size, a mesh independence study was performed.

Since the rate of the reaction differed in orders of size for the two compositions (and therefore also the gradients in solutions) the analysis was done for both compositions separately. The mesh independence was analysed by solving the model for different-sized elements and using the peak combustion temperature as a convergence criterion.

Since the burn rate is an indirect result obtained from the model, variations could be amplified in more than one calculating variable and lead to local minima results. It was therefore decided that using a direct model variable would result in more systematic increases and would deliver global minima solutions in the study. The mesh element size was systematically decreased up to the point where a variation in peak reaction temperature of less than 1% was obtained in comparison to the temperature obtained from the previous mesh size. In order to reduce the time required to solve the model with the very fine meshes, the mesh independence study was performed on only 50 mm long elements and not the full length of 100 mm. The combustion front was found to stabilise in the first 20 mm and the additional 50 mm would only add computational time without adding value to the mesh independence study. The mesh convergence results for both the Mn + Sb_2O_3 and the Si + Pb_3O_4 reactions are shown in **Figure 4-5**. All model calculations were performed on an Intel Core i7-4720HQ with 32 GB of DDR3 random-access memory in conjunction with a 256 GB solid-state drive.

(a)

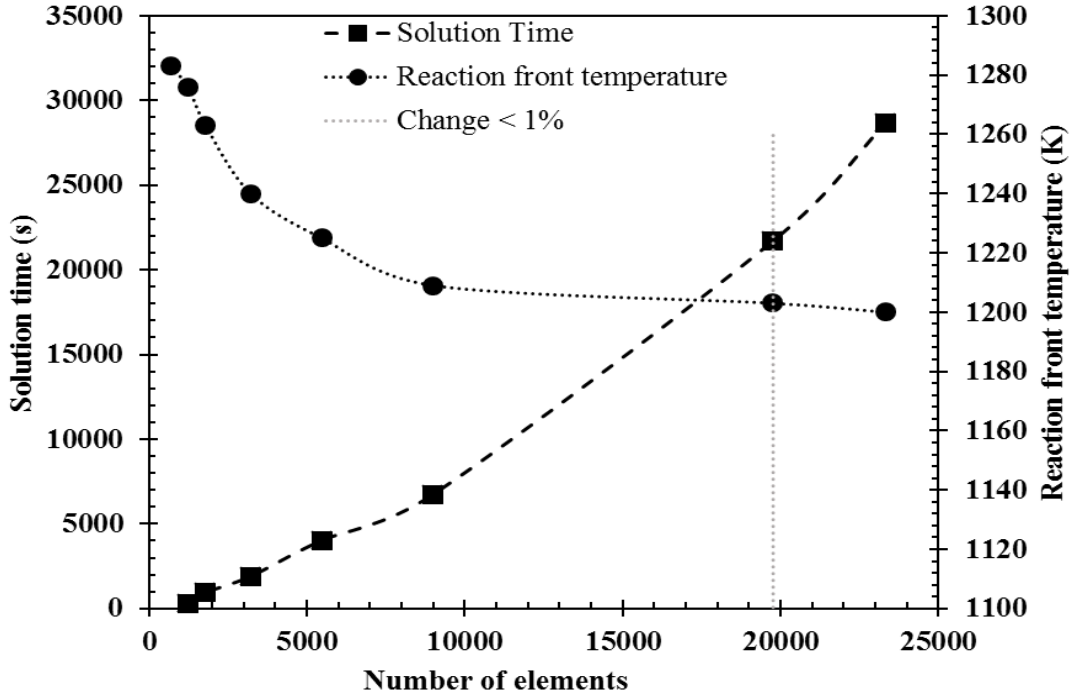

(b)

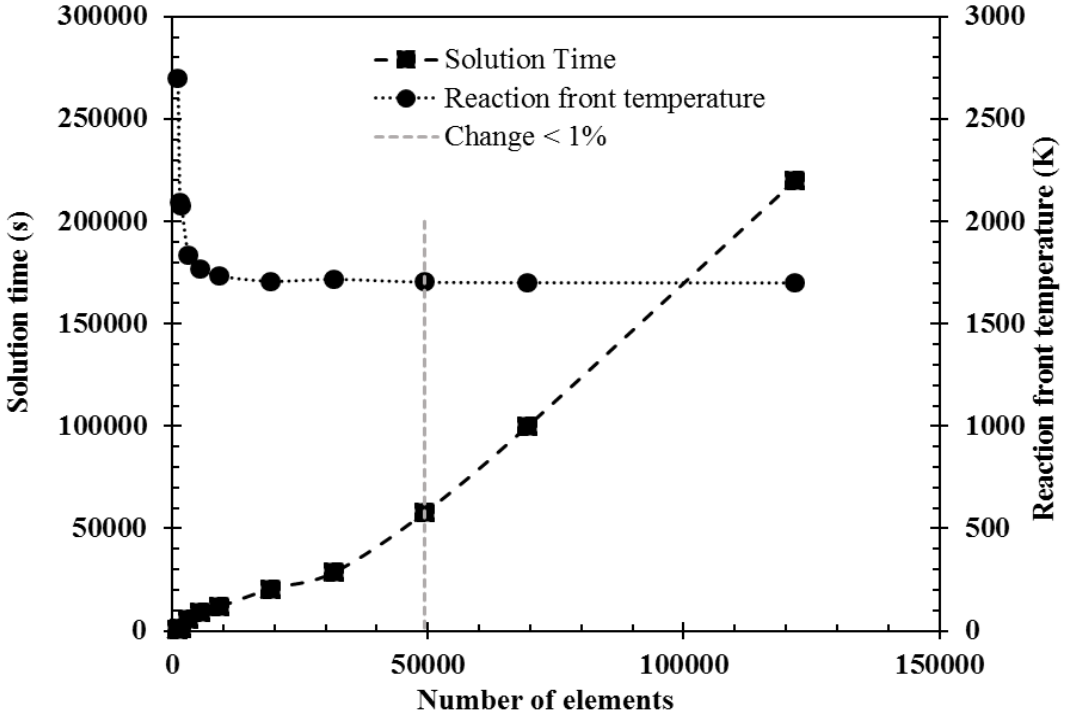

Figure 4-5: Results from the mesh independence study for (a) the Mn + Sb_2O_3 model and (b) the Si + Pb_3O_4 model

The final mesh parameters used in all other simulations, as determined from the mesh independence study, are shown in **Table 4-2**. **Figure 4-6** shows a section of the mesh for each reaction as used in the final simulations.

Table 4-2: Mesh parameters used in all simulations as determined from the mesh independence study and applied for a 100 mm long element

Mesh parameter	**Mn + Sb_2O_3 model**	**Si + Pb_3O_4 model**
Total number of elements	38 727	986 688
Average element area	8 946.92 µm^2	3 583.74 µm^2
Average equivalent diameter	106.73 µm	67.55 µm
Average element quality	0.986	0.989
Average growth rate	1.015	1.011

(a)

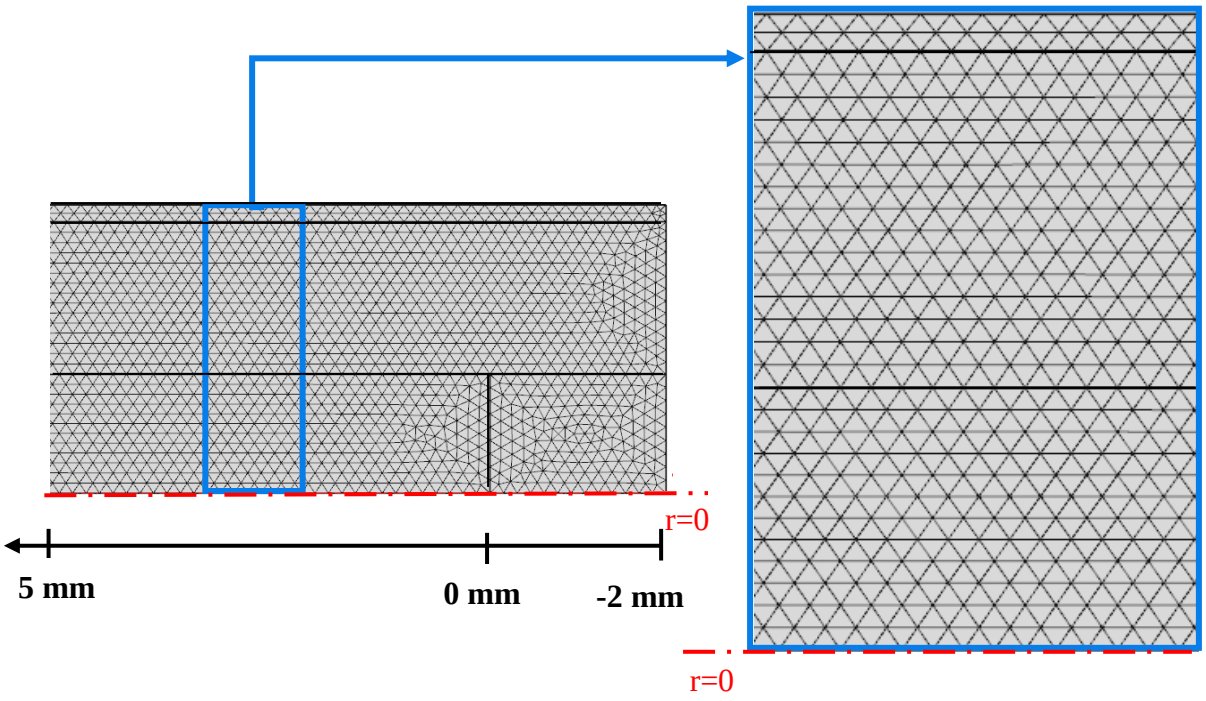

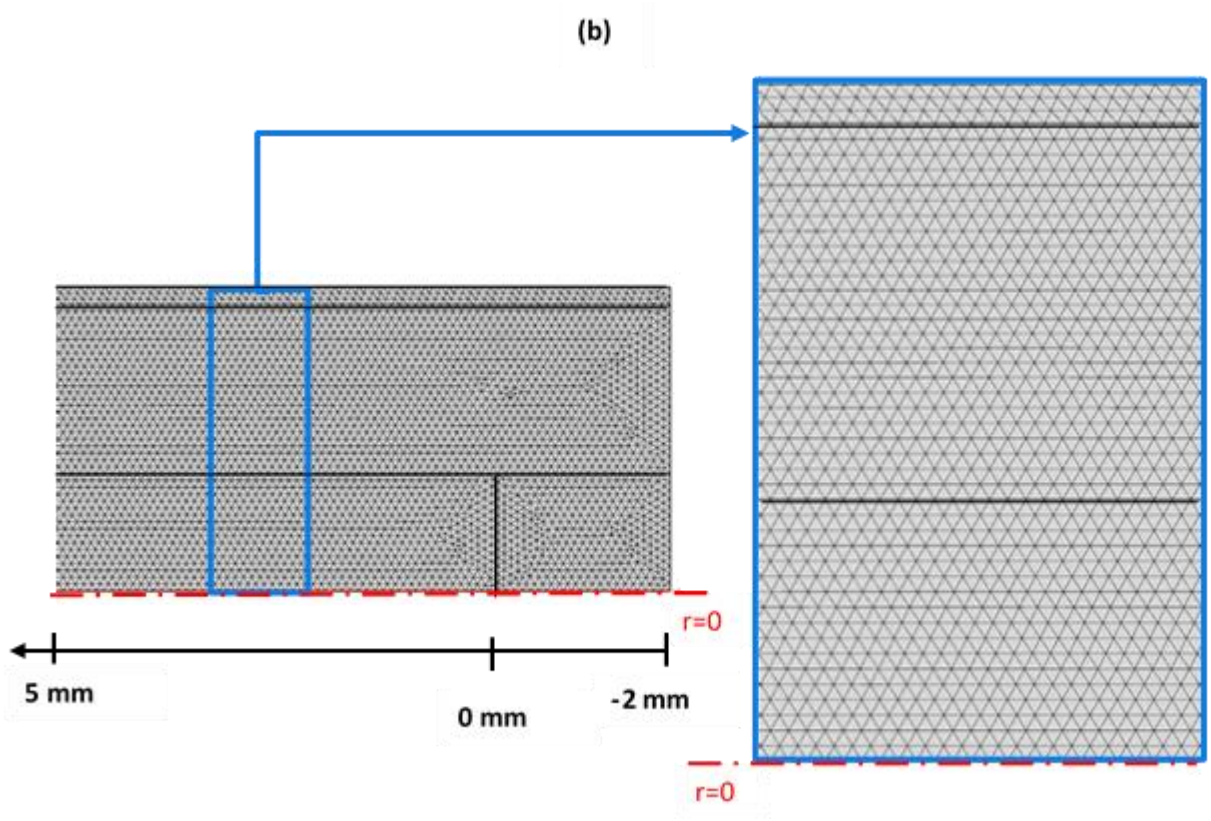

Figure 4-6: Finite element model showing a section of the meshed elements used for the numerical computations for the models of (a) Mn + Sb_2O_3 and (b) Si + Pb_3O_4

4.3 NUMERICAL SOLUTIONS

The pseudo steady-state solution at each time step was calculated using the Newtonian solver. The transient equations were solved using the PARDISO solver with row pre-ordering according to a nested dissection multi-thread algorithm. The Jacobian was calculated at every time step to ensure that convergence to a tolerance of 10^{-3} was reached.

One of the major problems with simulating pyrotechnic reactions is the initiation of the reaction in the model. Since there is no existing numerical model of how the shock tube ignites the pyrotechnic compositions, another means of initiating the reaction is required. In Section 2.4.2, various initiation mechanisms used in previous studies were discussed. It was decided that a combination of the methods used by Ivleva et al. (1983) would be used to initiate the simulated delay composition. A temperature pulse applied to the front of the delay element should serve as a way of initiating the pyrotechnic delay composition in a way similar to a starter composition.

Furthermore, it was decided that a 2 mm copper plate would be added to the front of the element, against which the temperature pulse would then be applied. The copper plate ensures that the heat being delivered to the delay composition from the temperature pulse is evenly distributed over the surface of the element before it is delivered to the delay composition. The use of indirect heat delivery would also minimise the effect of the heat transfer resistance at the interface of the copper plate and the delay composition.

In order to simulate the ignition as closely as possible to the ignition of a starter composition, the temperature pulse was used to simulate a 10 mm section of starter composition. The adiabatic flame temperature of the starter composition was found to be 1 683 K from the Ekvi thermodynamic simulations, shown in **Figure 4-1**. The burn rate of the starter composition measured with the IR camera was 149.05 mms^{-1} and therefore a 10 mm section would burn for about 67.09 ms. The temperature pulse was therefore delivered to the bottom surface of the copper plate for 67.09 ms through a Gaussian distribution with a peak temperature of 1 683 K. **Figure 4-7** shows how the initiation of the reaction occurs using this method of ignition.

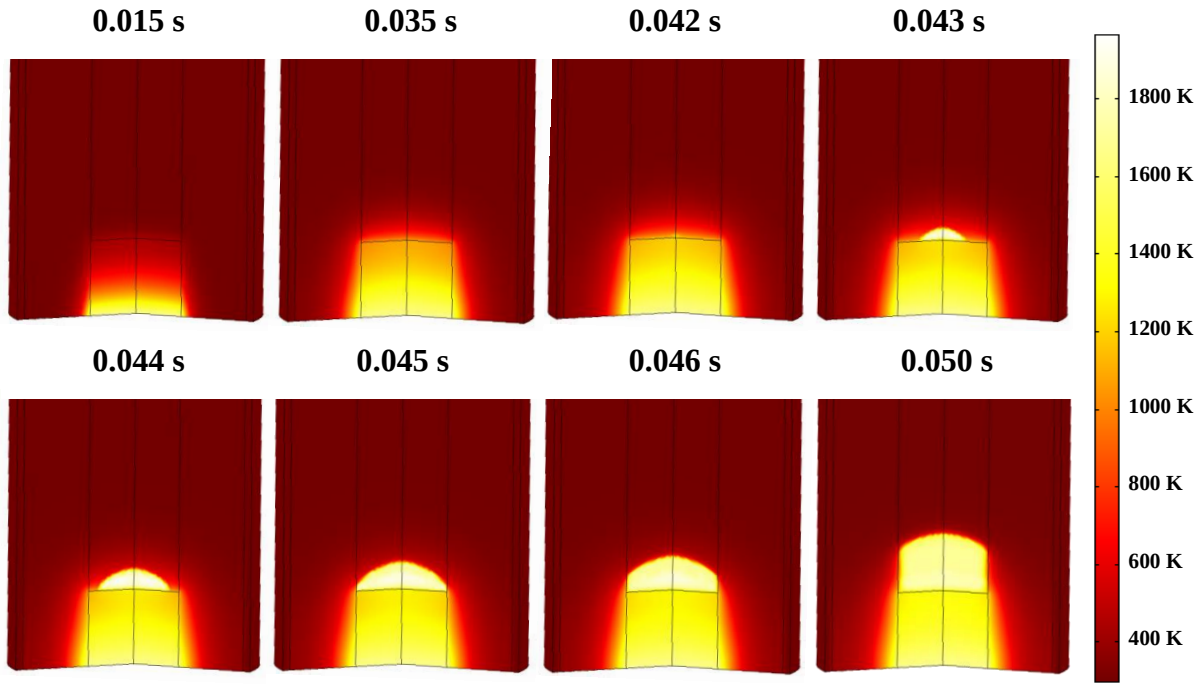

Figure 4-7: Numerical simulation of the temperature profiles of the first 30 mm section of the element showing the initiation of the combustion wave of the 36 wt.% Si + Pb_3O_4 composition from the temperature pulse applied to the bottom of the copper plate

The only parameters that are not available are the kinetic parameters (n, m, k_0 and E_a) from Equations 4–2 and 4–3. The data from the numerical simulations were compared to the IR camera measurements in order to fit these kinetic parameters. These four parameters can, however, not be changed independently, as this would change the burn rate. The fitting therefore had to comprise combinations of the four parameters that provide the best fitting temperature profile while still maintaining the desired burn rate. The temperatures change over time as well as over the length of the element. The fitting therefore had to be optimised in both dimensions. **Figure 4-8** shows the change in one temperature profile over the length of the element as well as over time for various combinations of kinetic parameter values. The comparison of these profiles to the IR camera profile is also shown. This method was followed to obtain the best fitting kinetics for both the Mn + Sb_2O_3 and the Si + Pb_3O_4 models. Fitting of only the Si + Pb_3O_4 model is shown in **Figure 4-8** to show the methodology.

In **Figure 4-8** it can be seen that the kinetic parameters have a much bigger influence on the temperature profile over the length of the element than over the temporal profile. Least mean square analysis was performed in both dimensions to find the best fitting kinetics.

(a)

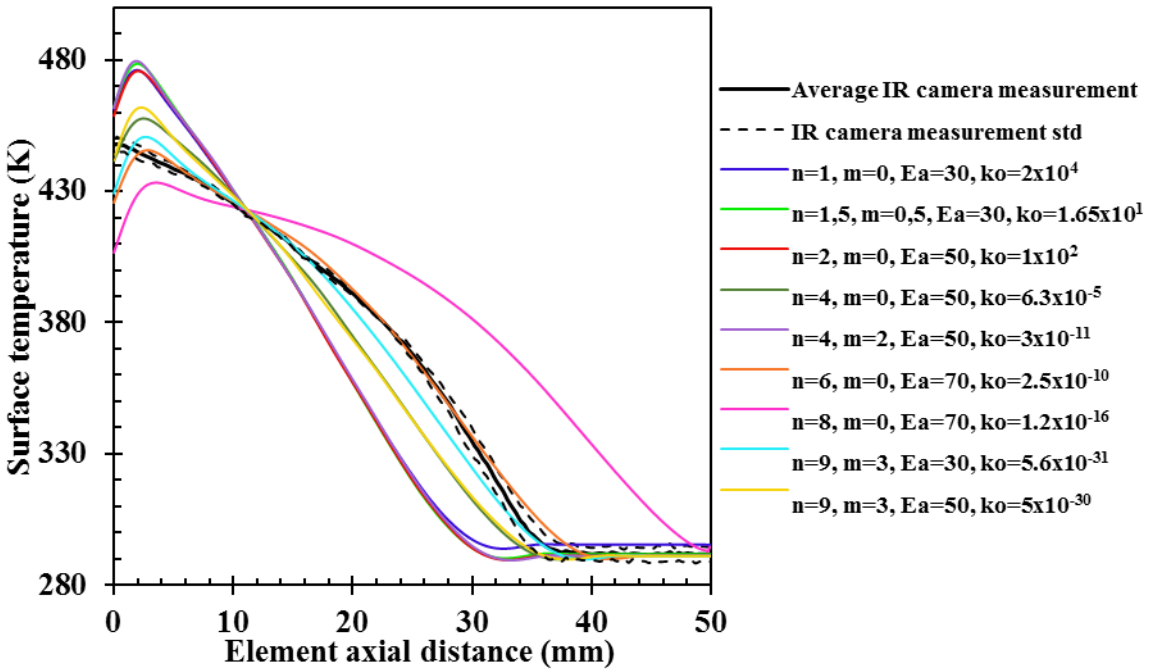

(b)

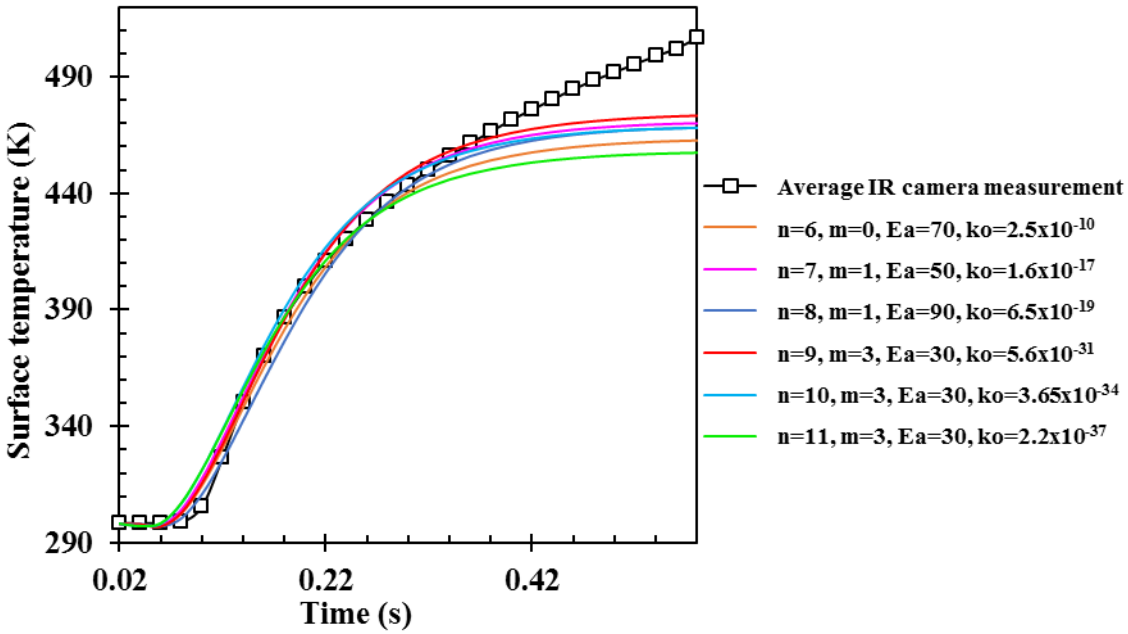

Figure 4-8: Surface temperature profiles for the Si + Pb_3O_4 model obtained from the numerical model at various combinations of the kinetic parameters (n, m, k_o, E_a), compared to the temperature profile measured using the IR camera for (a) changes at a single point over the duration of the reaction and (b) changes over the length of the element at a single point in time

5 RESULTS AND DISCUSSION

5.1 Mn + Sb_2O_3/MnO_2 PACKING

The packing of the Mn + Sb_2O_3 and Mn + MnO_2 compositions was investigated to determine the effect of the particle sizes of both materials on the packing arrangements of the composition, along with their impact on the burn rate. The different sized Mn, MnO_2 and Sb_2O_3 materials used for this study are listed in **Table 3-1**, along with all related characteristics described in Section 3.1.

Particle packing in compacts were imaged with a JEOL JSM-IT300LV scanning electron microscope (SEM). The lead-drawn delay elements containing all combinations of fuel (Mn) and oxidants (Sb_2O_3 and MnO_2) were sectioned and imaged to obtain a visual representation of the packed compositions. The images for a few of these compositions are shown in **Figure 5-1**. For the Mn + Sb_2O_3 compositions it was found that in all cases the Mn particles were significantly larger than the Sb_2O_3 particles. No discernible packing arrangement was found, and each of the Mn particles was encased in a 'sea' of Sb_2O_3 particles. There was almost no contact between the fuel particles themselves, but there was a large amount of contact between the oxidant particles and a single fuel particle. The largest number of contact points existed between the oxidant particles themselves. It was further found that the Sb_2O_3 had an attraction to the Mn particles and a layer of Sb_2O_3 particles stuck to the surface of any Mn particle. This can be seen in **Figure 5–1 (b)**. This is likely due to the static nature of Sb_2O_3. Sb_2O_3 has been found to be naturally electrostatically charged, which likely leads to this 'sticking' of small oxidant particles to the Mn particles. This greatly assisted in facilitating proper mixing and prevented particle segregation afterwards.

The Mn + MnO_2 packing was found to differ slightly from that of Mn + Sb_2O_3 since the MnO_2 particle size distributions were much wider. It was therefore found that the Mn and large agglomerates of MnO_2 were both encased in the sea of small MnO_2 oxidant particles. It can further be seen in **Figure 5–1 (d)** that there was no 'sticking' of small oxidant particles to the large fuel particles, and therefore not the same attraction between the two materials.

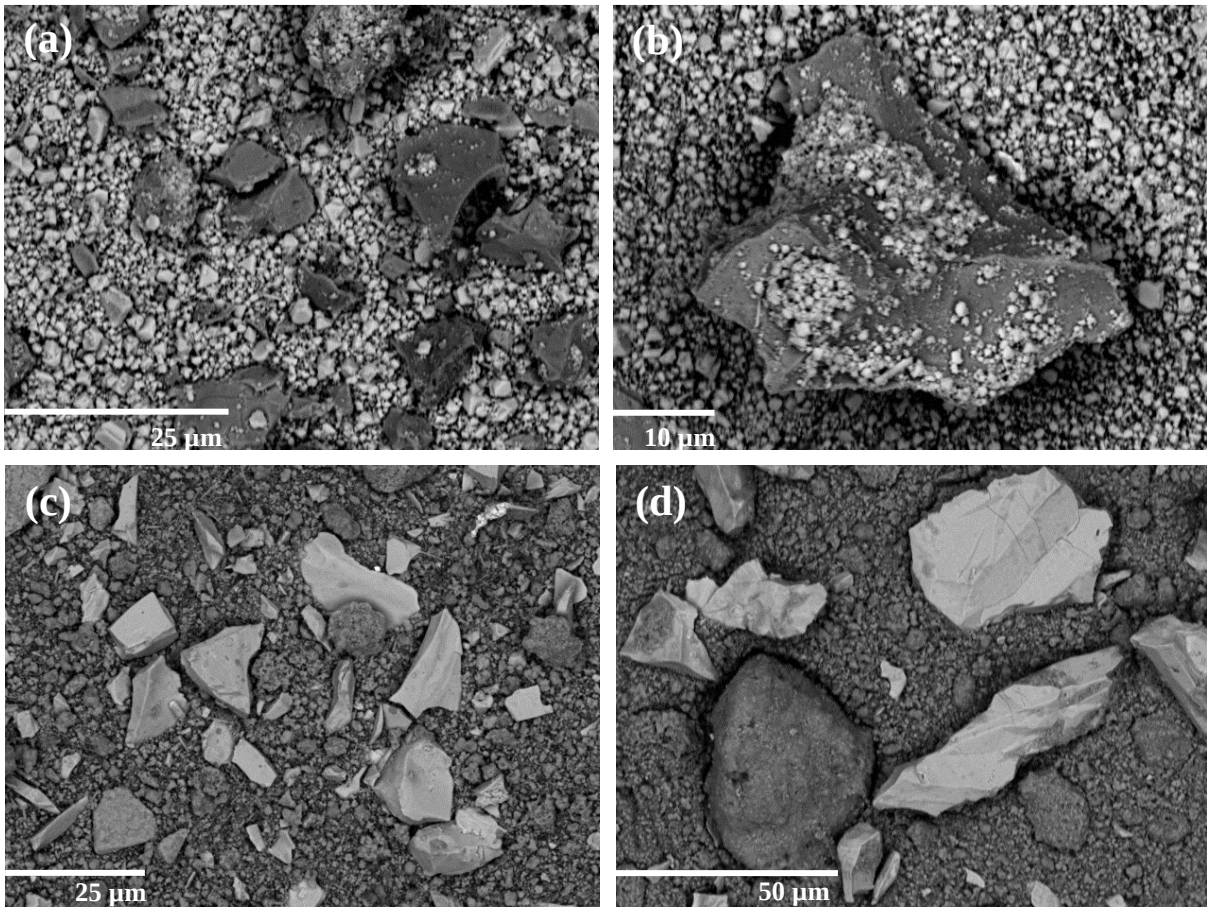

Figure 5-1: SEM images of the packed delay compositions sectioned from lead tubes containing (a) $Mn_I + Sb_2O_{3C}$, (b) $Mn_C + Sb_2O_{3A}$, (c) $Mn_I + MnO_{2C}$ and (d) $Mn_B + MnO_{2C}$

In order to evaluate the effect of the particle packing on the burn rate, every combination of fuel and oxidant of Mn with Sb_2O_3 or MnO_2 was tested. The elements were prepared in lead tubes and tested using the industrial testing technique. Unfortunately, only one of the MnO_2 samples (MnO_{2C}) reacted with the Mn. The reason for this is not yet understood. The results of the burn rates measured for the various sized particles of Mn + Sb_2O_3 and Mn + MnO_2 are shown in **Figure 5-2**. In **Figure 5-2** the apparent 'nano' structured particles are shown with open symbols and the solid micron structured particles are shown with solid symbols. The effective mixture particle size was used to evaluate the burn rate effect. The effective mixture particle size was calculated as the volume-fraction-weighted harmonic mean ($<d_p>$) of the fuel and the oxidant particle sizes. The proportionality constant $P = u<d_p>$ was determined from a least-squares fit. The results shown in **Figure 5-2** indicate that the burn rate could be proportional to the inverse of the mean particle size, which corresponds to the indications of Armstrong (1990) and Aldushin and Khaikin (1974). The large uncertainties in both values of P, however, indicate that the particle size is not the only factor that influences the burn rate.

(a)

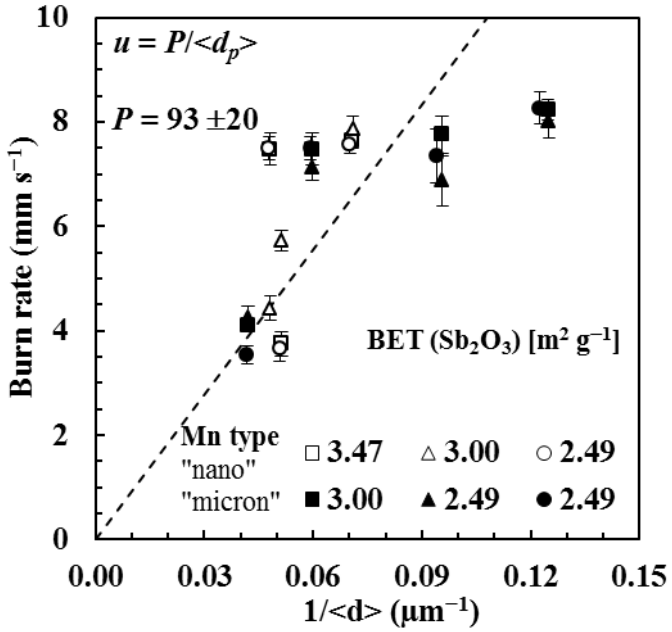

(b)

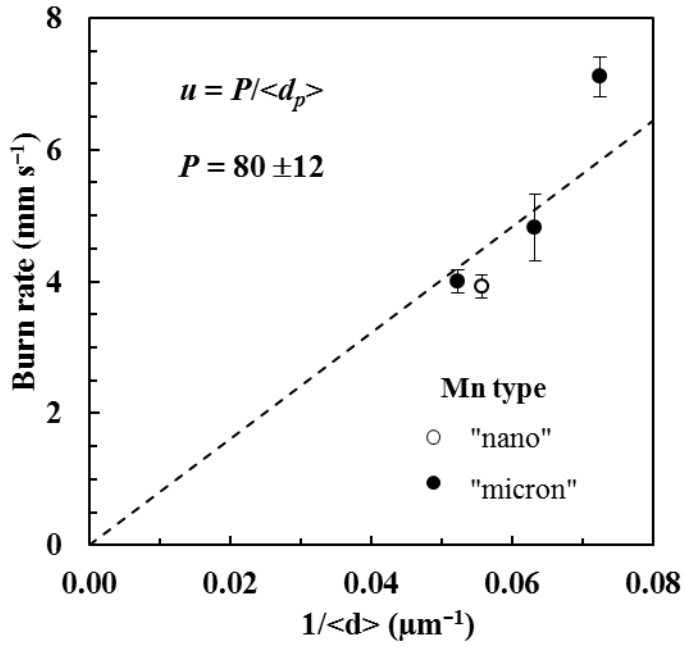

Figure 5-2: The effect of particle size on the burn rates containing (a) 36 wt.% Mn with Sb_2O_3 and (b) 38.7 wt.% Mn with MnO_2. d_p is the volumetric-fraction-weighted harmonic mean particle size of the mixture

One factor that could have a significant effect on these results is the porosity of the particles. As found in Section 3.1, the 'nano'-sized particles obtained were not truly nano-sized, but were rather an agglomerate of nano-sized particles fused together. This leads to one large micron-sized particle which is porous throughout its structure. This can affect the results shown in **Figure 5-2** in several ways. Firstly, the particle size parameter could be inaccurate. The overall size of a 'nano-sized' particle would contain several air spaces comparable to a solid micron-sized particle, which contains no air spaces. Another effect of the porosity is the decrease in thermal conductivity which, according to Equations 2–5 to 2–8 leads to a decrease in the burn rate. The porosity, on the other hand, facilitates the transport of gaseous or liquid phase reagents into contact with solid phase reagents. This would increase the mass diffusivity and lead to an increase in the burn rate. These factors all have opposing effects on the burn rate, the dominating factor depending on the specific composition. Other factors that could influence these results are particle shapes, mixing efficiency and reagent preparation methods. Since the reagents are from different suppliers and could have been prepared in different ways, the effect of these methods on the reactivity is not known at this stage.

The effect of local deviations from the stoichiometry within the mixtures could also influence these results. In order to evaluate this, the effect of variations in the amount of fuel on the burn rate was also evaluated. The fuel and oxidant particle sizes were held constant by using only Mn_B and Sb_2O_{3C} as fuel and oxidant. The volumetric ratio represents the volume oxidant to the volume fuel. The results of this analysis are shown in **Figure 5-3**. In the preparation methods currently used, the packing density was relatively insensitive to the fuel content of the composition, even though the volumetric ratio decreased from about four to unity over the range of experimental compositions. **Figure 5-3** further shows that the burn rate for Mn + Sb_2O_3 increases linearly even after the composition becomes fuel rich. This is attributed to the finding of a secondary intermetallic reaction occurring after the theoretical stoichiometry of the redox reaction. This was depicted in the Ekvi thermodynamic simulations shown in **Figure 4-1** and verified with XRD analysis in **Figure 4-2**. This additional intermetallic reaction adds exothermicity to the reaction even after the theoretical stoichiometry is reached, which leads to an additional increase in burn rate in fuel-rich compositions. In order to further evaluate the impact of the composition on the packing of the mixture, the compacted mixtures were imaged with a JEOL JSM-IT300LV (SEM). The images are shown in **Figure 5-4** for the composition of Mn_B with Sb_2O_{3C} containing various amounts of fuel.

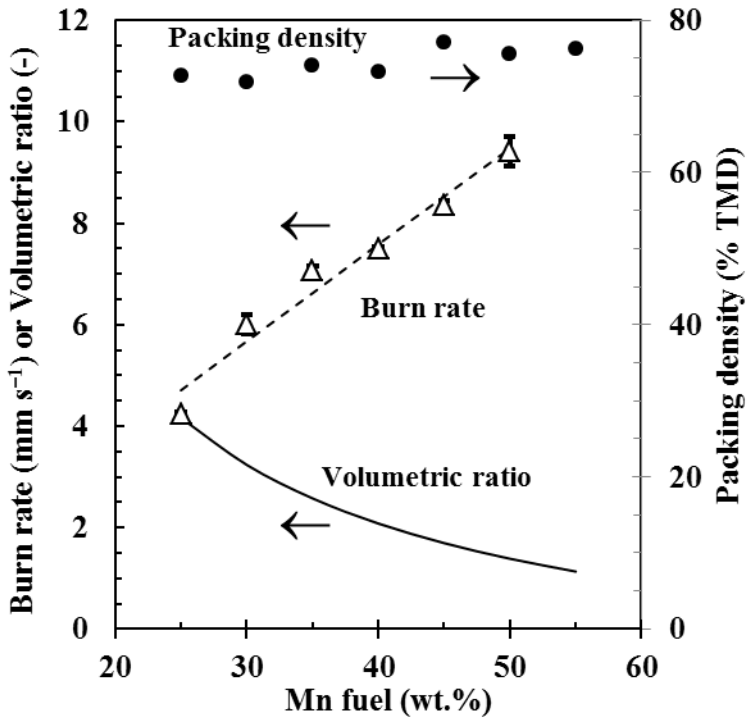

Figure 5-3: Experimental packing densities, calculated volumetric ratios and burning rates as a function of fuel content for the composition containing Mn_B and Sb_2O_{3C} at various fuel contents

The SEM images in **Figure 5-4** clearly show an increase in the number of fuel particles in relation to the number of oxide particles. When considering the image of the composition containing 25 wt.% Mn, it is surprising that any reaction can occur with the minimal amount of fuel particles present in the two-dimensional view. This is indicative of the sublimation undergone by the Sb_2O_3 oxide at a low temperature. The oxide is therefore in the gaseous phase when the reaction occurs, and the reaction is therefore not limited by physical contact or diffusion. The gas particles are free to move around and fill all the contact requirements of the fuel in order to propagate the reaction.

The same analysis was conducted with Mn_B as a fuel and MnO_{2C} as an oxidant, but the composition was found only to burn over a narrow region of fuel content. Burn rate measurements could only be obtained at 38.7 and 45 wt.% fuel with burn rates of 7.57 (±0.18) mms^{-1} and 4.98 (±0.03) mms^{-1} measured respectively. This reduction in burn rate for fuel rich compositions are consistent with the Ekvi simulations performed on the Mn + MnO_2 reactions shown in **Figure 5-5**.

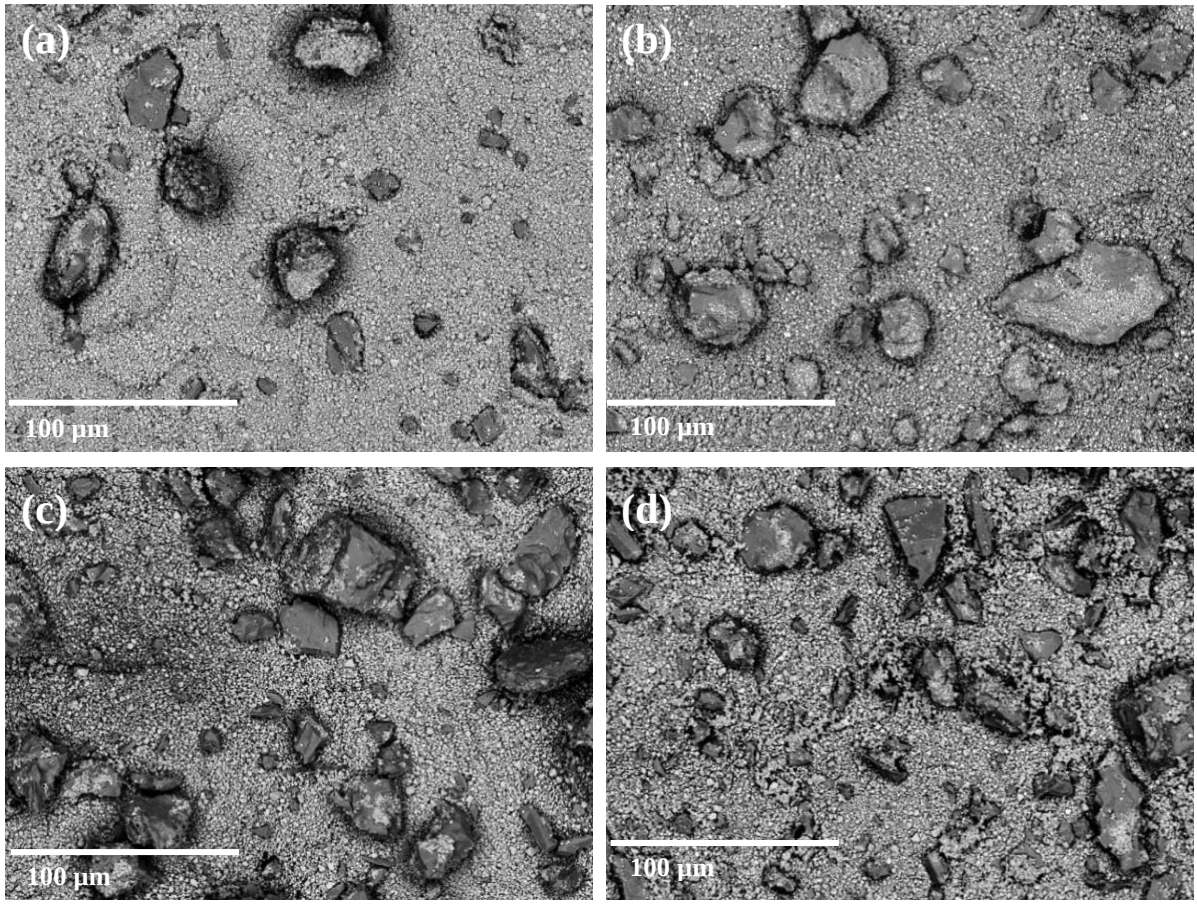

Figure 5-4: SEM images of the packed composition containing Mn_B and Sb_2O_{3C} with fuel contents of (a) 25 wt.%, (b) 36 wt.%, (c) 45 wt.% and (d) 50 wt.%

SEM images of the packed Mn + MnO_2 composition were also taken and are shown in **Figure 5-6**. The composition containing 25 wt.% fuel show very few Mn particles visible in the sea of MnO_2 particles. This can be attributed to the composition burning only at higher fuel contents. The adiabatic flame temperatures modelled through the Ekvi simulations indicate that the temperature varies between 1 000 K and 2 000K for compositions containing between 20 and 80 wt.% fuel. As discussed, from the TGA results in Section 3.1.4, the final decomposition step of MnO_2 only occurs above 1 473 K, which corresponds to the predicted adiabatic flame temperatures of between 20 wt.% and 60 wt.% Mn. Swanepoel et al. (2010) obtained burn rate results between 40 wt.% and 75 wt.% fuel, which would indicate, when considering the adiabatic flame temperatures, that the reaction occurs after the first reduction step of MnO_2 to Mn_2O_3. The reason for the prepared compositions only burning between 38 and 45 wt.% Mn is therefore still unclear. The Ekvi simulations indicate that the adiabatic flame temperature decreases after peaking at 40 wt.% Mn. This corresponds to the decrease in burn rate measured between the 38.7 wt.% and 45 wt.% fuel samples.

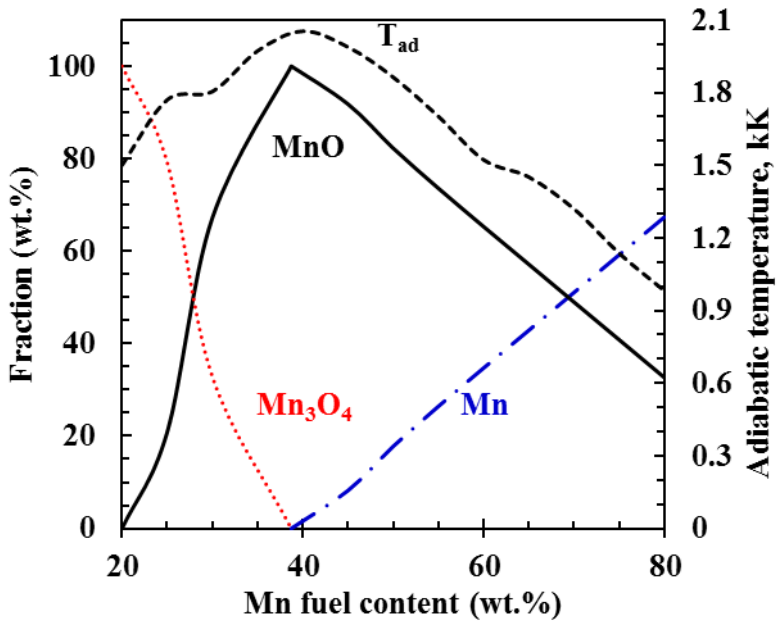

Figure 5-5: Ekvi simulations for the Mn + MnO_2 reaction showing the adiabatic flame temperatures and product formations over a range of fuel content

SEM images of the packed Mn + MnO_2 composition were also taken, which are shown in **Figure 5-6**. The composition containing 25 wt.% fuel show very few Mn particles visible in the sea of MnO_2 particles. This could be attributed to the composition burning only at higher fuel contents. The adiabatic flame temperatures modelled through the Ekvi simulations indicate that the temperature varies between 1 000 K and 2 000 K. As discussed, according to the TGA results in Section 3.1.4 the final decomposition step of MnO_2 only occurs above 1 473 K. The reaction is therefore only expected to occur above 1 473 K, which corresponds to the predicted adiabatic flame temperatures between 20 wt.% and 60 wt.% Mn. Swanepoel et al. (2010) obtained burn rate results between 40 wt.% and 75 wt.% fuel, which would indicate (when considering the adiabatic flame temperatures) that the reaction occurs after the first reduction step of MnO_2 to Mn_2O_3. The reason for this composition only burning between 38 wt.% and 45 wt.% Mn is therefore still not clear.

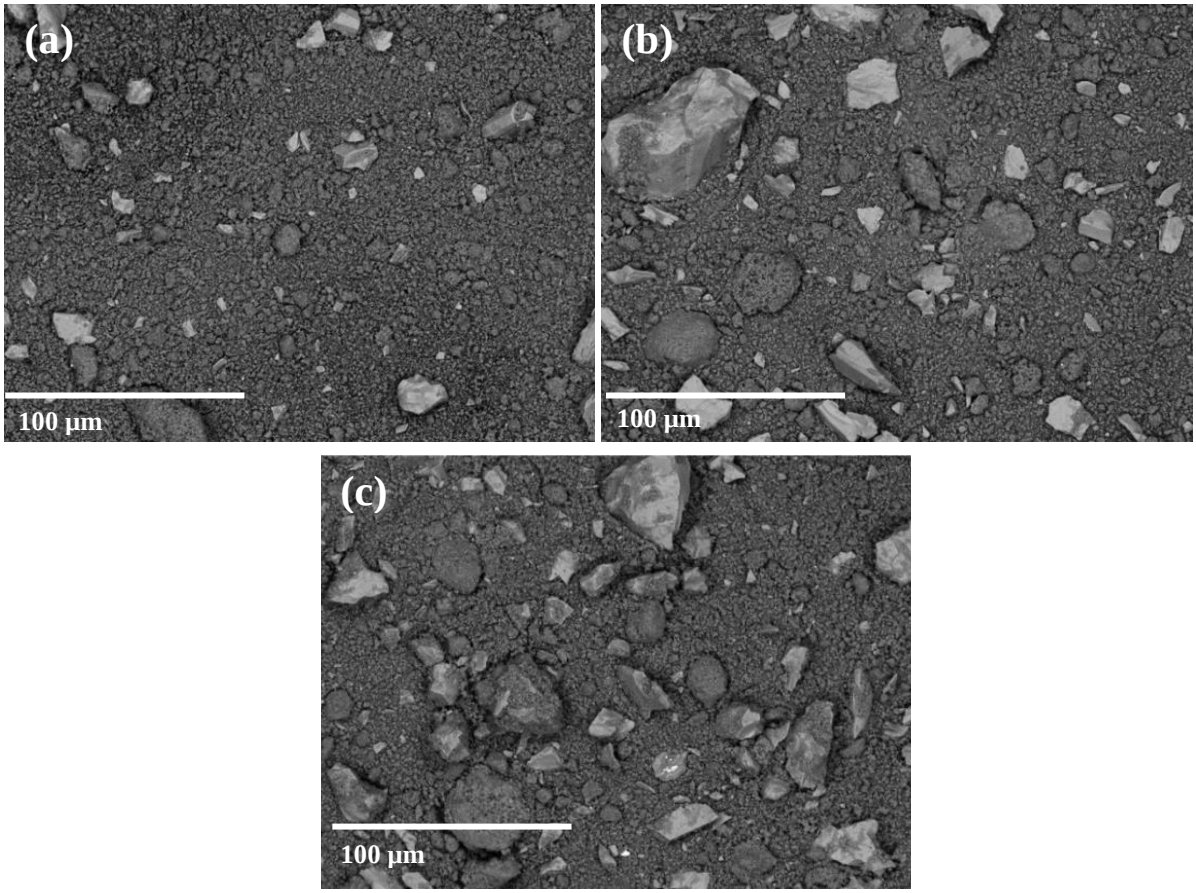

Figure 5-6: SEM images of the packed Mn_B with MnO_{2C} composition with (a) 25 wt.%, (b) 38 wt.% and (c) 45 wt.% fuel

5.2 BURN RATE MEASUREMENT TECHNIQUE

One of the objectives of the study was to develop and evaluate a new method for measuring the burn rates of pyrotechnic delay elements. The method was required to eliminate some of the problems with other commonly used techniques. From the discussion in Section 3.3, it was decided to use an IR camera to measure the burn rates. **Figure 5-7** shows the progression of a fast-burning (Si + Pb_3O_4) composition and a slow-burning (Mn_H + Sb_2O_{3D}) composition captured by the IR camera.

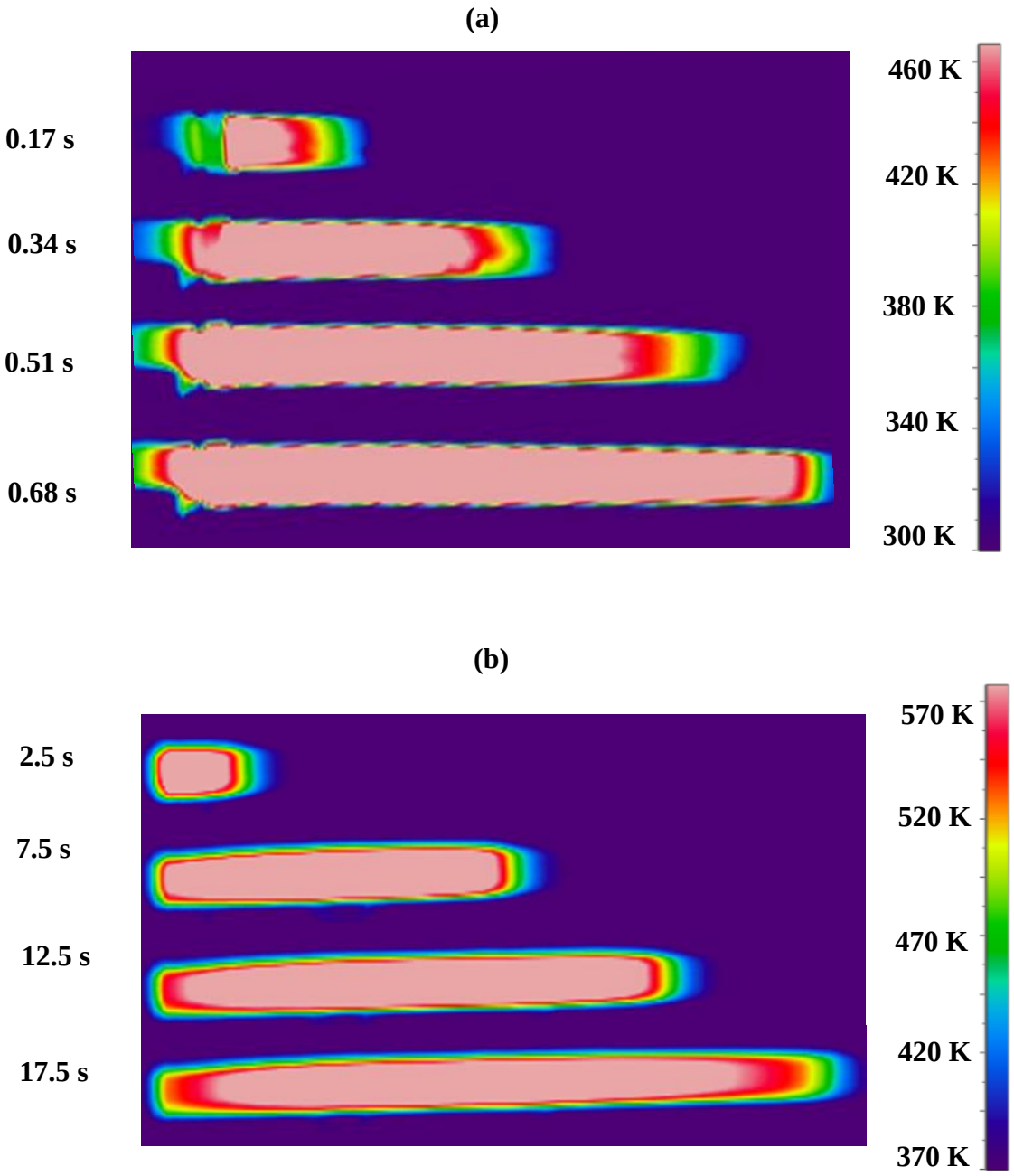

Figure 5-7: Propagation of (a) a fast-burning Si + Pb_3O_4 composition and (b) a slow-burning Mn + Sb_2O_3 composition captured by the IR camera

The average burn rates measured using the IR camera were compared to those obtained by two other commonly used techniques, the industrial detonator test and the thermocouple test, which were described in Section 3.3 in detail. **Figure 5-8** shows the average burn rates measured for compositions containing Mn + Sb_2O_3 at 36 wt.% Mn and Si + Pb_3O_4 at various fuel contents ranging from 30 wt.% to 55 wt.% Si measured using all three techniques. The results are also shown in **Table G- 1** in Appendix G.

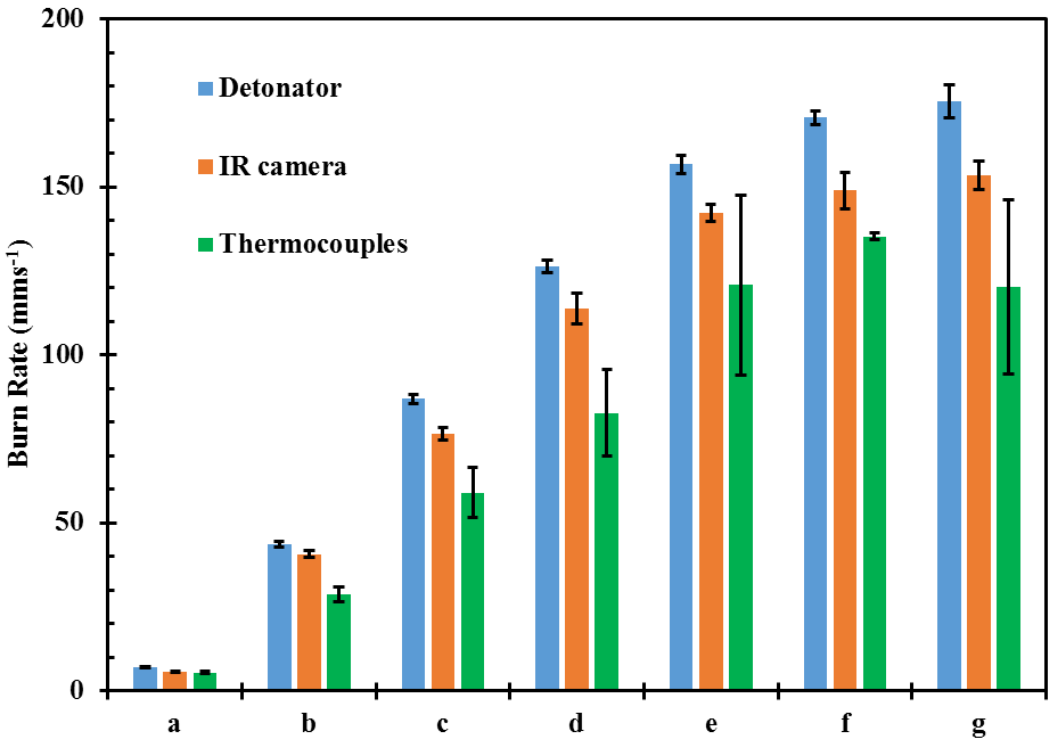

Figure 5-8: Comparison between the burn rates measured using the IR camera, the commercial detonator test and thermocouple tests of compositions containing (a) 36 wt.% Mn + Sb_2O_3 and (b) to (g) Si + Pb_3O_4 containing 30 wt.% to 55 wt.% Si

It was not surprising to find that the burn rates measured using the different techniques were not the same. Each method measures different variables and the detonators are not assembled in exactly the same way. The fully assembled detonators use a sealing composition and are also placed in an additional aluminium tube. When comparing the burn rates, the IR camera measured burn rates were much closer to those obtained by the commercial detonator technique than those measured using the thermocouples. Furthermore, the standard deviations of the results obtained from the IR camera method are of the same order as the results from the detonator burn rates. The thermocouple method, on the other hand, resulted in very large standard deviations. The thermocouples used in these tests were too big and their response times were too slow to accurately capture the burn rates of the elements. Very small thermocouples therefore have to be used to obtain more consistent results. The IR camera results were consistently repeatable and were found to be reliable. The progression of the temperature profiles measured using the IR camera for both the slow-burning and the fast-burning delay compositions over the length of the element are shown in **Figure 5-9**.

The temperature profiles shown in **Figure 5-9** indicate that the fast-burning Si + Pb_3O_4 profiles are not yet fully developed. The slow-burning Mn + Sb_2O_3 profiles, on the other hand, are fully developed. The burn rates measured for these slow-burning compositions can therefore be assumed to be reliable, whereas the fast-burning compositions need modelling to verify the burn rates measured. From these results, it was decided that the Mn + Sb_2O_3 profiles could be used to calibrate a numerical model for predicting the burning behaviour of the delay elements. The model could then also be applied to verify the burn rates measured for the fast-burning delay composition.

(a)

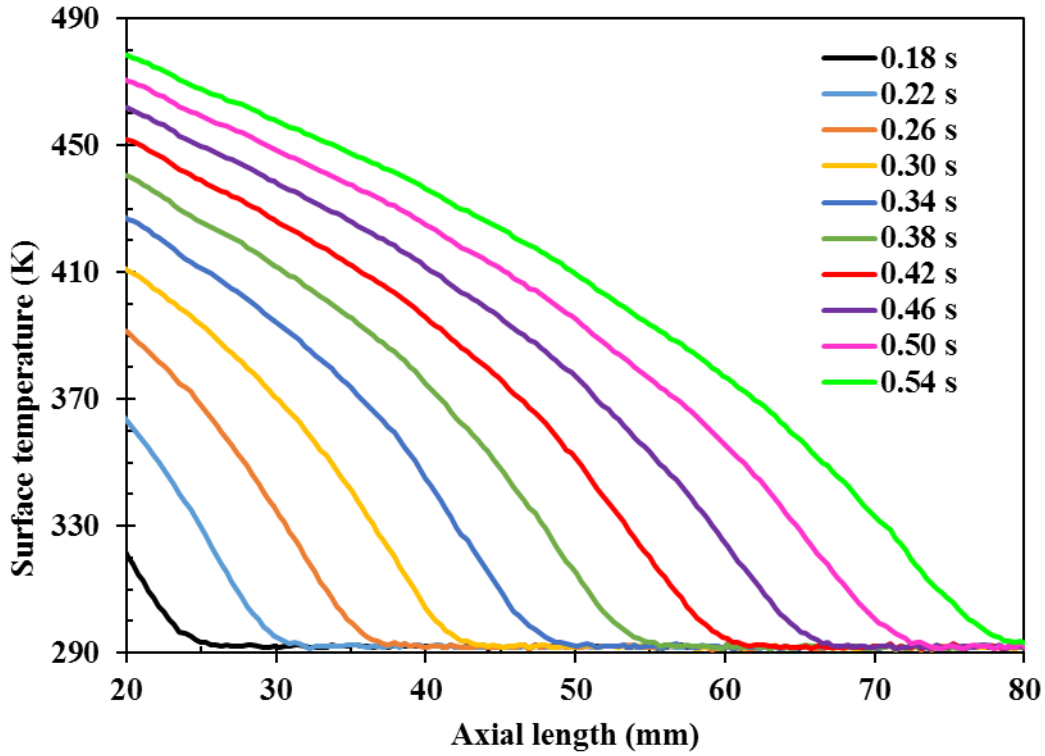

(b)

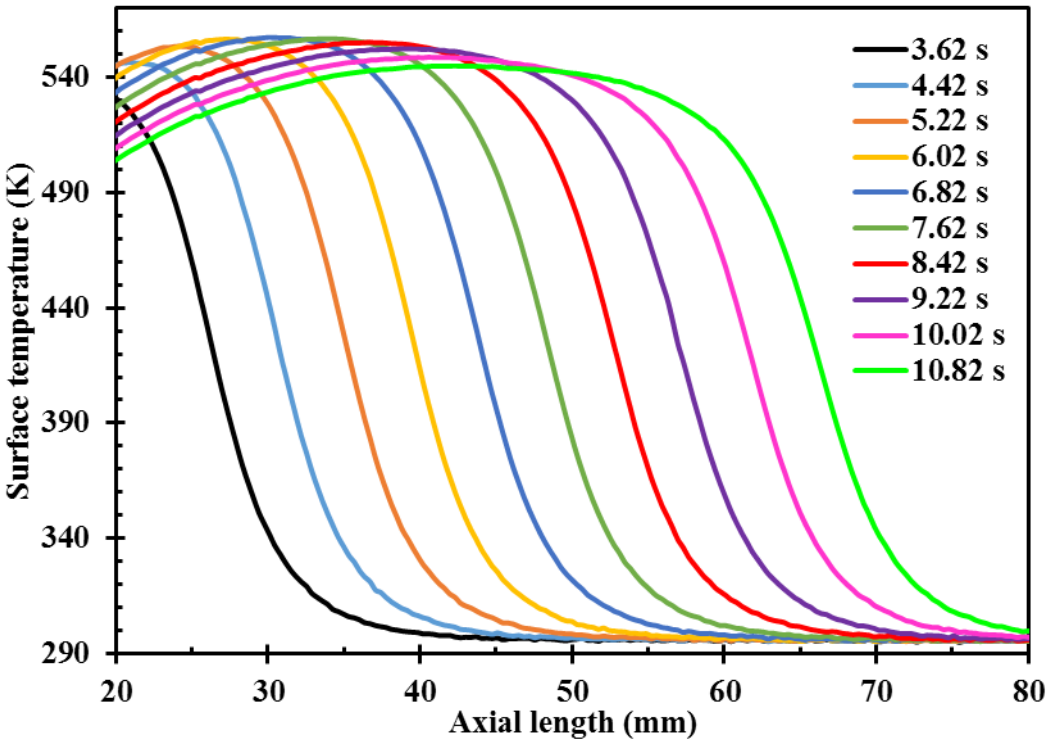

Figure 5-9: Temperature profiles over the length of the element for (a) the fast-burning Si + Pb_3O_4 and (b) the slow-burning Mn + Sb_2O_3 compositions taken over the centre of the element. Both compositions contained 36 wt.% fuel.

5.3 NUMERICAL SIMULATIONS

A numerical model of the complete delay element structure was created according to the details provided in Section 4. The outside surface temperature was fit through a least-squares method to the IR camera measurements taken for both the slow-burning Mn + Sb_2O_3 and the fast burning Si + Pb_3O_4 reactions. Since the slow-burning Mn + Sb_2O_3 composition resulted in fully developed temperature profiles, it was used to develop the model, which was then also applied to the fast-burning Si + Pb_3O_4 reaction. The progression of the reaction modelled and measured using the IR camera for Mn + Sb_2O_3 and Si + Pb_3O_4 is shown in **Figure 5-10** and **Figure 5-11** respectively.

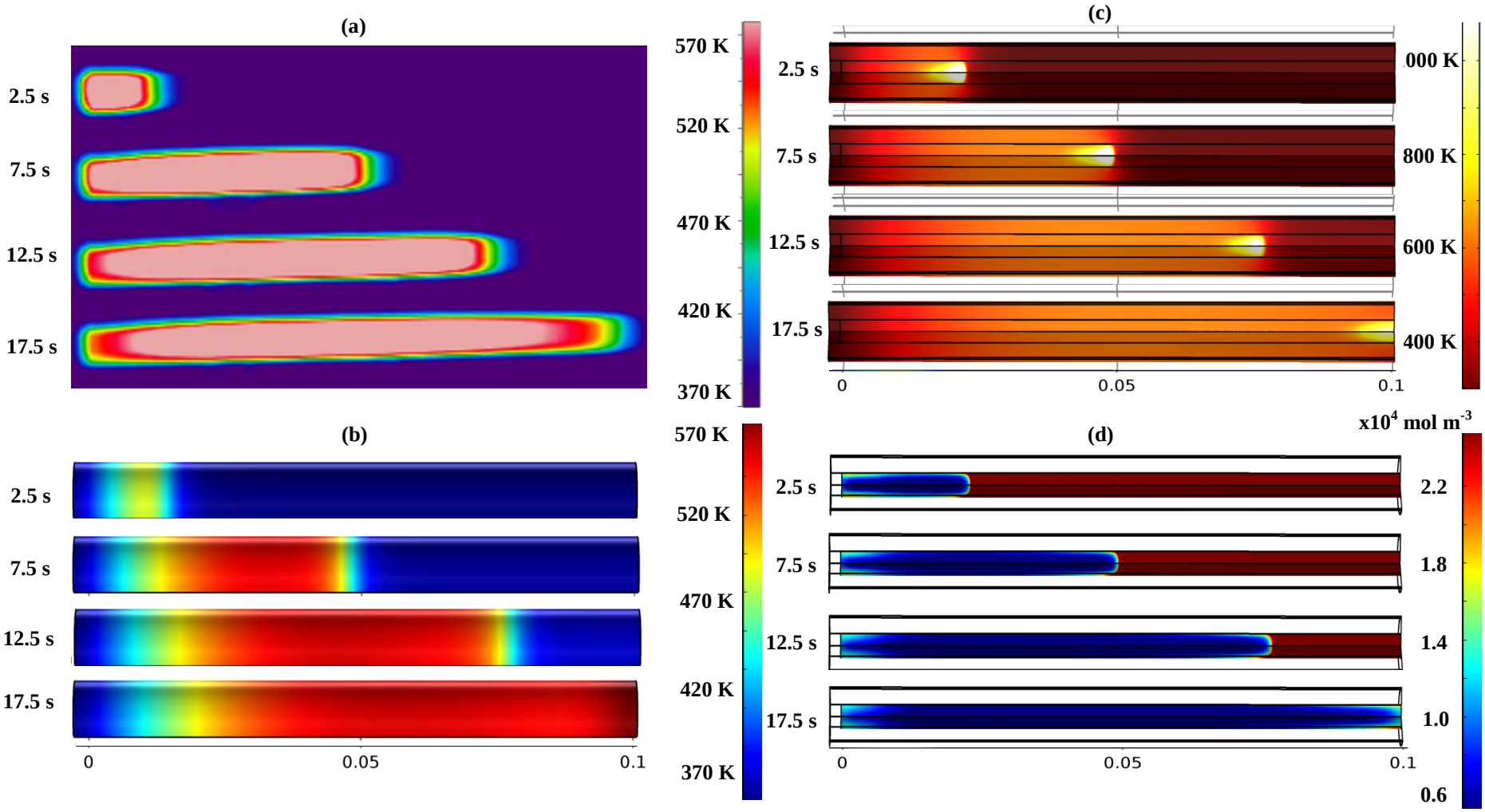

Figure 5-10: The progression of the reaction in the delay element containing Mn + Sb_2O_3 obtained from (a) the outside surface temperature measured with the IR camera, (b) the surface temperature modelled, (c) internal temperatures modelled and (d) the concentration profiles (C_{Mn}) modelled

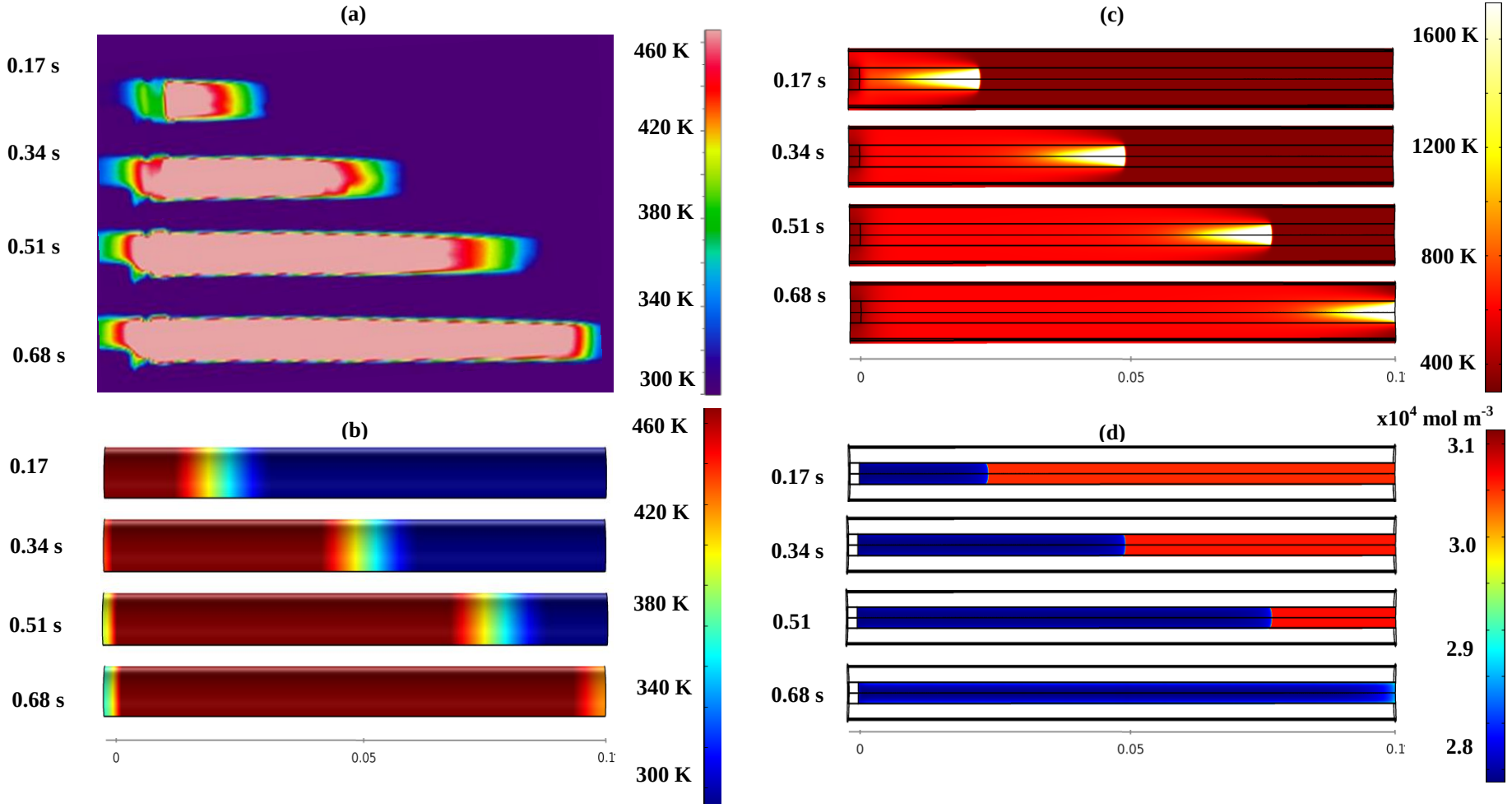

Figure 5-11: Progression of the reaction in the delay element containing Si + Pb_3O_4 obtained from (a) the outside surface temperature measured with the IR camera, (b) the surface temperature modelled, (c) internal temperatures modelled and (d) concentration profiles (C_{Si}) modelled

The temperature profiles on the outside surface of the elements was fit through a least-squares method (as described in Chapter 4) to obtain the kinetic parameters. The temperature profiles measured using the IR camera and modelled for both compositions with the best fit kinetics are shown in **Figure 5-12**. The best fit kinetic parameters for both compositions are given in **Table 5-1**.

Table 5-1: Best fit kinetic parameters obtained for the numerical model

Composition	**Fuel content**	E_a **(kJ/mol)**	k_0	n	m
Mn + Sb_2O_3	36 wt.%	30	2.75×10^{-28} $m^{24}mol^{-9}s^{-1}$	8	1
Si + Pb_3O_4	36 wt.%	30	5.6×10^{-31} $m^{33}mol^{-11}s^{-1}$	9	3

Good agreement was obtained between the numerical model and the IR camera data. The reaction kinetics obtained from the empirical fit is exceptionally high. This suggests that the constants have no physical basis and is purely an empirical equation. In both cases, however, the measured profiles converge to a higher peak temperature than the numerically modelled profiles. One reason could be due to the assumptions made about the oxidant thermal conductivity. A sensitivity analysis was therefore performed on the physical properties of the compositions to aid in understanding the extent to which these properties influence the numerical model. In order to evaluate the sensitivity of the models to the different parameters, the burn rates were evaluated for either increasing or decreasing property values depending on the feasibility of the parameter value changes.

In **Figure 5-13** it is shown that the thermal conductivity has a very small effect on the numerical model. The thermal conductivity is therefore not the reason for the discrepancies in the peak temperature observed. It was also found that when the thermal conductivity was increased by more than 20%, the reaction died out before it reached the end of the element. The heat of reaction was found to have the most significant effect on the burn rate. The density and heat capacity only appear in the model as a composite parameter. An increase in either parameter leads to a decrease in the overall burn rate. In the case of density and heat capacity, a property increase of more than 15% causes the reaction to extinguish similar to the extinguishing that occurs for the increased thermal conductivity. Another cause of the peak temperature discrepancy could be the heat transfer parameters. In order to evaluate this, the sensitivity of the Si + Pb_3O_4 model to changes in the heat transfer parameters of

convection, radiation and porous media conduction was analysed. The results of this sensitivity analysis are shown in **Figure 5-14**.

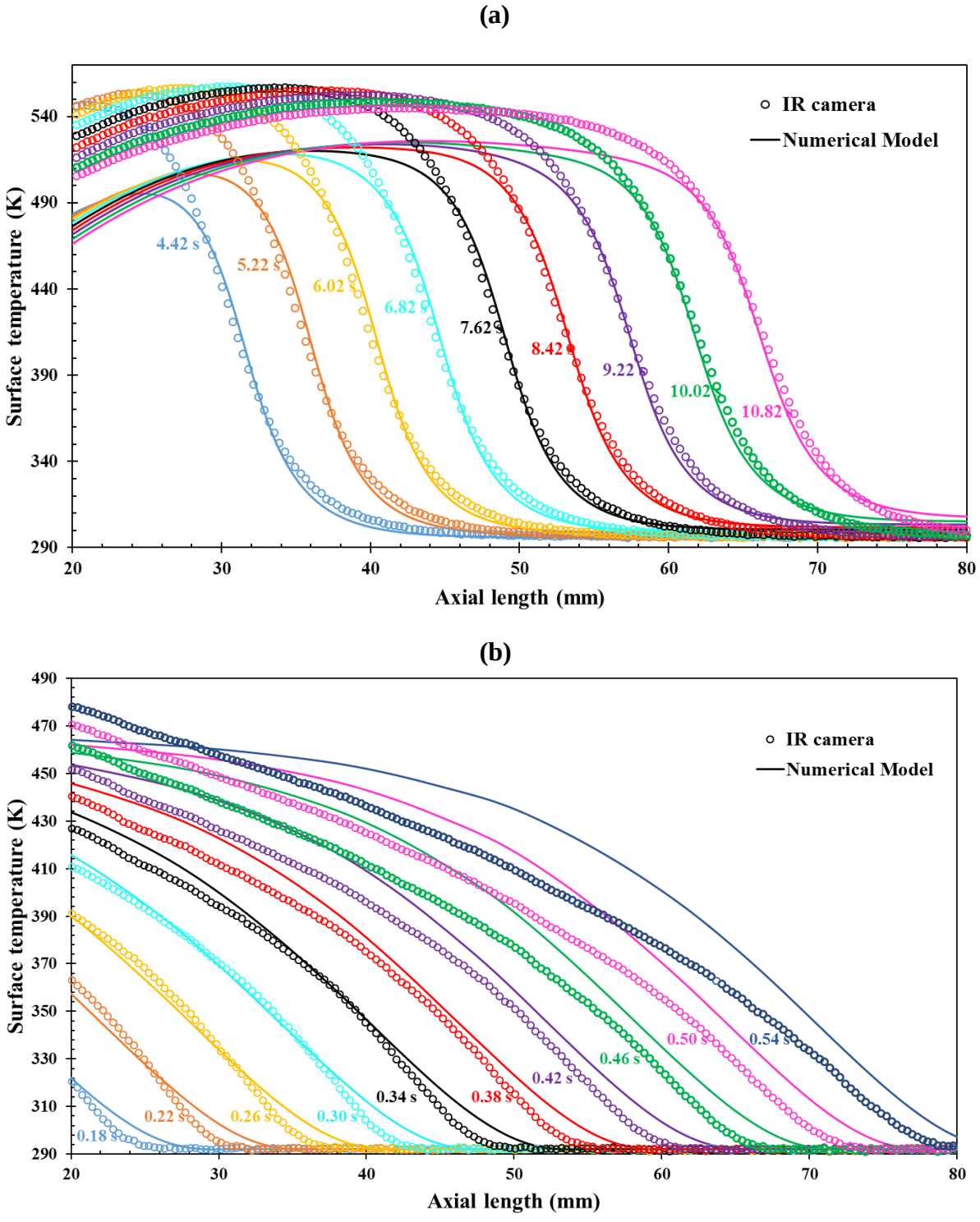

Figure 5-12: Temperature profiles on the outside of the element as developed over the length of the element obtained from the IR camera and the numerical model for (a) Mn + Sb_2O_3 and (b) Si + Pb_3O_4

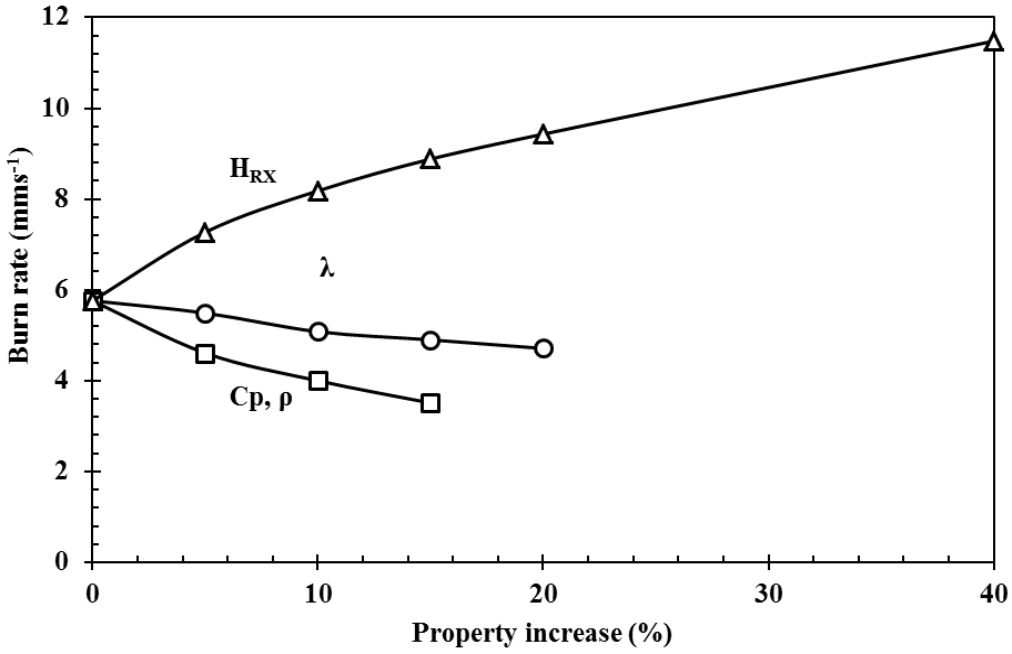

Figure 5-13: Sensitivity of the numerical model to the physical properties of the composition evaluated for the Mn + Sb_2O_3 composition

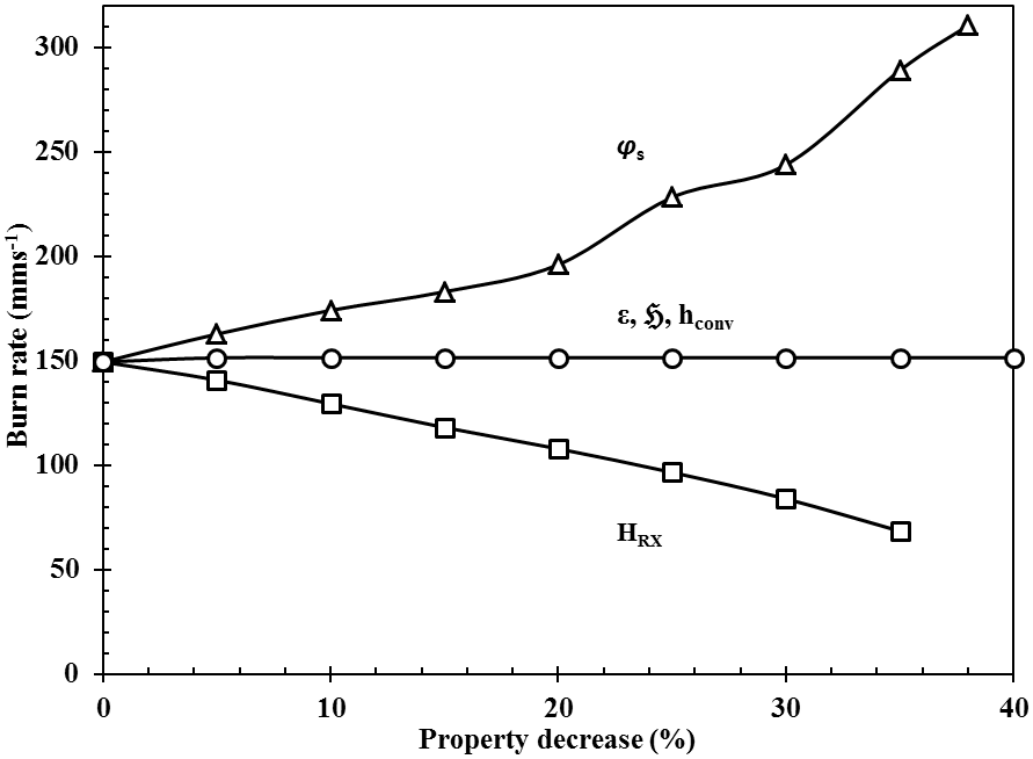

Figure 5-14: Sensitivity analysis of the Si + Pb_3O_4 model to changes in the heat transfer parameters

From **Figure 5-14** it was found that the external heat transfer parameters (ε, $\mathfrak{H}$ and h_{conv}) had a negligible effect on the burn rate. This was probably due to the reaction occurring at a much faster rate than the rate at which heat transfer occurs. The heat transfer only affects the composition after the reaction has already completed. Similar to the results for Mn + Sb_2O_3 in **Figure 5-13**, the heat of reaction has a significant impact on the burn rate. Decreasing the heat of reaction by more than 35% further leads to the reaction stopping before it reaches the end of the element. The volume fraction solids in the porous composition also had a big impact on the burn rate. The sensitivity of both models to the parameters shown in **Figure 5-13** and **Figure 5-14** was found to indicate the same trend. The significant effect of these two parameters (H_{rx} and φ_s) is due to the delay composition being modelled as a porous medium through which the heat has to be conducted in order for the reaction to propagate forward. These two parameters directly influence the amount of heat generated in the reaction zone and therefore the rate at which the heat is transferred axially through the composition. Due to the composition being modelled as a porous medium, the intensity of the heat generated at a specific point is a rate-controlling factor. The analytical model of Khaikin and Merzhanov (1966) in Equation 2-5 represent the heat of reaction to be inversely proportional to the burn rate. This contradicts current findings. Another notable finding is that the numerical model predicted that the volume fraction solids (or packing density) have a significant influence on the burn rate. The packing density is, however, not a parameter in any of the analytical models presented.

The predictions of the numerical model were validated by comparing the effect of ambient temperature on the burn rate with the experimental results obtained in the literature. The result of the validation is shown in **Figure 5-15**. The average burn rate was predicted by the numerical model to increase by 9.40% for a 50 °C increase in the ambient temperature. This corresponds well to experimental and numerical findings of 8.52% and 9.65% increase per 50 °C obtained respectively by Jakubko (1997) experimentally and Boddington et al. (1989) numerically. Li et al. (2010), however, obtained inconsistent results with the increase in burn rate, which varied between a 3.05% and an 8.24% increase for a 50 °C increase in ambient temperature over a range of fuel-lean compositions containing B + Pb_3O_4. Their slopes of burn rate over ambient temperature increased for increasing fuel content. One factor that could have influenced their results is the filling process. The compositions were all filled to a constant weight at a constant pressure, but the compositions varied between 1 wt.% and 16 wt.% fuel.

The change in composition could significantly change the density of the composition, and when pressing the same mass at the same pressure, could result in different packing densities.

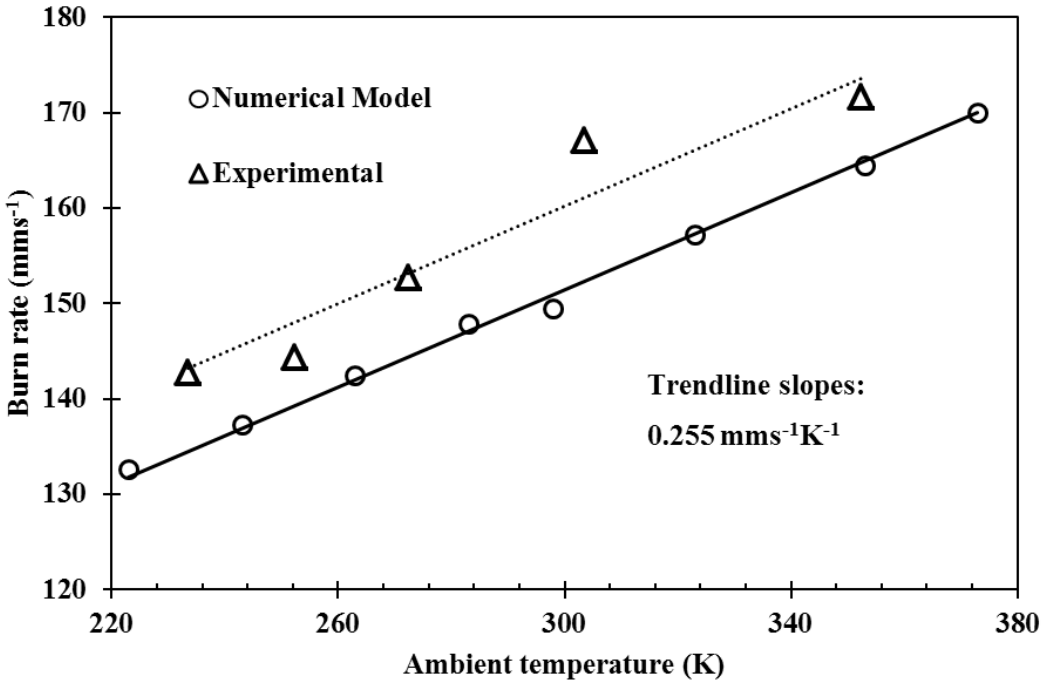

Figure 5-15: Change in burn rate due to changes in the ambient temperature as modelled and obtained experimentally by Jakubko (1997) for the Si + Pb_3O_4 system containing 36 wt.%

The effect of changes in the tube wall geometry on the burn rate was investigated for aluminium and lead tube delay elements. **Figure 5-16** shows the results from this analysis. The data were predicted numerically for lead tubes with a constant inside diameter of 2.625 mm and varying outside diameter, for lead tubes with a constant outside diameter of 6.00 mm with varying inside diameters, and lastly for aluminium tubes with a constant wall thickness of 2 mm and varying outside diameters. All of these simulations were performed for the Si + Pb_3O_4 composition at 36 wt.% Si. This was also compared to the experimental data obtained by Kalombo et al. (2007) for aluminium tube elements containing Si + Bi_2O_3 by maintaining a constant outside diameter of 6.200 mm with varying inside diameters.

It was found that the burn rate increased with increases in both the internal and external diameters. This agrees with the experimental results of Kalombo et al. (2007). These observations can be rationalised as follows: increasing the core diameter leads to a greater mass of reactive powder per unit length and a lower specific surface area, while increasing the outer diameter reduces lateral heat loss.

Boddington et al. (1989) and Boddington et al. (1986) tested burn rates in square channels with different cross-sectional areas and also found faster burn rates for larger column areas. They concluded that the cross-sectional area of the reacting composition is the most important factor determining lateral heat loss. From **Figure 5-16** it was confirmed that the cross-sectional area of the reacting core has a significant impact on the burn rate, but that the outside diameter itself also significantly influences the burn rate.

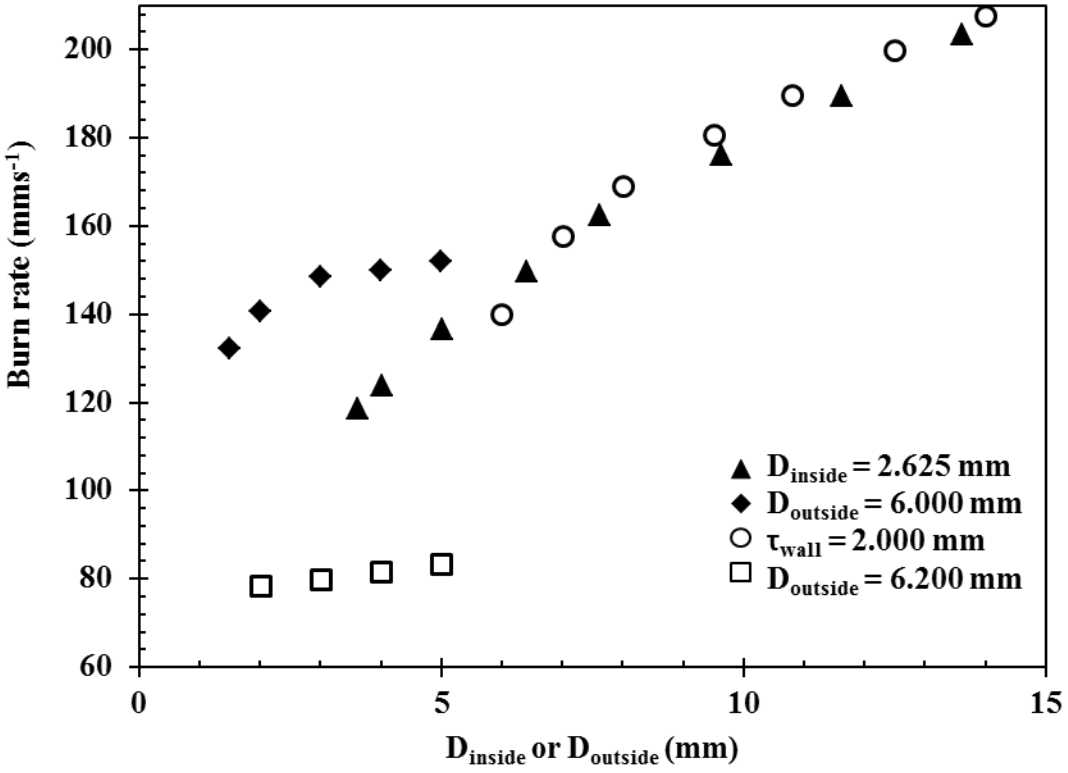

Figure 5-16: Effect of wall thickness and core diameter on the burn rate as predicted by the numerical model for Si + Pb_3O_4. Open symbols (○, □) indicate aluminium tubes and closed symbols (▲, ◆) indicate lead tubes. The data for aluminium tubes with an outside diameter of 6.2 mm is experimental for elements containing Si + Bi_2O_3 (Kalombo et al., 2007).

The effect of the nature of the tube material on the burn rate was also investigated. Delay elements with inner and outer diameters of 2.625 mm and 6.400 mm were simulated with different tube materials and containing 36 wt.% Si with Pb_3O_4. The thermal resistance of the tube is influenced by the volumetric heat capacity of the tube material as well as the thermal conductivity, and both of these parameters are therefore expected to influence the burn rate. Different combinations of volumetric heat capacity and thermal conductivity corresponding to real materials were modelled.

The response surface of these parameters on the burn rate is shown in **Figure 5-17**, which indicates that an increase in burn rate can be expected for tube materials with higher thermal conductivities and lower volumetric heat capacities. For very high thermal conductivity materials, the effect of both parameters is significant, but the volumetric heat capacity has a lesser effect for materials with low thermal conductivity. Experimental results comparing lead elements and aluminium elements indicated only a slightly lower burn rate for lead tubes. This is consistent with the findings presented in **Figure 5-17**. There are unfortunately very few experimental studies that address this effect. One study by Kalombo et al. (2007) observed significantly faster burn rates in lead tubes in comparison to those in aluminium tubes. However, the study had to use different preparation methods for the lead and aluminium tubes. This would result in different packing densities, which in turn would influence the burn rates. This highlights the difficulties in controlling all parameters independently when attempting comparative studies experimentally, and emphasises the need for applicable modelling solutions.

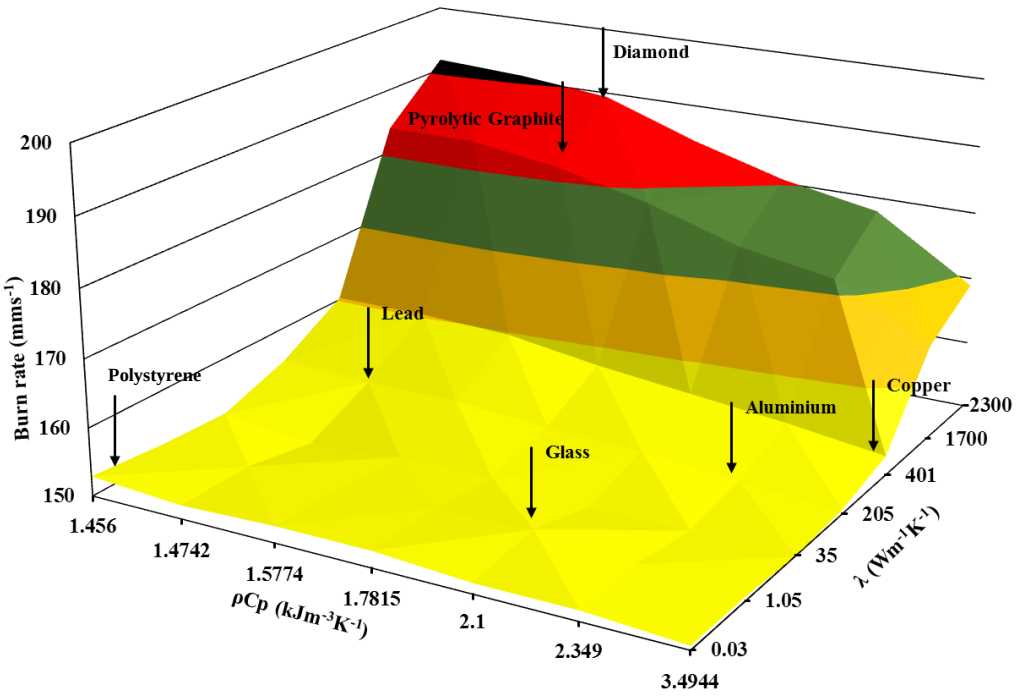

Figure 5-17: Response surface for the influence of thermal conductivity and volumetric heat capacity on the burn rate modelled using real material properties for elements containing 36 wt.% Si + Pb_3O_4

The shape of the combustion front was found to be influenced by several factors, including the activation energy of the reaction, the packing density of the composition and the tube wall material properties. **Figure 5-18** shows the combustion wave front in the element for different real tube materials. The isotherms are also shown in **Figure 5-18**, which in most cases have a teardrop shape. The combustion proceeds from left to right, with the blunt portion facing the front of the wave followed by a thinning tail to form the teardrop.

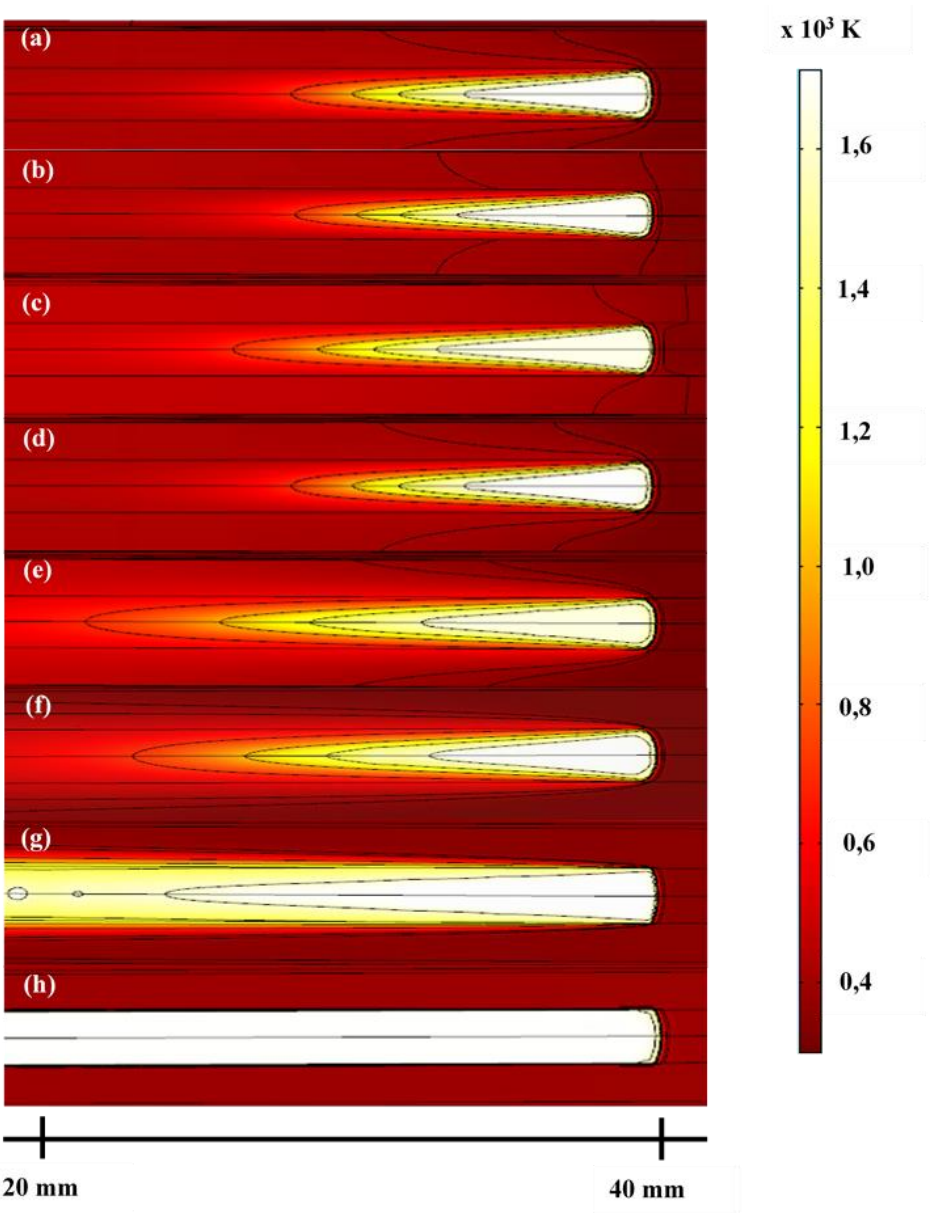

Figure 5-18: Combustion wave propagation of the Si + Pb_3O_4 composition in tube materials consisting of (a) aluminium, (b) diamond, (c) pyrolytic graphite, (d) copper, (e) lead, (f) stainless steel, (g) glass and (h) polystyrene

The thinning of the tail end of the teardrop is a result of radial heat loss, and is elongated for higher radial heat losses. The tube with the lowest heat transfer properties is the polystyrene tube, which shows almost no radial heat losses and no teardrop shaped tail.

The temperature rise in the walls lags behind the temperature rise in the unburned composition. The only material which showed an exception to this was the pyrolytic graphite casing. In this case the isothermal contours of the reaction propagation indicate that heat is more rapidly transferred forward in the axial direction along the tube wall. This leads to a preheating effect of the unburned composition, which could cause the reaction front to propagate faster. The other materials with high thermal conductivity (diamond, copper and aluminium) did not display the same pre-heating effect, even though the diamond tube has a higher thermal conductivity than the pyrolytic graphite. This mechanism is determined by a combination of both the thermal conductivity of the material and the volumetric heat capacity. The pyrolytic graphite, in addition to high thermal conductivity, had the lowest volumetric heat capacity of the materials with high thermal conductivities. Diamond has a somewhat higher thermal conductivity, and the isothermal contours for this casing did show slight preheating ahead of the combustion front.

Radial combustion occurs when the tube wall on the internal surface exceeds the ignition temperature of the composition due to lateral heat transfer. The composition on the outer edge of the core thereby ignites before the combustion wave front reaches that point. The mechanisms of preheating and radial combustion were studied by Norgrove et al. (1994) on a numerical basis. The tube materials used in their simulations were assumed to be perfect heat conductors. They found that for compositions containing $KMnO_4$ as the oxidant, preheating and radial combustion were unavoidable. This is most likely due to the decomposition temperature of the oxidant, which for $KMnO_4$ is as low as 506 K. The study was also expanded by Clements et al. (1995), in which they assigned finite conductivity to the tube walls and still came to the same conclusion. In the current numerical model, the preheating that was observed did not lead to any radial combustion in any of the investigated scenarios. This can be attributed to the thermal stability of Pb_3O_4, which is much higher than that of $KMnO_4$, as it only decomposes above 873 K. Therefore the inside wall temperature would have to be maintained above 873 K ahead of the combustion wave. This temperature would also likely have to be sustained for some time in order for ignition and radial combustion to occur on the outside edge of the reactive column.

Radial combustion would therefore be controlled by the material properties of the tube wall, the composition porosity, the activation energy of the reaction, the decomposition temperature of the oxidant and the burn rate of the reaction.

Instantaneous velocity profiles over the length of the delay element can give an indication of the effect of the end points of the element, as well as the consistency of the burn rate. The instantaneous velocity profiles for a lead delay element containing Si + Pb_3O_4 as obtained from the numerical model and measured using the IR camera are shown in **Figure 5-19**. The results of both methods indicate that directly following ignition, the reaction was fast but then slowed down. For both the numerical model and the IR camera methods, it takes about 18 mm for the combustion to propagate at a steady rate. Norgrove et al. (1994) and Clements et al. (1995) found that the steady propagation rate is reached at about 12.5 mm after ignition. However, the burn rate calculated prior to the steady propagation was slower than the average burn rate. The reason for this difference most likely lies in the numerical initiation of the reaction. In this study, as well as in the studies by Norgrove et al. (1994) and Clements et al. (1995), a form of numerical initiation was required to start the convergence of the solutions.

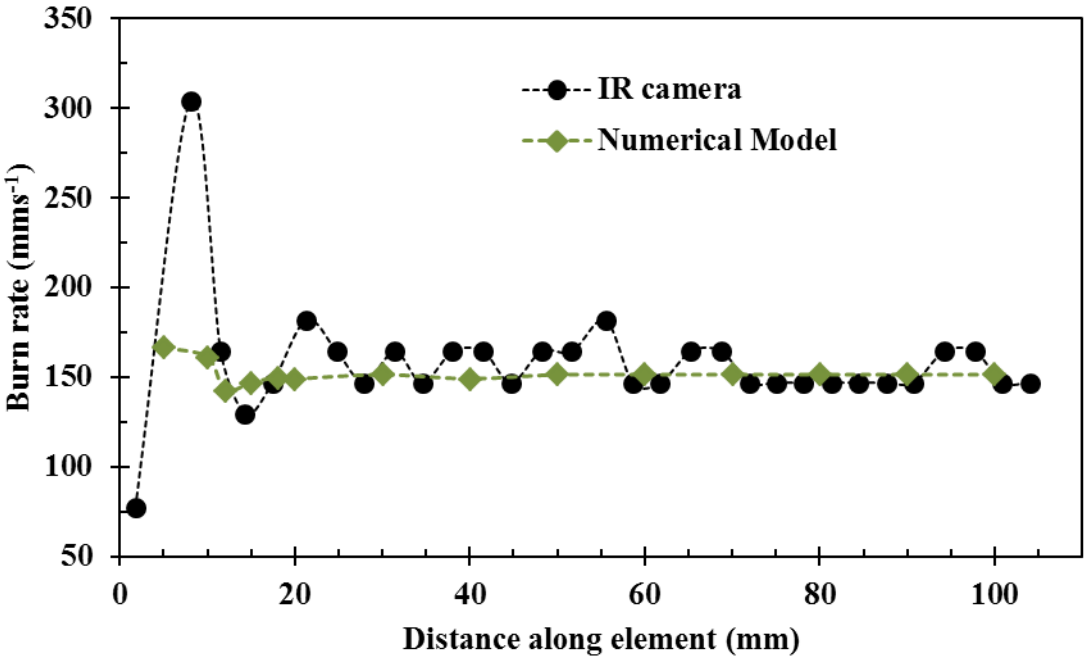

Figure 5-19: Instantaneous velocity profiles for a lead-drawn delay element containing 36 wt.% Si + Pb_3O_4 measured using the IR camera and calculated with the numerical model

The last investigation in this study was performed to determine the radial temperature profiles and the spread of the heat across a slice of the element. The distribution of the temperature over the radial section of the element is shown in **Figure 5-20**. The radial temperature distribution indicates that the paint layer on the outside surface did have a small effect on the element. The temperature drop over the paint layer was about 25 K. It was also found that the temperature drop over the lead wall was very small, which was likely due to the high thermal conductivity of the lead wall. It is further expected from **Figure 5-18** that the slope of the profile over the composition will decrease for tube wall materials with low thermal conductivities such as polystyrene and glass.

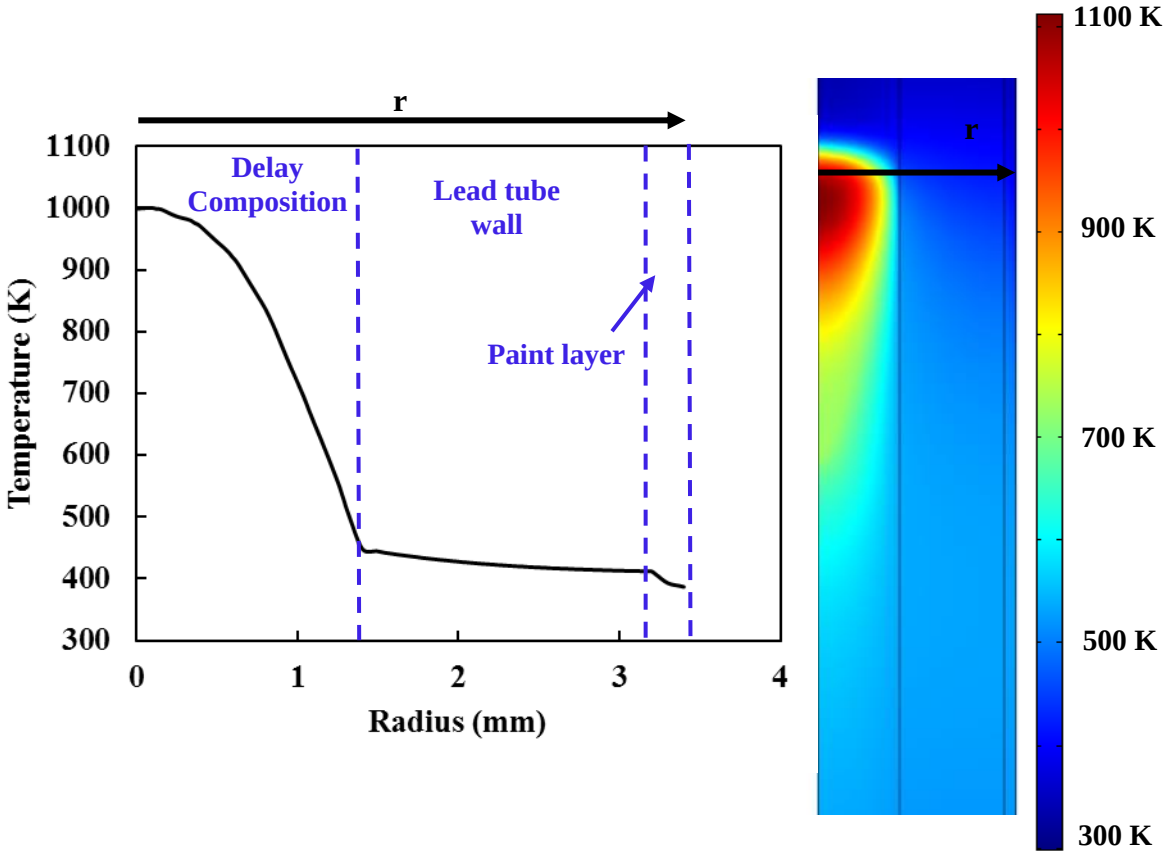

Figure 5-20: Temperature profile across a section of the delay element containing 36 wt.% Mn + Sb_2O_3 to indicate the effect of the heat transfer resistance layers

6 CONCLUSIONS AND RECOMMENDATIONS

Three problems were identified as factors inhibiting the improvement in the burn rate reliability of pyrotechnic time delay elements. These three problems were set as the objectives of this study. The need for a safe and accurate burn rate measurement technique was first identified. The use of an IR camera was identified as a possible method for accurately and safely measuring the burn rates. The IR camera method was developed and tested in comparison to two other commonly used techniques, the industrial detonator test and the laboratory scale thermocouple test. The comparison of the burn rates measured indicated that the burn rates measured using the IR camera technique were closer to those of the industrial detonator test than those of the thermocouple technique. The standard deviations of the burn rates measured using the IR camera were of the same order of size as the industrial detonator measurements. The laboratory thermocouple technique had very large standard deviations, and the size and response rate of the thermocouples were identified as the problem. The IR camera measurements were slightly lower than the measurements of the industrial detonator test, which is most likely due to the differing assembly components of the two techniques. The IR camera method was found to be safe, accurate, required minimal alterations to the delay elements and was non-destructive by nature. The IR camera technique was therefore found to be a viable method of measuring the burn rates of pyrotechnic delay elements.

The second problem identified was the need for a numerical model to predict delay element behaviours. A numerical model was created which includes the delay element structure as well as the pyrotechnic reaction of the delay composition inside. The IR camera provided temperature profiles along with the average burn rates. These temperature profiles were used to calibrate the numerical model. The slow-burning Mn + Sb_2O_3 composition was found to exhibit fully developed temperature profiles, whereas the fast-burning Si + Pb_3O_4 composition had temperature profiles that were not yet fully developed. The slow-burning composition was therefore used to develop the numerical model, followed by application to the fast-burning composition. The numerical model was successfully developed and the kinetic parameters were fit against the IR camera measurements. The numerical model was then used to partially fulfil the third objective of the study.

The third and last problem identified was the lack in data in the open literature on the effect of external and internal factors on the burn rate. This is due to the problems experienced in keeping all the factors constant while varying only one in experimental preparation and testing. The numerical model was therefore a perfect tool for evaluating the effect of these factors on the burn rate. The model was validated by comparison to the experimental data from Jakubko (1997) quantifying the effect of the ambient temperature on the average burn rate. The results from both were in good agreement with the experimental data, indicating a change in burn rate of 9,40% and 8.52% per 50 °C change in ambient temperature. The numerical results obtained were also in good agreement with the numerical predictions made by Boddington et al. (1989), which predicted a 9.65% change in burn rate for a 50 °C change in ambient temperature.

The numerical model was then used to evaluate the effect of other parameters on the burn rate. The parameters investigated were geometry, composition properties, tube material and other heat transfer parameters. The external heat transfer parameters of all the heat transfer mechanisms present were found not to have any significant effect on the burn rate. The volume fraction solids and heat of reaction were found to have the biggest influence on the burn rate. Considering the geometry, the cross-sectional area of the reacting core and the outside diameter of the tube itself had a large impact on the burn rates. The nature of the tube material was also investigated, and it was revealed that the burn rate is higher for materials with high thermal conductivities and low volumetric heat capacities. This effect was, however, only significant for materials with very low volumetric heat capacities. The data from the literature on this effect is unfortunately very inconsistent. This highlights the problems encountered in experimentally keeping all the parameters constant except one. The paint layer applied to the outside of the element for the IR camera method was found to have a small influence on the temperature profiles, but did not have any significant effect on the average burn rate. There was one factor that could not be evaluated numerically, which was the effect of the particle packing. This was evaluated experimentally by varying both the fuel and the oxidant particle sizes simultaneously. SEM analysis indicated that the fuel particles are encased in a sea of oxidant particles, and that no real packing arrangement was present.

During this evaluation, Ekvi thermodynamic simulations also revealed that the Mn + Sb_2O_3 composition undergoes a secondary intermetallic reaction to form alloys of Mn + Sb. This was confirmed through XRD analysis of the product residues. This has the advantage of adding additional exothermic reaction heat to the composition even in fuel-lean compositions. This leads to constant burn rates over a wider range of fuel contents.

The numerical model was successfully created and was found to be an invaluable tool in clarifying the factors affecting the burn rates of pyrotechnic time delay elements. The use of the model would reduce the need for extensive experimental testing, which would not only save costs and time, but also reduce the exposure of personnel to possibly dangerous test setups.

It is recommended that further studies should be done to investigate situations that lead to the propagation reaction dying before reaching the end of the element. The use of different kinetic models should also be investigated to determine whether there is a better kinetic model to describe the reaction behaviour of time delay compositions.

REFERENCES

AHMAD, S. R. & RUSSEL, D. A. 2005. Laser ignition of pyrotechnics - Effects of wavelength, composition and confinement. *Propellants, Explosives, Pyrotechnics,* 30(2)**,** 131-139.

AHMAD, S. R. & RUSSEL, D. A. 2008. Studies into laser ignition of confined pyrotechnics. *Propellants, Explosives, Pyrotechnics,* 33**,** 396-402.

AL-KAZRAJI, S. S. & REES, G. J. 1978. The fast pyrotechnic reaction of silicon and red lead part 1. Differential thermal analysis studies. *Combustion and Flame,* 31**,** 105-113.

AL-KAZRAJI, S. S. & REES, G. J. 1979. The fast pyrotechnic reaction of silicon and red lead: heats of reaction and rates of burning. *FUEL,* 58**,** 139-143.

ALDUSHIN, A. P. & KHAIKIN, B. I. 1974. Combustion of mixtures forming condensed reaction products. *Fizika Goreniya i Vzryva,* 10(3)**,** 313-323.

ALDUSHIN, A. P., VOL'PERT, V. A. & FILIPENKO, V. P. 1987. Effect of reagent melting on combustion stability for gasless systems. *Combustion, Explosion, and Shock Waves,* 23(4)**,** 408-420.

AMERICAN SOCIETY OF HEATING, REFRIGERATING AND AIR-CONDITIONING ENGINEERS, 1997. *1997 ASHRAE handbook: Fundamentals.* USA, GA, Atlanta: ASHREA, 3.11-3.12.

ANISIMOVA, N. I., BORDOVSKY, G. A., BORDOVSKY, V. A. & SELDAYEV, V. I. 'Electrical and thermal properties of Bi_2O_3, PbO and mixed oxides of Bi_2O_3-PbO system', *In:* IEEE International Conference on Solid Dielectrics Vol 1. France, Toulouse: IEEE, 141-142.

ARMSTRONG, R. 1990. Models for gasless combustion in layered materials and random media. *Combustion Science and Technology,* 71(4-6)**,** 155-174.

BECK, M. W. & BROWN, M. E. 1983. Thermal analysis of antimony/potassium permanganate pyrotechnic compositions. *Thermochimica Acta,* 65(2-3)**,** 197-212.

BECK, M. W. & BROWN, M. E. 1986. Burning of antimony/potassium permanganate pyrotechnic compositions in closed systems. *Combustion and Flame,* 65**,** 263-271.

BECK, M. W., BROWN, M. E. & CAWTHORNE, D. 1984. Pyrotechnic delay compositions. *ChemSA,* June 1984**,** 398-399,401.

BECK, M. W. & FLANAGAN, J. 1992. *Delay composition and device*. USA, US5147476A.

BERGER, B. 2005. Parameters influencing the pyrotechnic reaction. *Propellants, Explosives, Pyrotechnics,* 30(1)**,** 27-35.

BOCKMON, B. S., PANTOYA, M. L., SON, S. F., ASAY, B. W. & MANG, J. T. 2005. Combustion velocities and propagation mechanisms of metastable interstitial composites. *Journal of Applied Physics,* 98 (6), art. no. 064903.

BODDINGTON, T., COTTRELL, A. & LAYE, P. G. 1989. A numerical model of combustion in gasless pyrotechnic systems. *Combustion and Flame,* 76**,** 63-69.

BODDINGTON, T., COTTRELL, A. & LAYE, P. G. 1990. Combustion transfer in gasless pyrotechnics. *Combustion and Flame,* 79**,** 234-241.

BODDINGTON, T., LAYE, P. G., PUDE, J. R. G. & TIPPING, J. 1982. Temperature profile analysis of pyrotechnic systems. *Combustion and Flame,* 47**,** 235-254.

BODDINGTON, T., LAYE, P. G., TIPPING, J. & WHALLEY, D. 1986. Kinetic analysis of temperature profiles of pyrotechnic systems. *Combustion and Flame,* 63**,** 359-368.

BRENT, G. F. & HARDING, M. D. 1993. *Shock tube initiator*. United States, US5351618.

BROWN, M. E. 1997. Steps in a minefield: Some kinetic aspects of thermal analysis. *Journal of Thermal Analysis,* 49**,** 17-32.

BROWN, M. E., TAYLOR, S. J. & TRIBELHORN, M. J. 1998. Fuel-oxidant particle contact in binary pyrotechnic reactions. *Propellants, Explosives, Pyrotechnics,* 23**,** 320-327.

CARLOMAGNO, G. M. & CARDONE, G. 2010. Infrared thermography for convective heat transfer measurements. *Experiments in Fluids,* 49(6)**,** 1187-1218.

CENGEL, Y. A. 2006. *Heat and mass transfer: A practical approach.* USA, New York: The McGraw-Hill Companies, 866.

CENTERS, P. W. 1988. Sublimation-controlled oxidation of antimony trioxide. *Journal of Solid State Chemistry,* 72(2)**,** 303-308.

CHARSLEY, E. L., FORD, M. C., TOLHURST, D. E., BAIRD-PARKER, S., BODDINGTON, T. & LAYE, P. G. 1978. Differential thermal analysis and temperature profile analysis of pyrotechnic delay systems: Mixtures of tungsten and potassium dichromate. *Thermochimica Acta,* 25**,** 131-141.

CHASE, M. W., CURNUTT, J. L., HU, A. T., PROPHET, H., SYVERUD, A. N. & WALKER, L. C. 1974. JANAF Thermochemical tables, 1974 supplement. *Journal of Physical and Chemical Reference Data,* 3(2)**,** 470.

CLEMENTS, L., KING-HELE, J. A., JONES, A. F. & THOMAS, R. M. 1995. Some effects of axial temperature gradients in the wall of a detonator delay element. *Combustion Science and Technology,* 107(4-6)**,** 205-221.

COMSOL 2013. *COMSOL Multiphysics 4.3b*, COMSOL, 3 May 2013.

DANALI, S. M., PALAIAH, R. S. & RAHA, K. C. 2010. Developments in pyrotechnics. *Defence Science Journal*, 60(2)**,** 152-158.

DEAN, J. A. 1999. *Lange's handbook of chemistry*. USA, New York: The McGraw-Hill Companies, 6.131-6.137.

DESAI, P. D. 1986. Thermodynamic properties of iron and silicon. *Journal of Physical and Chemical Reference Data,* 15(3)**,** 967-983.

DIAS INFRARED SYSTEMS 2010. *"Pyroview Uncooled IR Camera: Operating instructions".*

DRENNAN, R. L. & BROWN, M. E. 1992a. Binary and ternary pyrotechnic systems of Mn and/or Mo and BaO_2 and/or SrO_2 Part 1. Thermal analysis. *Thermochimica Acta,* 208**,** 201-221.

DRENNAN, R. L. & BROWN, M. E. 1992b. Binary and ternary pyrotechnic systems of Mn and/or Mo and BaO_2 and/or SrO_2 Part 2. Combustion studies. *Thermochimica Acta,* 208**,** 223-246.

DRENNAN, R. L. & BROWN, M. E. 1992c. Binary and ternary pyrotechnic systems of Mn and/or Mo and BaO_2 and/or SrO_2 Part 3. Kinetic aspects. *Thermochimica Acta,* 208**,** 247-259.

DUGAM, A. G., MUTTALIB, A., GANDHI, H. J., PHAWADE, P. A., JOHN, A. & KHARE, R. R. 1999. Effect of fuel content and particle size distribution of oxidiser on ignition of metal-based pyrotechnic compositions. *Defence Science Journal,* 49(3)**,** 263-268.

DUNMEAD, S. D., READEY, D. W., SEMIER, C. E. & HOLT, J. B. 1989. Kinetics of combustion synthesis in the Ti-C and Ti-C-Ni systems. *Journal of the American Ceramic Society,* 72(12)**,** 2318-2324.

ELISCHER, P. P., CLEAL, G. & WILSON, M. 1986. The development of a boron and iron oxide delay system. *Report - Department of Defence, Materials Research Laboratories (Australia).*

GARNER, W. E. (ed.) 1955. *Chemistry of the solid state,* London, Butterworth: Academic Press.

GARNIER, P., BERAR, J. F. & CALVARIN, G. 1979. Calorimetric study of lead oxide Pb_3O_4 phase transition. *Material Research Bulletin,* 14**,** 1275-1279.

GOLUNSKI, S. E. & JACKSON, D. 1989. Antimony oxides: A guide to phase changes during catalyst preparation. *Applied Catalysis,* 48(11)**,** 123-135.

GRANIER, J. J. & PANTOYA, M. L. 2004. Laser ignition of nanocomposite thermites. *Combustion and Flame,* 138**,** 373-383.

GREEN, D. W. & PERRY, R. H. 2008. *Perry's Chemical Engineers' Handbook.* USA, New York: The McGraw-Hill Companies, 2.7 - 2.163.

HARDT, A. P. & PHUNG, P. V. 1973. Propagation of gasless reactions in solids-I. Analytical study of exothermic intermetallic reaction rates. *Combustion and Flame,* 21**,** 77-89.

HEDGER, J. T. 1983. Factors influencing the pyrotechnic reaction of silicon and red lead. *Propellants, Explosives, Pyrotechnics,* 8**,** 95-98.

HEISKELL, R. H. 1955. *Pyrotechnic composition*. USA, US2726943.

HEMMINGER, W. 1989. Thermal conductivity of lead in the range -180 to 500^{o}C. *International Journal of Thermophysics,* 10(4)**,** 765-777.

INTERNATIONAL ATOMIC ENERGY AGENCY 2008. Thermophysical properties of materials for nuclear engineering: A tutorial and collection of data. Vienna, Austria: IAEA.

IVLEVA, T. P., KRISHENIK, P. M. & SHKADINSKII, K. G. 1983. Nonidentity of steady conditions of combustion of gas-free mixed compositions. *Fizika Goreniya i Vzryva,* 19(4)**,** 87-90.

JAKUBKO, J. 1997. Pressure and temperature effects on burning rate of the silicon-red lead system. *Journal of Energetic Materials,* 15(2-3)**,** 151-161.

JAKUBKO, J. 1999. Combustion of the silicon-red lead system. Temperature of burning, kinetic analysis and mathematical model. *Combustion Science and Technology,* 146(1-6)**,** 37-55.

JAKUBKO, J. & CERNOSKOVA, E. 1997. Differential thermal analysis of the mixtures of silicon and red lead. *Journal of Thermal Analysis,* 50**,** 511-515.

KALOMBO, L., DEL FABBRO, O., CONRADIE, C. & FOCKE, W. W. 2007. Sb_6O_{13} and Bi_2O_3 as oxidants for Si in pyrotechnic time delay compositions. *Propellants, Explosives, Pyrotechnics,* 32(6)**,** 454-460.

KAPPAGANTULA, K. S., CLARK, B. & PANTOYA, M. L. 2011. Flame propagation experiments of non-gas-generating nanocomposite reactive materials. *Energy Fuels,* 25**,** 640-646.

KHAIKIN, B. I. & MERZHANOV, A. G. 1966. Theory of thermal propagation of a chemical reaction front. *Fizika Goreniya i Vzryva,* 2(3)**,** 36-46.

KHAWAM, A. & FLANAGAN, D. R. 2006. Solid-state kinetic models: Basics and mathematical fundamentals. *Journal of Physical Chemistry B,* 110**,** 17315-17328.

KNAPP, S., WEISER, V., KELZENBERG, S. & EISENREICH, N. 2014. Modeling ignition and thermal wave progression in binary granular pyrotechnic compositions. *Propellants, Explosives, Pyrotechnics,* 39**,** 423-433.

KOCH, E. & CLEMENT, D. 2007. Special materials in pyrotechnics: VI. Silicon - An old fuel with new perspectives. *Propellants, Explosives, Pyrotechnics,* 32(3)**,** 205-212.

KOSANKE, K., KOSANKE, B. J., VON MALTITZ, I., STURMAN, B., SHIMIZU, T., WILSON, M. A., KUBOTA, N. C., JENNINGS-WHITE, C. D. & CHAPMAN, D. 2004. *Pyrotechnic Chemistry, Pyrotechnic reference series No. 4.* USA: Journal of Pyrotechnics, Inc., 1-4.

LAYE, P. G. & CHARSLEY, E. L. 1987. Thermal analysis of pyrotechnics. *Thermochimica Acta,* 120**,** 325-349.

LI, Y., CHENG, Y., HUI, Y. & YAN, S. 2010. The effect of ambient temperature and boron content on the burning rate of the B/Pb_3O_4 delay compositions. *Journal of Energetic Materials,* 28**,** 77-84.

LUYBEN, W. L. 1989. *Process modeling, simulation and control for chemical engineers.* USA, New York: The McGraw-Hill Companies, 623.

MAGOMEDOV, Y. B. & GADJIEV, G. G. 2008. High-temperature thermal conductivity of silicon in the solid and liquid states. *High Temperature,* 46(3)**,** 422-424.

MIKLASZEWSKI, E. J., SHAW, A. P., PORET, J. C., SON, S. F. & GROVEN, L. J. 2014. Performance and aging of Mn/MnO_2 as an environmentally friendly energetic time delay composition. *ACS Sustainable Chemistry & Engineering,* 2(5)**,** 1312-1317.

MUJUMDAR, A. S. 2006. *Handbook of industrial drying.* USA, New York: CRC Press, 93-95.

NAGARAJAN, S., CHEN, W. H. & CHIN, B. A. 1989. Infrared sensing for adaptive arc welding. *Welding Journal,* 68(11)**,** 462-466.

NOLÄNG, B. 2004. *Ekvi System 3.2,* BeN Systems, Balinge, Sweden.

NORGROVE, A. H. C., JONES, A. F. & KING-HELE, J. A. 1994. Effects of axial heat conduction in the metal wall of a detonator delay element. *Combustion Science and Technology,* 97(4-6)**,** 449-468.

POURMORTAZAVI, S. M., HAJIMIRSADEGHI, S. S., KOHSARI, I., FATHOLLAHI, M. & HOSSEINI, S. G. 2008. Thermal decomposition of pyrotechnic mixtures containing either aluminum or magnesium powder as fuel. *FUEL,* 87(2)**,** 244-251.

RAGHU, O. & PHILIP, J. 2006. Thermal properties of paint coatings on different backings using a scanning photo acoustic technique. *Measurement Science and Technology,* 17**,** 2945-2949.

RICCO, I. M. M., FOCKE, W. W. & CONRADIE, C. 2004. Alternative oxidants for silicon fuels in time-delay compositions. *Combustion Science and Technology,* 176(9)**,** 1565-1575.

RUGUNANAN, R. A. & BROWN, M. E. 1991. Reactions of powdered silicon with some pyrotechnic oxidants. *Journal of Thermal Analysis,* 37**,** 1193-1211.

RUGUNANAN, R. A. & BROWN, M. E. 1994. Combustion of binary and ternary silicon/oxidant pyrotechnic systems, Part IV: Kinetic aspects. *Combustion Science and Technology,* 95(1)**,** 117-138.

SARAWADEKAR, R. G. & AGRAWAL, J. P. 2008. Nanomaterials in pyrotechnics. *Defence Science Journal,* 58(4)**,** 486-495.

SHAMSIPUR, M., POURMORTAZAVI, S. M., ROUSHANI, M. & BEIGI, A. A. M. 2013. Thermal behavior and non-isothermal kinetic studies on titanium hydride-fueled binary pyrotechnic compositions. *Combustion Science and Technology,* 185(1)**,** 122-133.

SHIMIZU, A. & HAO, Y. 1997. Influence of particle contact on the estimation of powder reaction kinetics of binary mixtures. *Journal of the American Ceramic Society,* 80(3)**,** 557-568.

SHKADINSKII, K. G. 1971. Transition to steady-state combustion of gasless compositions ignited by a hot surface. *Fizika Goreniya i Vzryva,* 7(3)**,** 332-336.

SHKADINSKII, K. G., KHAIKIN, B. I. & MERZHANOV, A. G. 1971. Propagation of a pulsating exothermic reaction front in the condensed phase. *Combustion, Explosion and Shock Waves,* 7(1)**,** 15-22.

STRUNINA, A. G., FIRSOV, A. N. & KOSTIN, S. V. 1981. Transition modes in the combustion of heterogeneous systems with solid-phase products. *Fizika Goreniya i Vzryva,* 17(5)**,** 24-30.

STRUNINA, A. G., MARTEM'YANOVA, T. M., BARZYKIN, V. V. & ERMAKOV, V. I. 1974. Ignition of gasless systems by a combustion wave. *Fizika Goreniya i Vzryva,* 10(4)**,** 518-526.

SULACSIK, L. 1974. Thermal analysis of pyrotechnical mixtures II: Study of the mechanism of the reaction of MnO_2 + Pb_3O_4. *Journal of Thermal Analysis,* 6**,** 215-220.

SWANEPOEL, D., DEL FABBRO, O. & FOCKE, W. W. 2010. Manganese as fuel in slow-burning pyrotechnic time delay compositions. *Propellants, Explosives, Pyrotechnics,* 35**,** 105-113.

THURESON, G. R. & GLADDEN, E. L. 1988. *Nonelectric blasting initiation signal control system, method and transmission device thereof*. USA, US4757764.

TICHAPONDWA, S. M., FOCKE, W. W., DEL FABBRO, O., GISBY, J. & KELLY, C. 2016. A comparative study of Si-$BaSO_4$ and Si-$CaSO_4$ pyrotechnic time-delay compositions. *Journal of Energetic Materials*, 34(3)**,** 342-356.

TICHAPONDWA, S. M., FOCKE, W. W., DEL FABBRO, O. & KELLY, C. 2010. Calcium sulfate as a possible oxidant in "green" silicon-based pyrotechnic time delay compositions. *Propellants, Explosives, Pyrotechnics,* 35**,** 1-9.

TSANG, D. K. L. 2005. The initiation process inside a detonation delay element. *International Journal of Applied Mathematics and Mechanics,* 2**,** 12-39.

VERMEIJ, E., DUVALOIS, W., WEBB, R. & KOEBERG, M. 2009. Morphology and composition of pyrotechnic residues formed at different levels of confinement. *Forensic Science International,* 186(1)**,** 68-74.

WEATHERBASE. Available: www.weatherbase.com [Accessed 6 November 2017].

YAGODNIKOV, D. A., IGNATOV, A. V. & GUSACHENKO, E. I. 2017. Ignition and combustion of pyrotechnic compositions based on microsized and ultra-nanosized aluminum particles in a moist medium in a two-zone gas generator. *Combustion, Explosion and Shock Waves,* 53(1)**,** 15-23.

YAWS, C. L. 2010. *Yaws' Thermophysical Properties of Chemicals and Hydrocarbons (Electronic Edition),* KNOVEL, Available: https://app.knovel.com.

YAWS, C. L. 2014. *Yaws' Critical Property Data for Chemical Engineers and Chemists (Electronic Edition),* KNOVEL, Available: https://app.knovel.com.

PUBLICATIONS

Journal Articles

Montgomery, Y. C., Focke, W. W., Atanasova, M., Del Fabbro, O. and Kelly, C. 2016. Mn + Sb_2O_3 thermite/intermetallic delay compositions. *Propellants, Explosives, Pyrotechnics,* 41(5), 919 – 925.

Montgomery, Y. C., Focke, W. W. and Kelly, C. 2017. Measurement and modelling of pyrotechnic time delay burn rates: Method and model development. *Propellants, Explosives, Pyrotechnics,* 42(10), 1161-1167.

Montgomery, Y. C., Focke, W. W. and Kelly, C. 2017. Measurement and modelling of pyrotechnic time delay burn rates: Application and Prediction of fast burning delay composition. *Propellants, Explosives, Pyrotechnics*, 42(11), 1289-1295.

Conference Papers Presented

Focke, W. W., Theron, Y. C., Haggard, E. L., Del Fabbro, O., Luyt, I. and Muller, I. 2012. Measuring time delay burn rates with an infrared camera. *The 38th International Pyrotechnics Seminar*, Westin Denver Downtown Hotel, Denver, Colorado, USA, 10-15 June 2012.

Montgomery, Y. C., Van der Westhuizen, A. and Focke, W. W. 2014. Measuring and modelling of burn rates in pyrotechnic time delay elements. *The 40th International Pyrotechnics Seminar*, DoubleTree by Hilton Hotel, Colorado Springs, Colorado, USA, 13-18 July 2014.

Montgomery, Y. C., Focke, W. W., Del Fabbro, O., Kelly, C. and Labuschagnè, G. 2016. The burning rate of Mn + MnO_2 and Mn + Sb_2O_3 delay compositions. *The 42nd International Pyrotechnics Seminar*, DoubleTree by Hilton Hotel, Grand Junction, Colorado, USA. 10-15 July 2016.

APPENDICES

APPENDIX A: DIFFRACTOGRAMS OF RAW MATERIALS

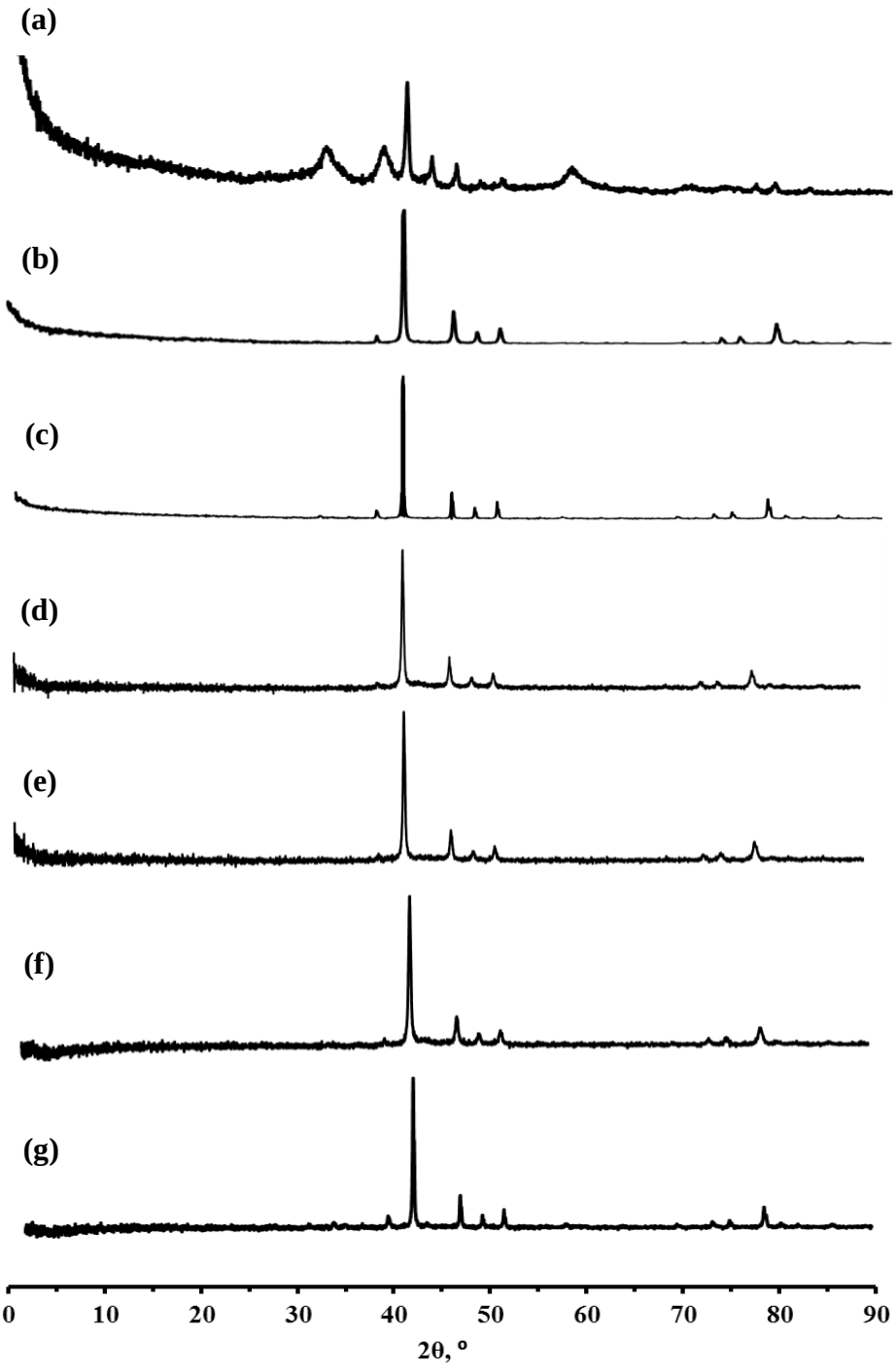

Figure A. 1: XRD diffractograms of samples (a) Mn_A, (b) Mn_B, (c) Mn_C, (d) Mn_D, (e) Mn_E, (f) Mn_F and (g) Mn_G/ Mn_H/ Mn_I

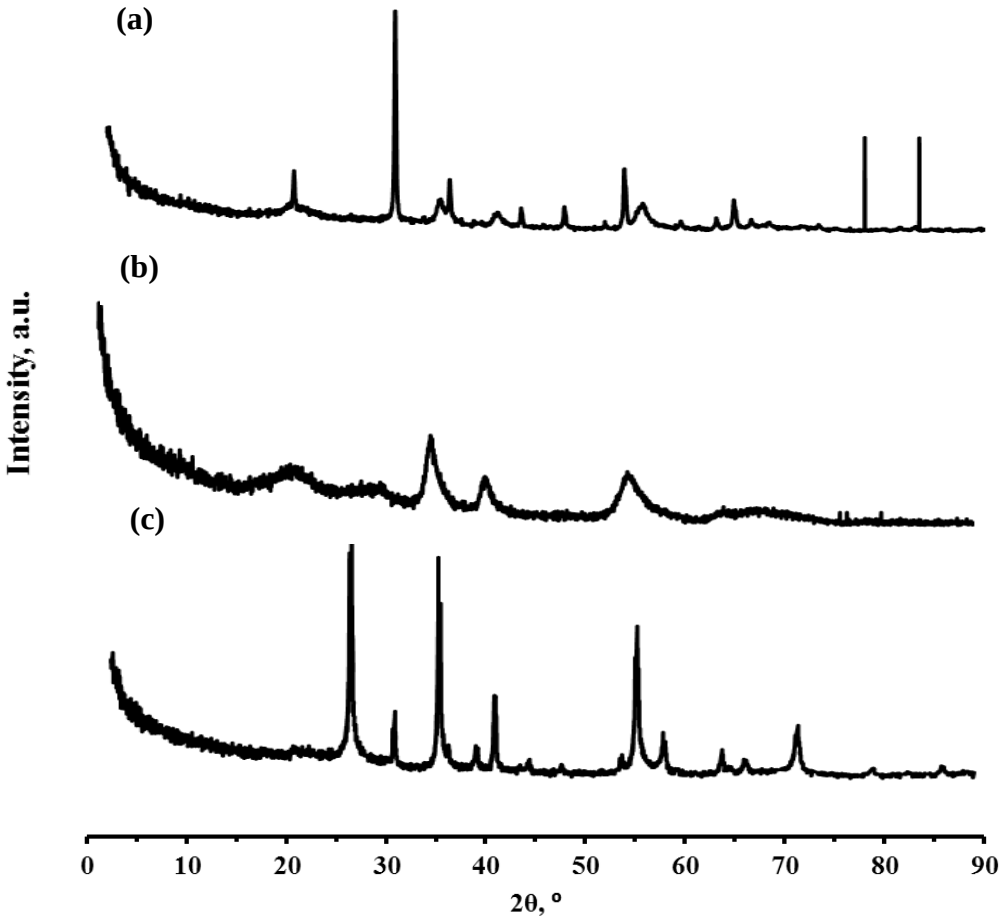

Figure A. 2: XRD diffractograms of samples (a) MnO_{2A}, (b) MnO_{2B} and (c) MnO_{2C}

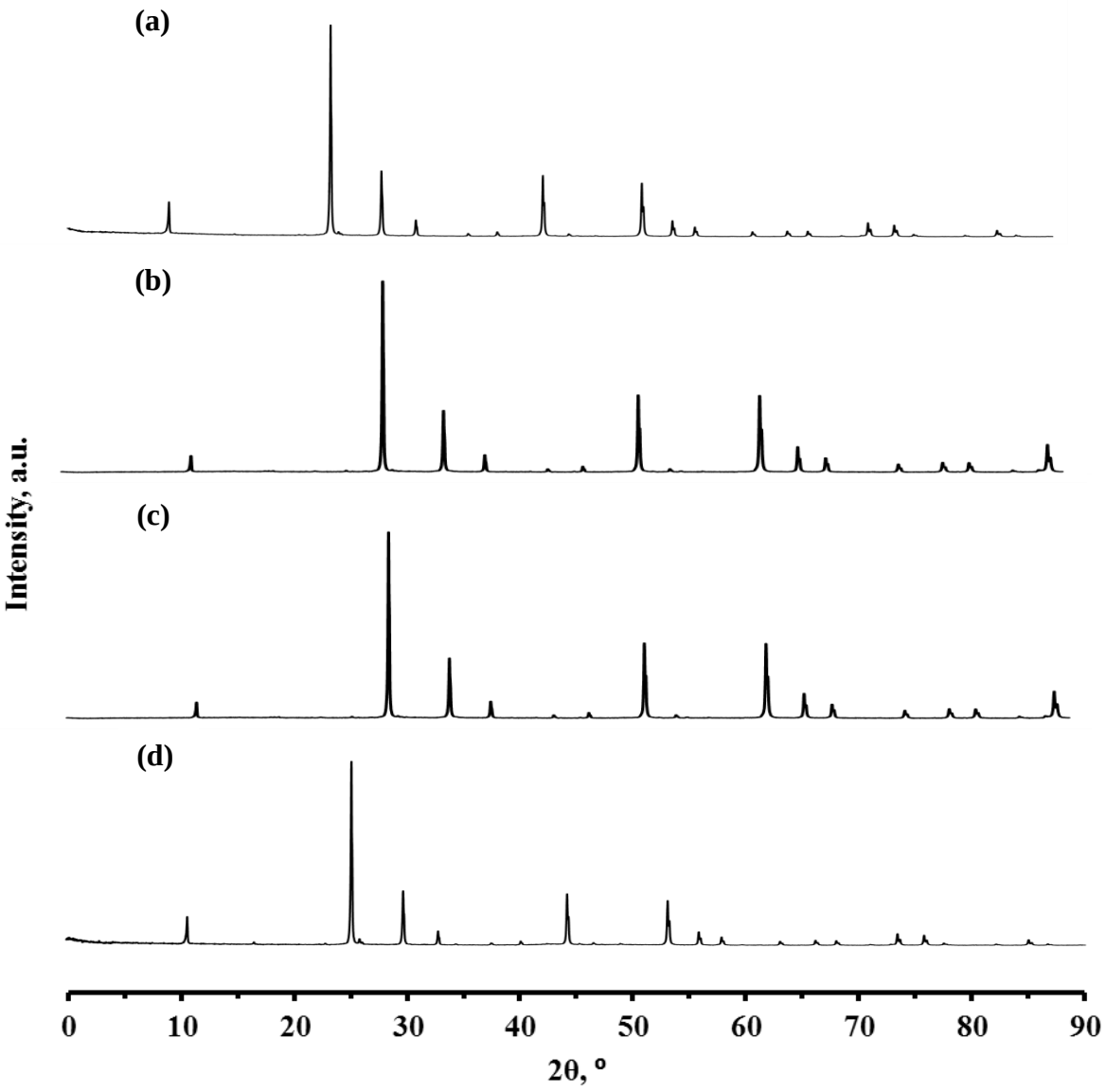

Figure A. 3: XRD diffractograms of samples (a) Sb_2O_{3A}, (b) Sb_2O_{3B}, (c) Sb_2O_{3C} and (d) Sb_2O_{3D}

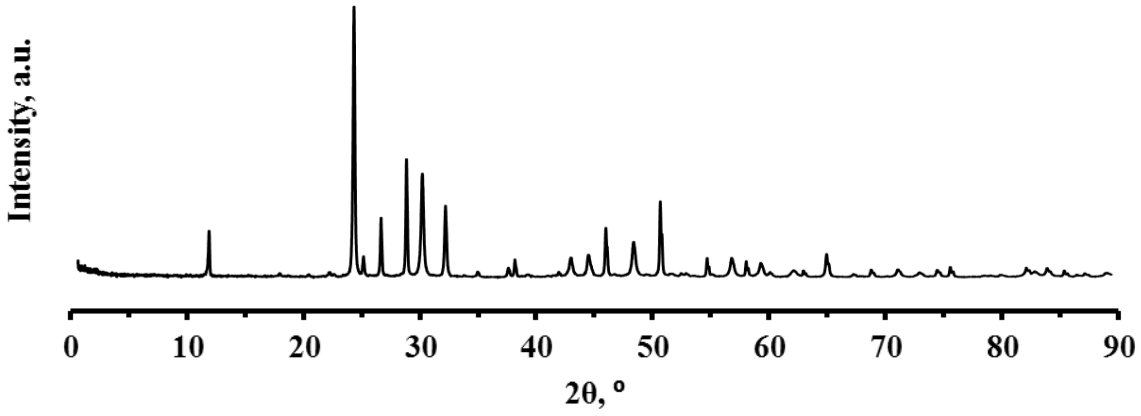

Figure A. 4: XRD diffractogram of sample Pb_3O_4

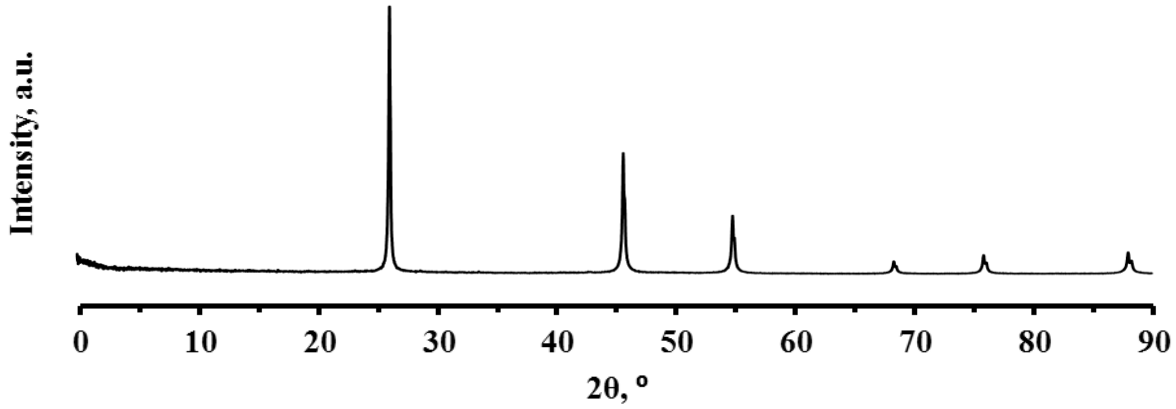

Figure A. 5: XRD diffractogram of sample Si

APPENDIX B: FESEM IMAGES OF RAW MATERIALS

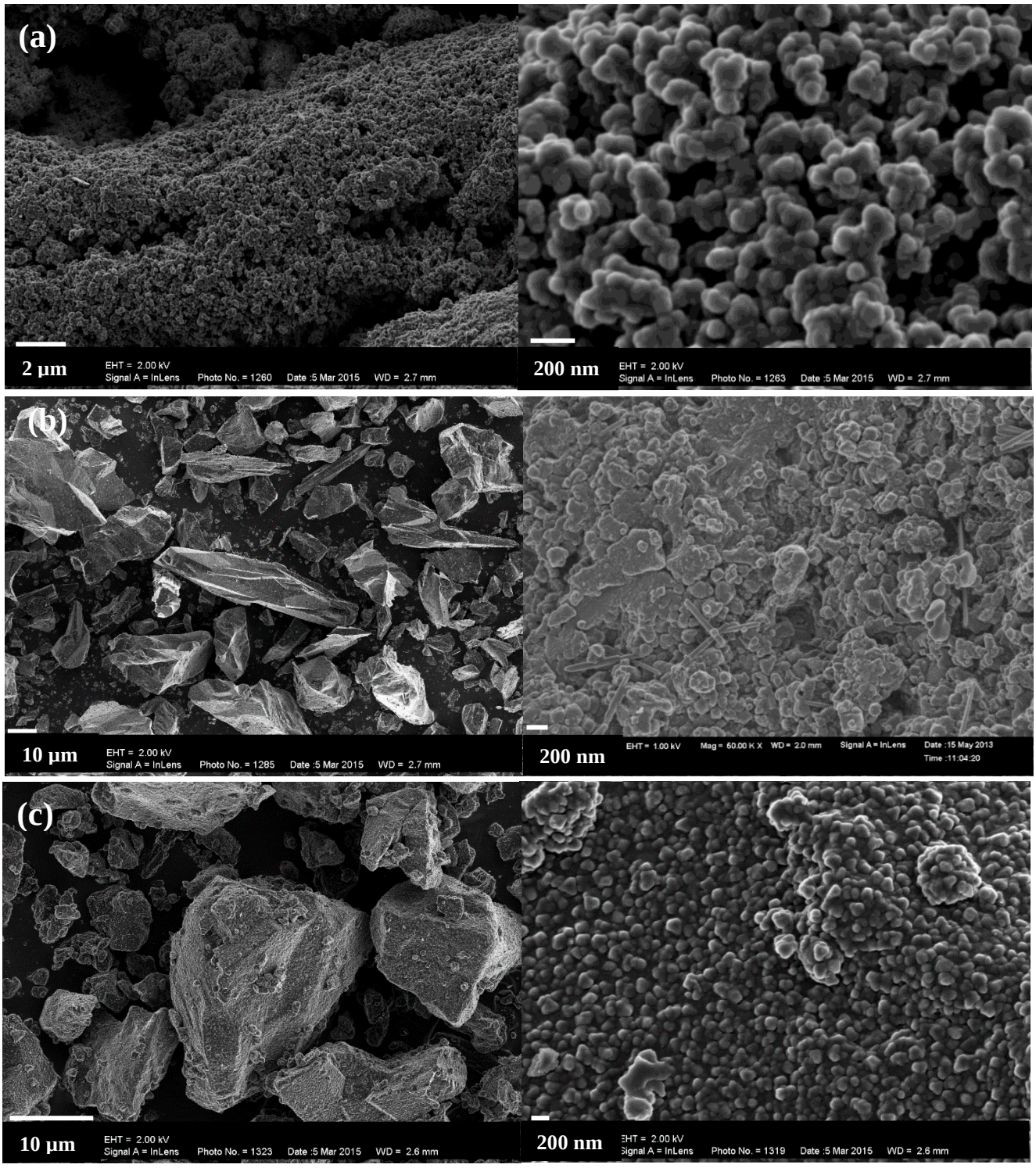

Figure B. 1: FESEM images of all the porous manganese samples (a) Mn_A, (b) Mn_B and (c) Mn_F

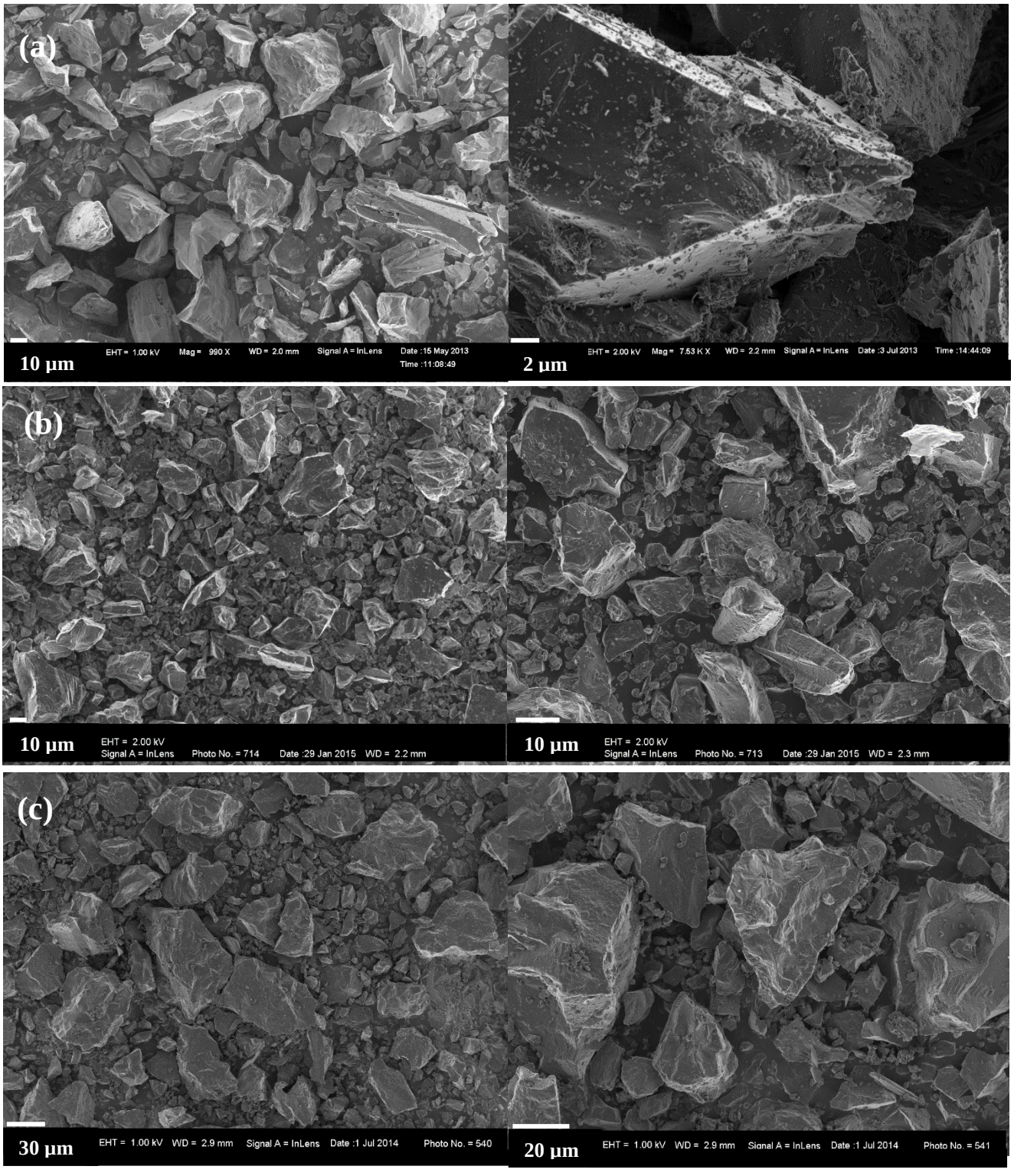
(a)
10 µm
EHT = 1.00 kV Mag = 990 X WD = 2.0 mm Signal A = InLens Date :15 May 2013 Time :11:08:49
2 µm
EHT = 2.00 kV Mag = 7.53 K X WD = 2.2 mm Signal A = InLens Date :3 Jul 2013 Time :14:44:09
(b)
10 µm
EHT = 2.00 kV Signal A = InLens Photo No. = 714 Date :29 Jan 2015 WD = 2.2 mm
10 µm
EHT = 2.00 kV Signal A = InLens Photo No. = 713 Date :29 Jan 2015 WD = 2.3 mm
(c)
30 µm
EHT = 1.00 kV WD = 2.9 mm Signal A = InLens Date :1 Jul 2014 Photo No. = 540
20 µm
EHT = 1.00 kV WD = 2.9 mm Signal A = InLens Date :1 Jul 2014 Photo No. = 541

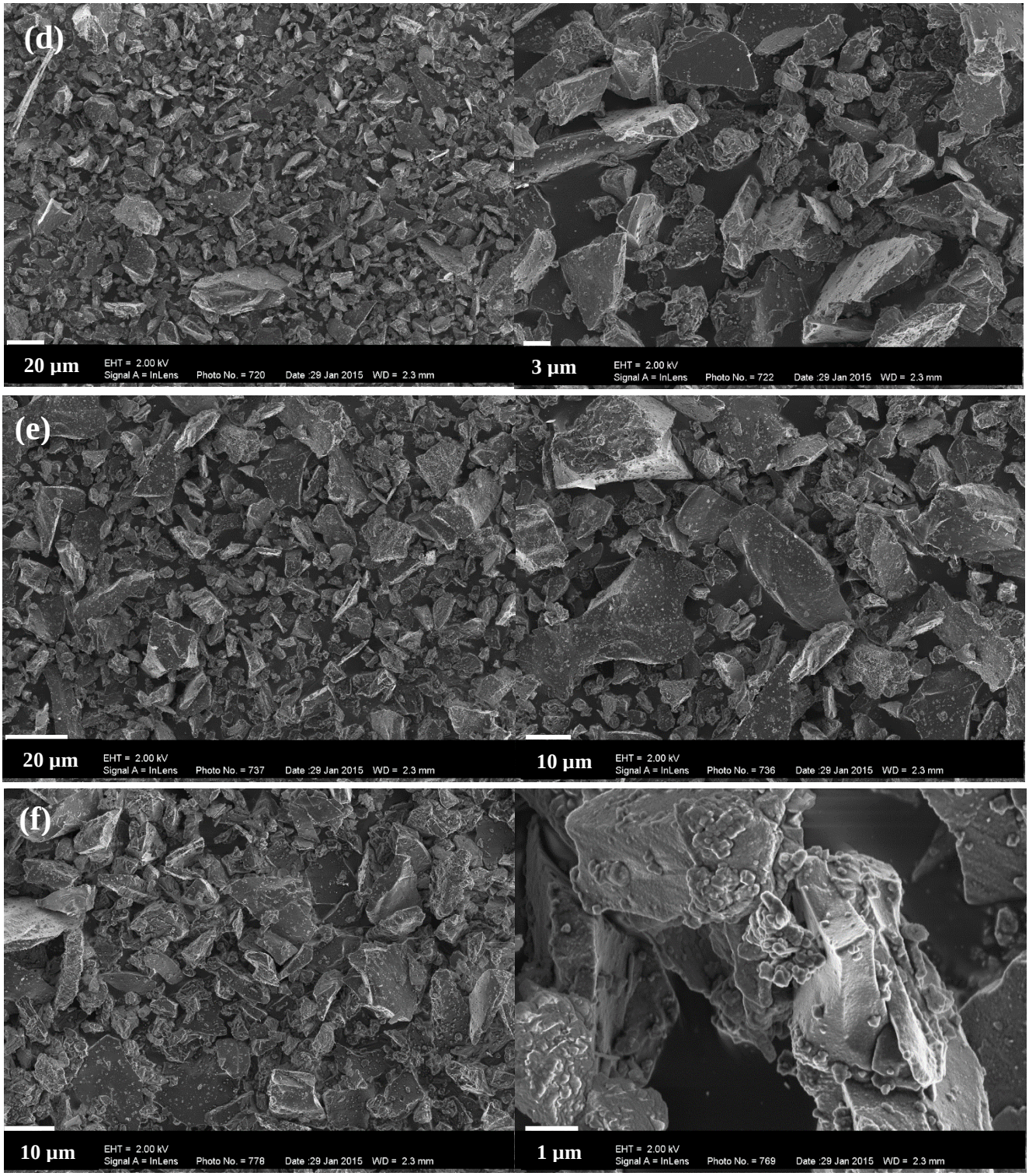

Figure B. 2: FESEM images of all the porous manganese samples (a) Mn_C, (b) Mn_D, (c) Mn_E, (d) Mn_G, (e) Mn_H and (f) Mn_I

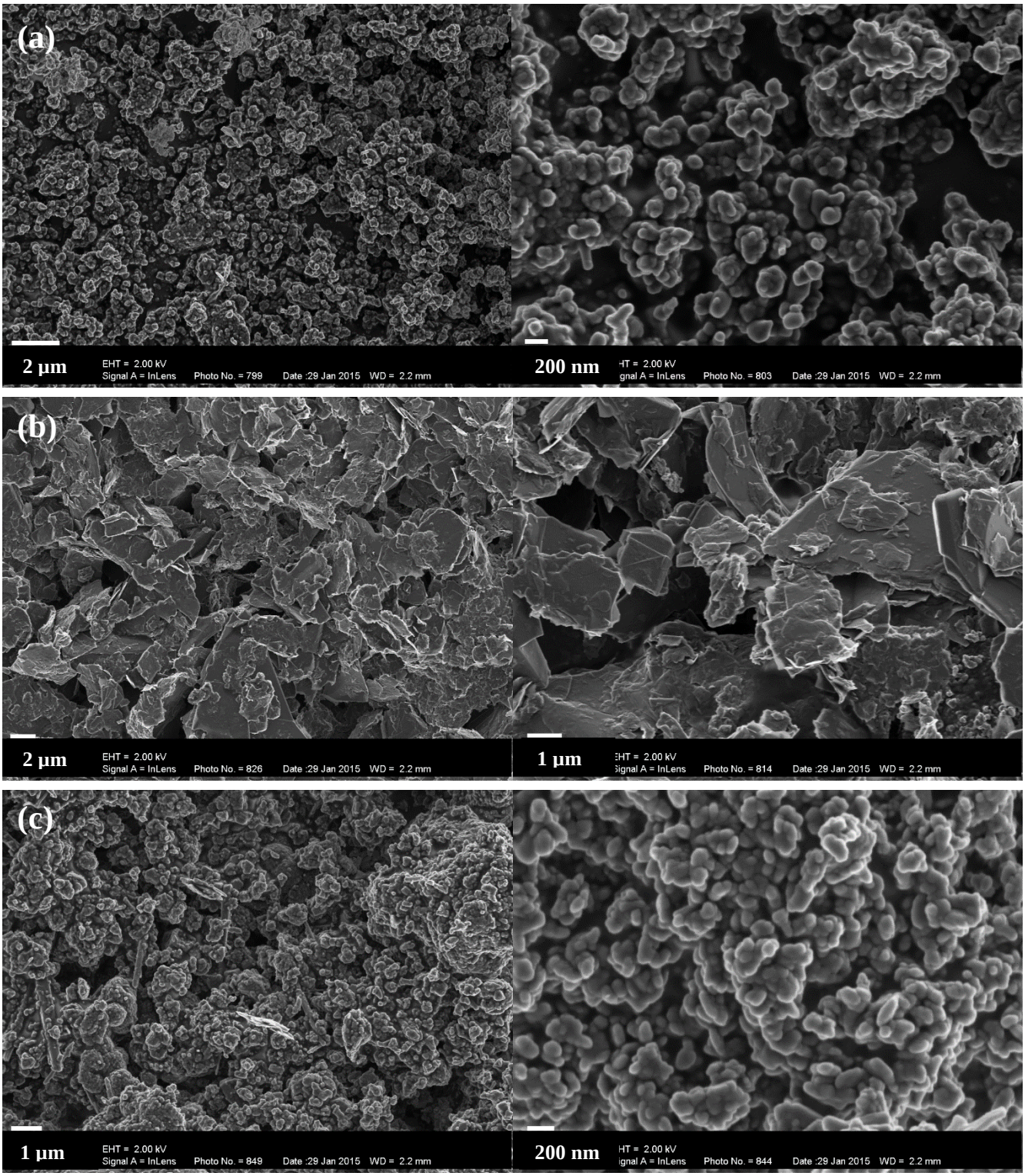

Figure B. 3: FESEM images of all the MnO_2 samples (a) MnO_{2A}, (b) MnO_{2B} and (c) MnO_{2C}

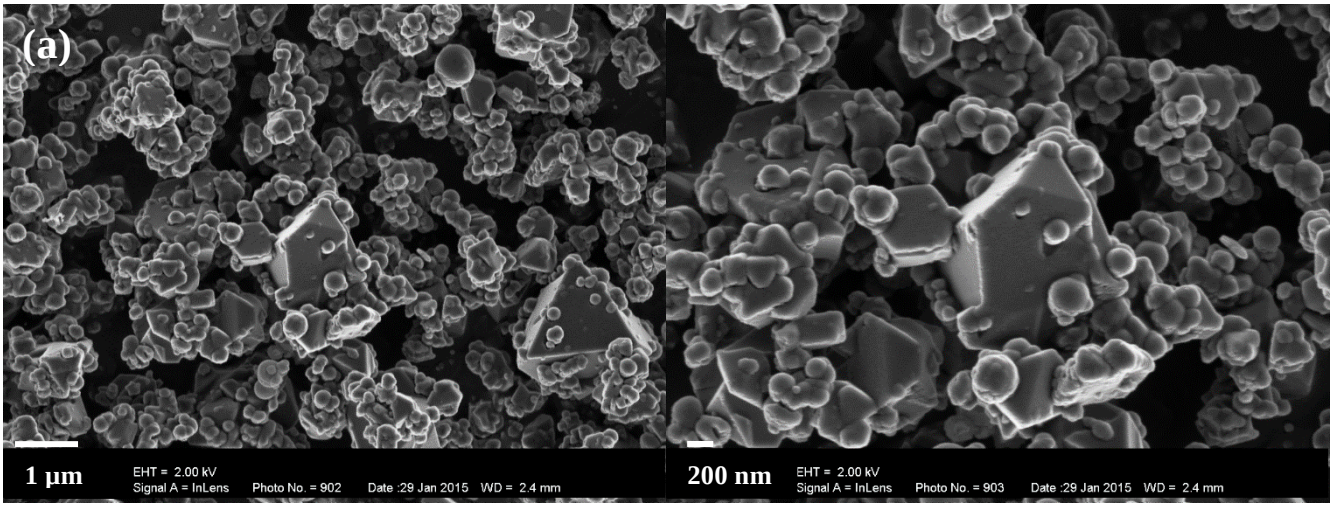
(a)
1 µm
EHT = 2.00 kV
Signal A = InLens
Photo No. = 902
Date :29 Jan 2015
WD = 2.4 mm
200 nm
EHT = 2.00 kV
Signal A = InLens
Photo No. = 903
Date :29 Jan 2015
WD = 2.4 mm

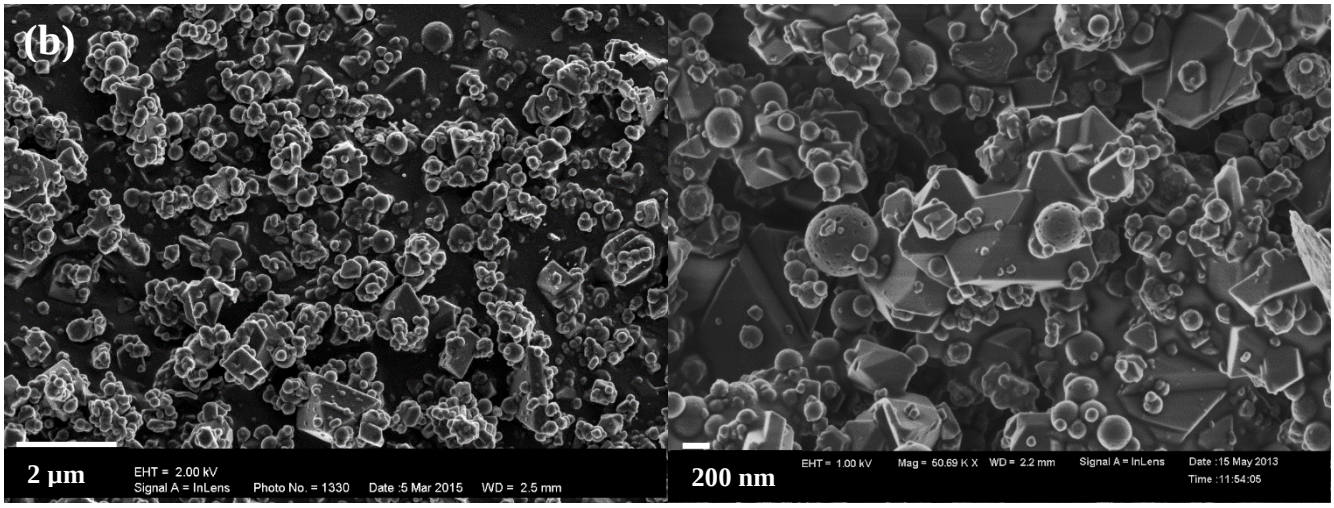
(b)
2 µm
EHT = 2.00 kV
Signal A = InLens
Photo No. = 1330
Date :5 Mar 2015
WD = 2.5 mm
200 nm
EHT = 1.00 kV
Mag = 60.69 K X
WD = 2.2 mm
Signal A = InLens
Date :15 May 2013
Time :11:54:05

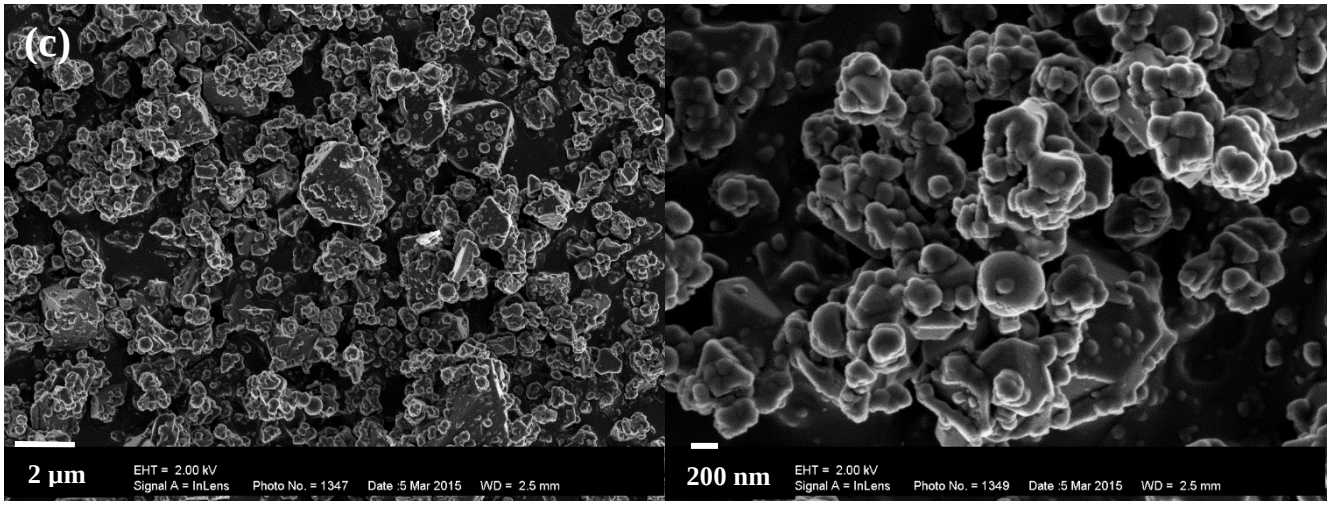
(c)
2 µm
EHT = 2.00 kV
Signal A = InLens
Photo No. = 1347
Date :5 Mar 2015
WD = 2.5 mm
200 nm
EHT = 2.00 kV
Signal A = InLens
Photo No. = 1349
Date :5 Mar 2015
WD = 2.5 mm

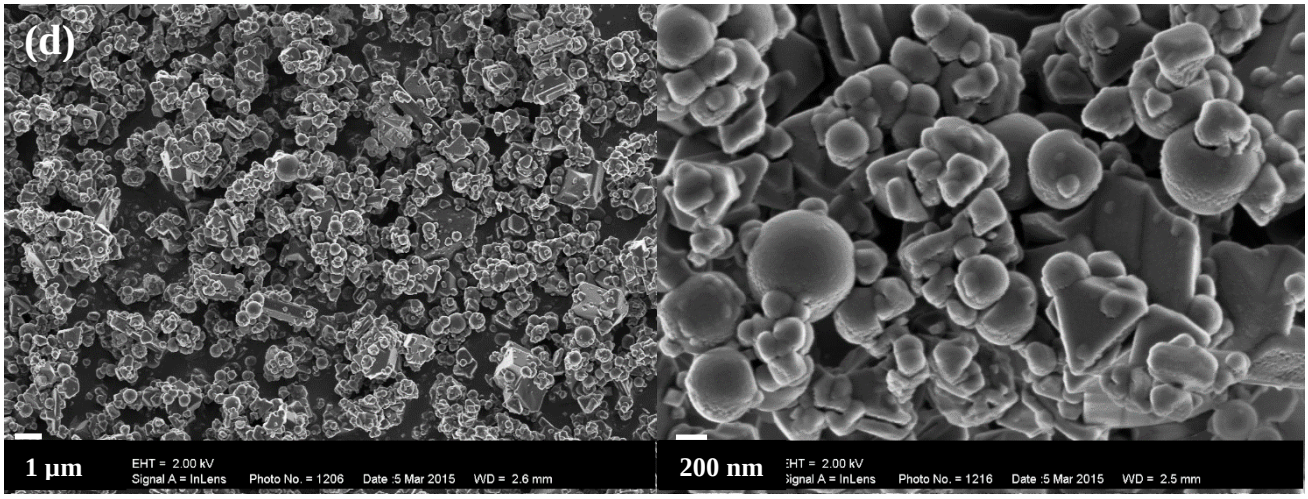

Figure B. 4: FESEM images of all the Sb_2O_3 samples with (a) Sb_2O_{3A}, (b) Sb_2O_{3B}, (c) Sb_2O_{3C} and (d) Sb_2O_{3D}

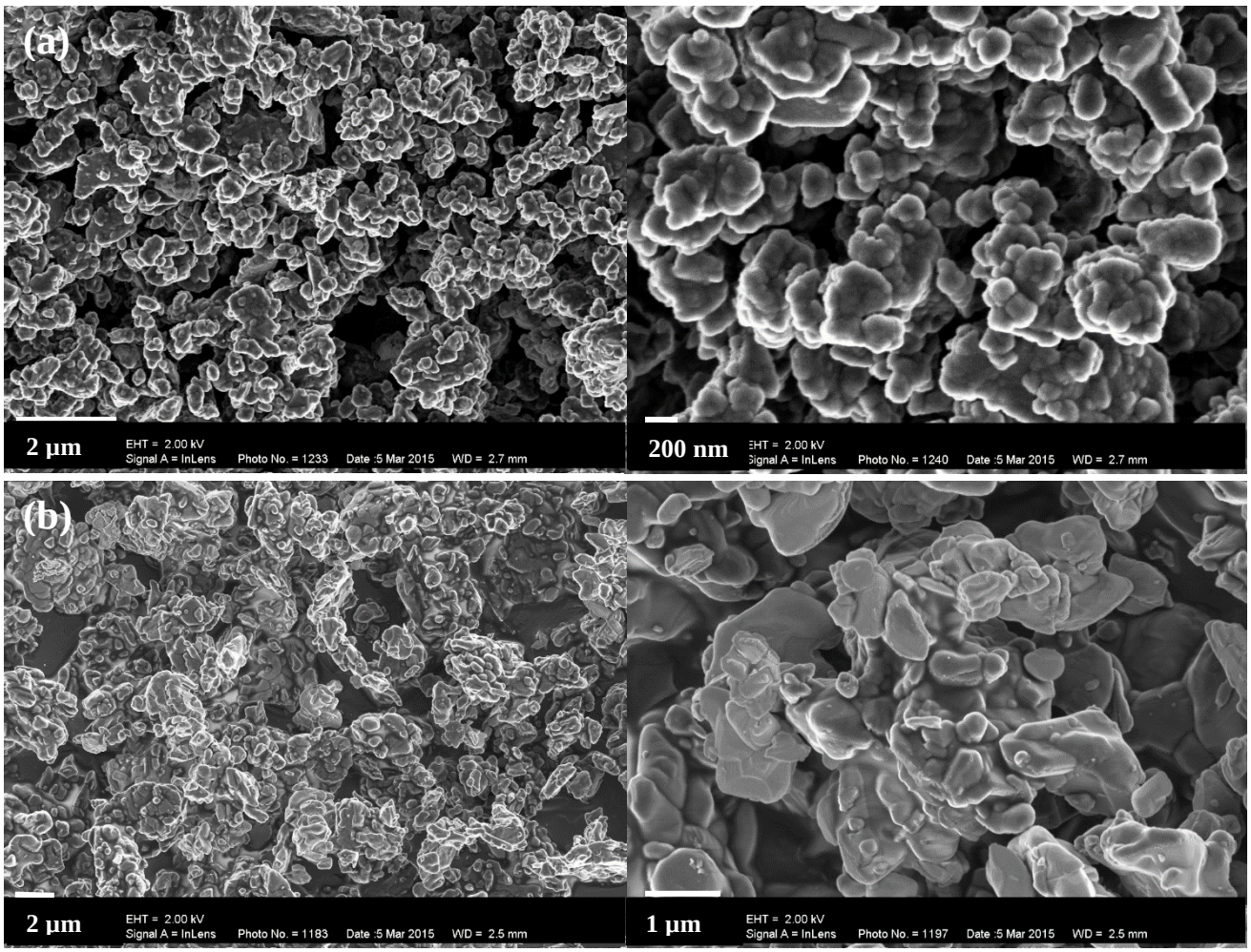

Figure B. 5: FESEM images of the silicon and red lead samples (a) Si and (b) Pb_3O_4

APPENDIX C: MATLAB CODES FOR DATA ANALYSIS

C.1 Data filtering

```
%IRdatafilter.m

load samplename.txt
  data = samplename
  numberofframes = length(data(1,:));
  numberofpixels = length(data(:,1));

  for m = 1:numberofframes
    a = 1;
    for n = 2:(numberofpixels-1);
      newdata(a,m) = (data(n-1,m)+data(n,m)+data(n+1,m))/3;
      a = a+1;
    end
  end
  save('filtereddatasamplename','newdata');
```

C.2 Average burn rate calculation

```
%averageburnrate.m

  frame1 =  %input('number of frame 1 = ')
  frame2 =  %input('number of frame 2 = ')
  Tracetemp = input('choose temperature = ')
  numberofframes = frame2-frame1;

  load -mat filtereddatasamplename;
  data = newdata
  numberofpixels = length(data);

 pixelvalue = 0.206;      %mm/pixel
                          %for 160mm from camera pixelvalue = 0.22
                          %For 250mm from camera pixelvalue = 0.349
                          %For 150mm from camera pixelvalue = 0.206
  framevalue = 0.02       %s/frame

n = 1;
  a = 1;
  for k = 1:numberofpixels
    T = data(k,n);
    if T<Tracetemp
      b = 0;
    else
      pixelfound(a,n) = k;
      a = a+1;
    end
  end

n = 2;
```

```
  a = 1;
  for k = 1:numberofpixels
    T = data(k,n);
    if T<Tracetemp
      b = 0;
    else
      pixelfound(a,n) = k;
      a = a+1;
    end
  end



pixelstraveled = pixelfound(1,1)-pixelfound(1,2)
distance = pixelstraveled*pixelvalue
time = numberofframes*framevalue
averageburnrate = distance/time
```

C.3 Instantaneous velocity profile calculations

```
%Instantaneousvelocityprofile.m

function instantaneousvelocityprofile
  clear all
  close all

  data = load("Allframesfiltered.txt");

  numberofframes = length(data(1,:))
  numberofpixels = length(data(:,1))

  pixelvalue = 0.349     %mm/pixel
                         %pixelvalue for 160mm from camera = 0.22
                         %pixelvalue    for    250mm    from    camera
pixelvalue = 0.349
                          %pixelvalue for 15mm from camera = 0.206
  framevalue = 0.02

  Tracetemp = input("Tracetemp")
  a = 1;
  for n = 1:numberofframes;
    i = 1;
    count = n;
    k = 0;
    while k < 1;
      Temp = data(i,n);

      if i == numberofpixels;
        if Temp < Tracetemp;
            k = 2;
        else
          placevalue(a,1) = i;
```

```
        placevalue(a,2) = n;
        a = a+1;
        k = 2;
      end

    else
        if  Temp < Tracetemp;
          i = i+1;
          k = 0;
        else
          placevalue(a,1) = i;
          placevalue(a,2) = n;
          a = a+1;
          k = 2;
        end
    end
  end
end
placevalue;
a = 1;
i = 2;
b = 1;
x = 1;
placevaluecut1 = [];
placevaluecut2 = [];
while x < (length(placevalue(:,1))-3)
  same = placevalue(x,1) - placevalue((x+5),1);
  x;

   if same ==0
      if (placevalue(x-1,1)-placevalue(x,1) )< 0
        x = x+1
      else
        placevaluecut1(:,1) = placevalue((1:x),1);
        placevaluecut2(:,1) = placevalue((1:x),2);
        x = (length(placevalue(:,2))-2);

      end

    else
    x = x+1;
  end
end
valuematrix = [];

valuematrix(:,1) = placevaluecut1(:,1);
valuematrix(:,2) = placevaluecut2(:,1);
valuematrix;

for v = 1:(length(valuematrix)-1);
  distance(v) = (valuematrix(v,1)-valuematrix(v+1,1))*pixelvalue;
  time(v) = (valuematrix(v+1,2)-valuematrix(v,2))*framevalue;
end

for w = 1:(v-1);
instvel(w,1) =distance(w)./time(w) ;
```

```
  distmatrix(w,1)                 =                 (valuematrix(1,1)-
valuematrix(w+1,1))*pixelvalue;
  end

  totaldistance                   =                 (valuematrix(3,1)-
valuematrix((length(valuematrix)-2),1))*pixelvalue;
  totaltime         =         (valuematrix((length(valuematrix)-2),2)-
valuematrix(3,2))*framevalue;
  averagespeed = totaldistance/totaltime
  for u = 1:(length(distmatrix));
    averagematrix(u) = averagespeed;
  end


  figure(1)

plot(distmatrix,instvel,'r',distmatrix,averagematrix,'k',distmatrix,
instvel,'or')
  hold off

  save("instvel.text","instvel")
  save("distance.text","distmatrix")
end
end
```

APPENDIX D: XRD RESULTS OF PRODUCT RESIDUES

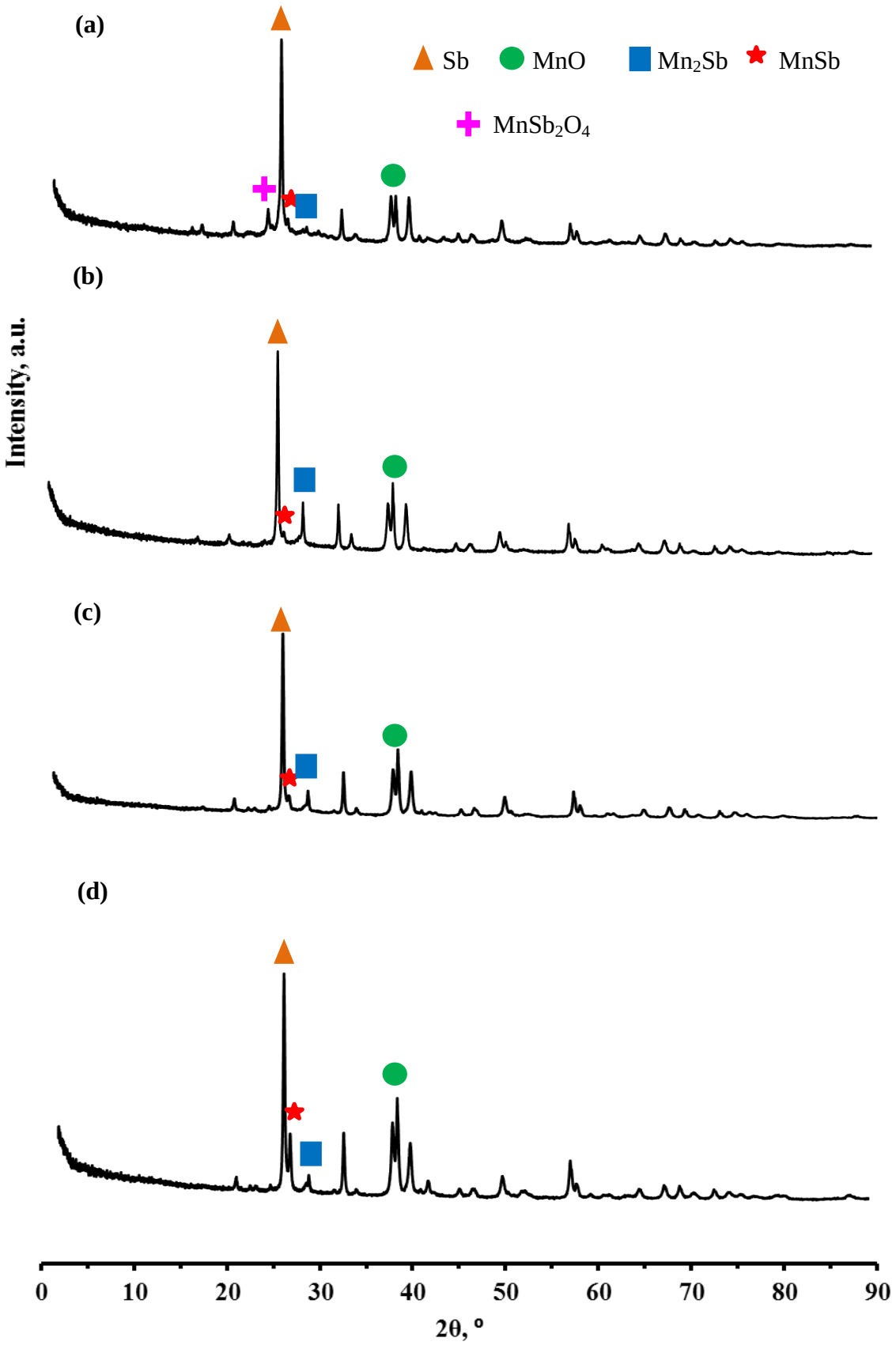

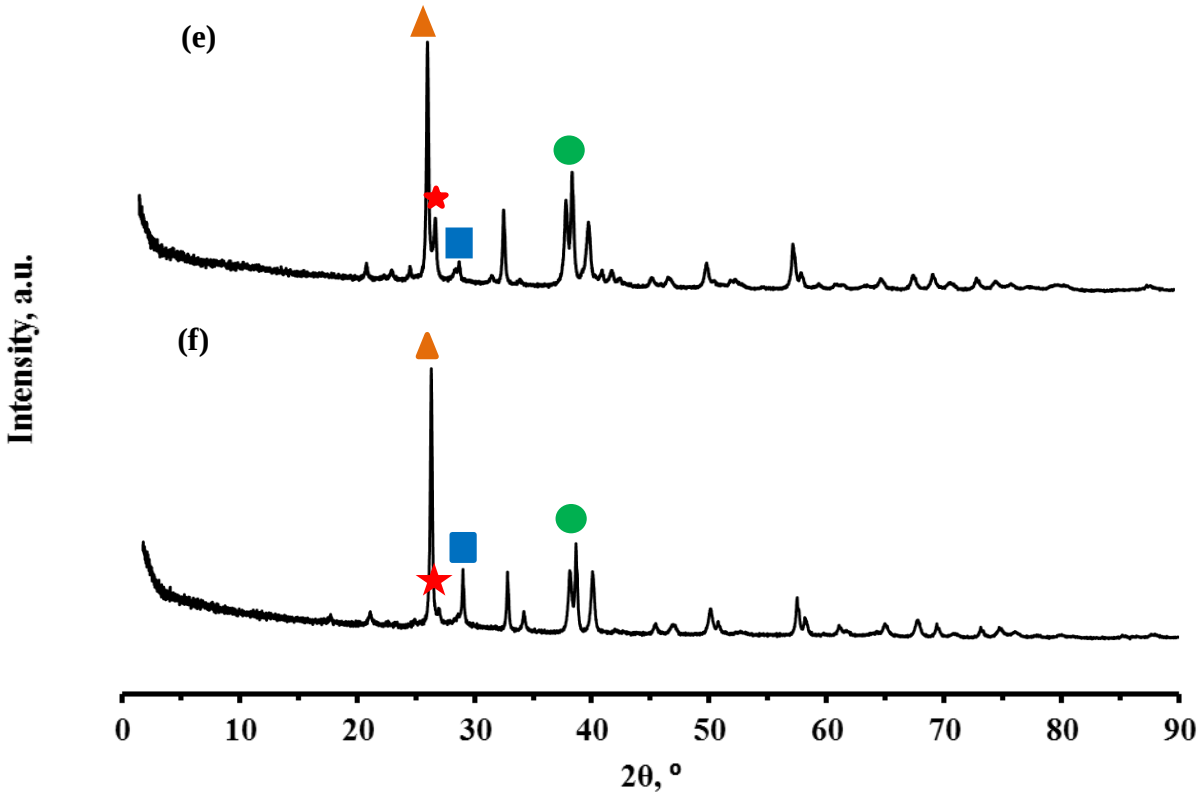

Figure D. 1: XRD diffractograms of the residues obtained after burning the Mn + Sb_2O_3 composition originally containing (a) 25 wt.%, (b) 30 wt.%, (c) 35 wt.%, (d) 40 wt.%, (e) 45 wt.% and (f) 50 wt.%

APPENDIX E: THERMOPHYSICAL PROPERTIES OF MATERIALS USED IN THE NUMERICAL MODEL

E.1 Thermal conductivities

.

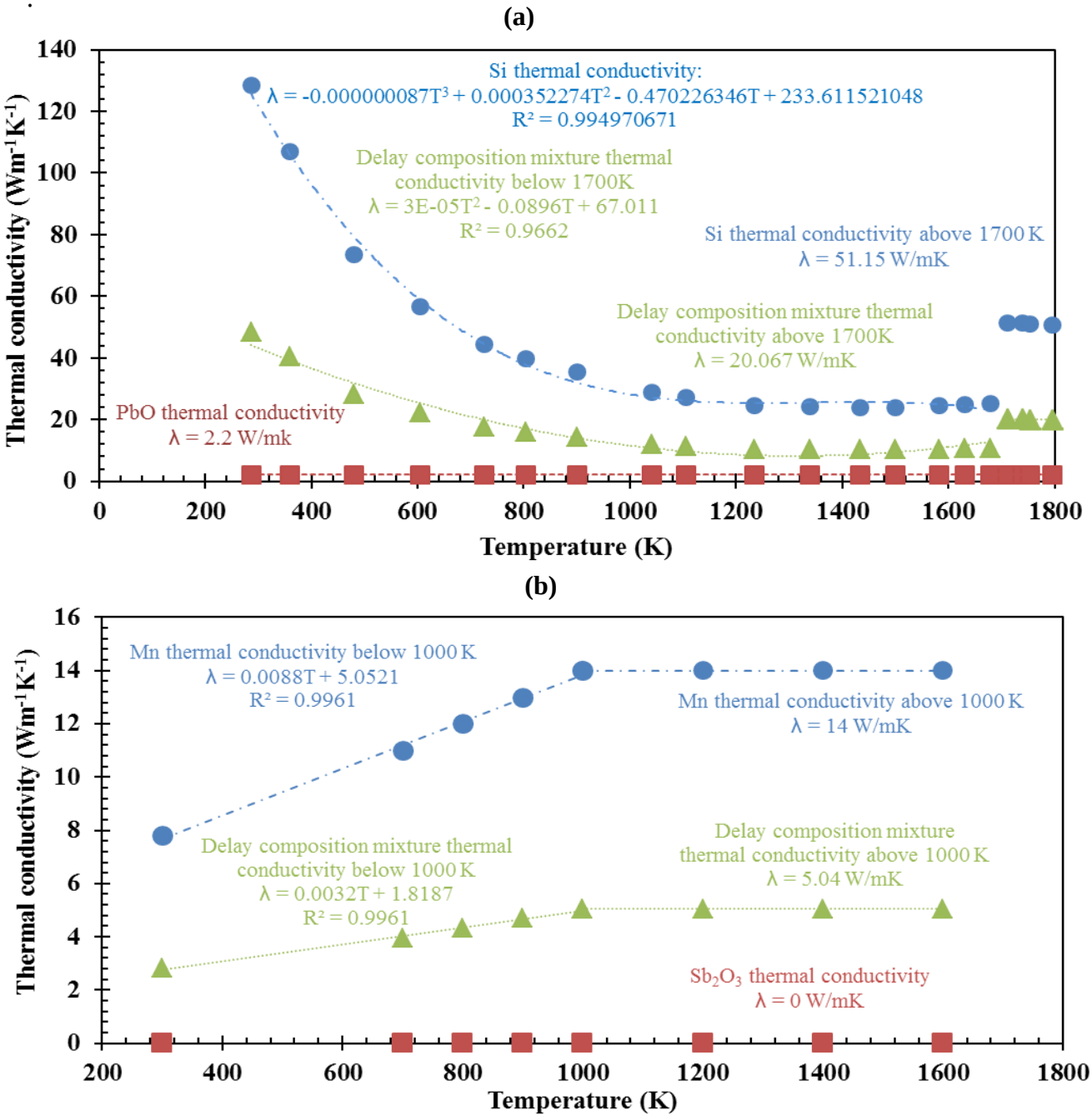

Figure E. 1: The thermal conductivity derived for the delay composition mixtures from (a) Pb_3O_4 and Si as temperature-dependent parameters represented by Equation 4-7 and (b) Sb_2O_3 and Mn represented in Equation 4-8 (Magomedov and Gadjiev, 2008, Anisimova et al., 2004, International Atomic Energy Agency, 2008)

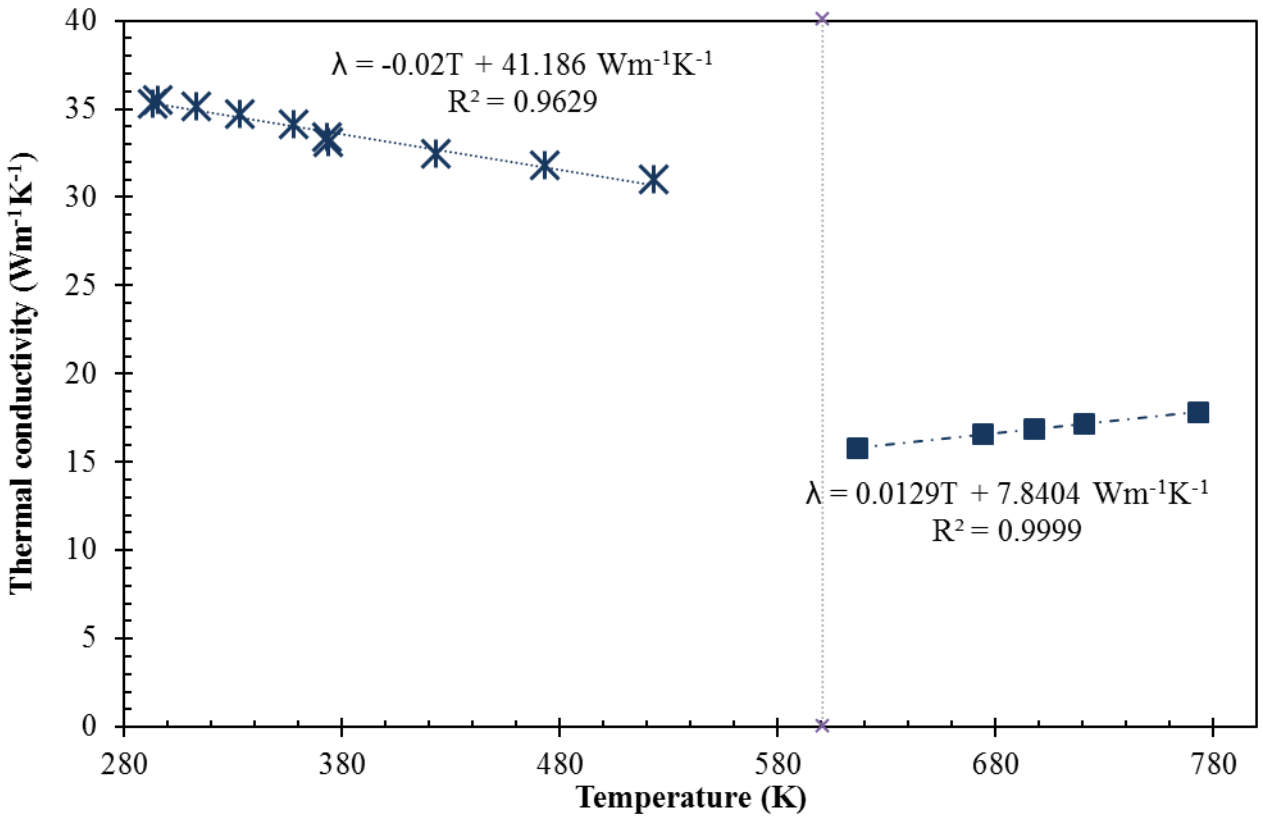

Figure E. 2: Thermal conductivity of the lead tube wall containing the experimental literature values as presented in Equation 4-16 (Hemminger, 1989)

E.2 Specific heat capacities

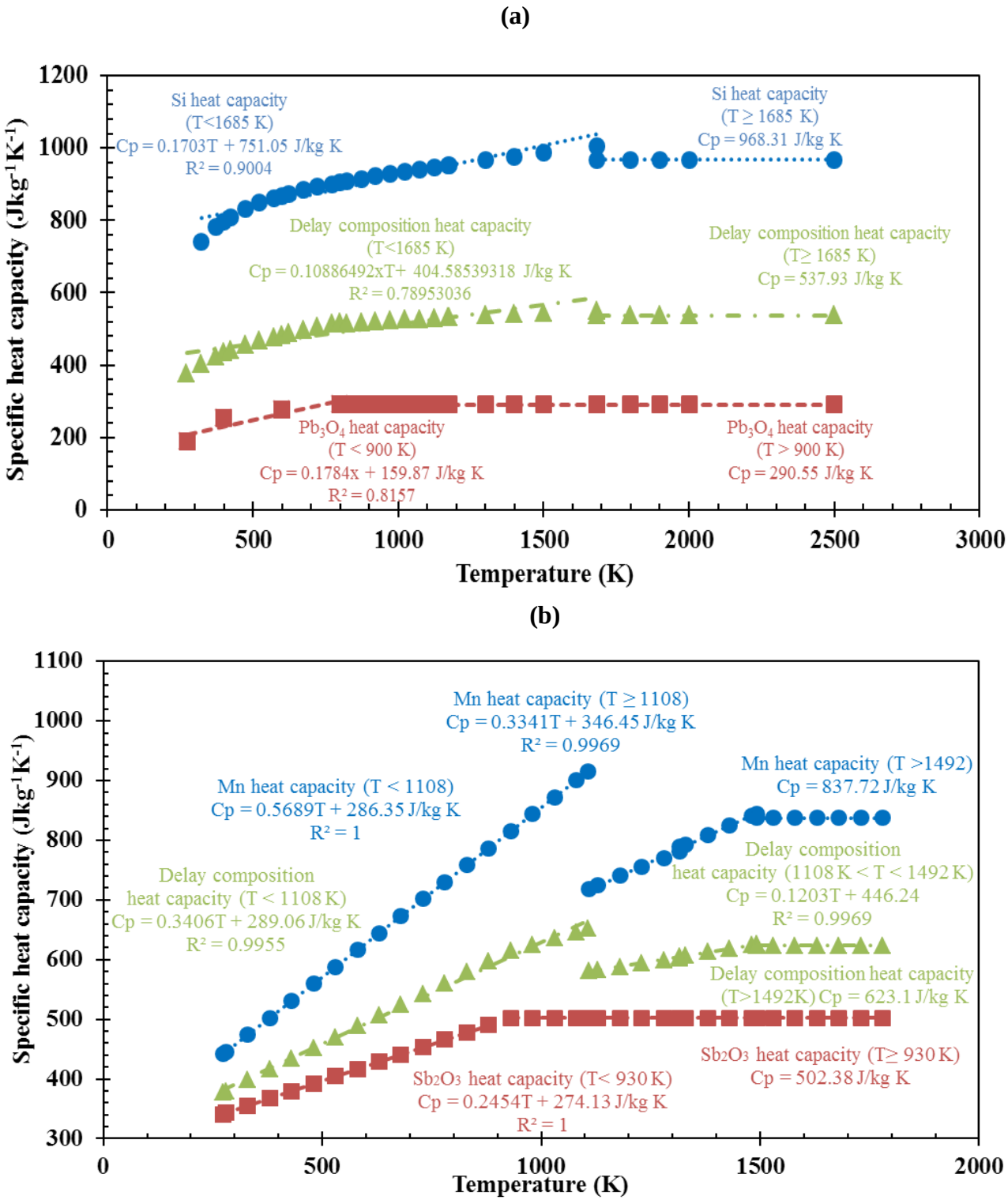

Figure E. 3: Derivation of the heat capacity for mixed delay compositions from the straight line mixing rule between the heat capacities of (a) Si (Green and Perry, 2008) and Pb_3O_4 (Chase et al., 1974) and (b) Mn (Green and Perry, 2008) and Sb_2O_3 (Green and Perry, 2008)

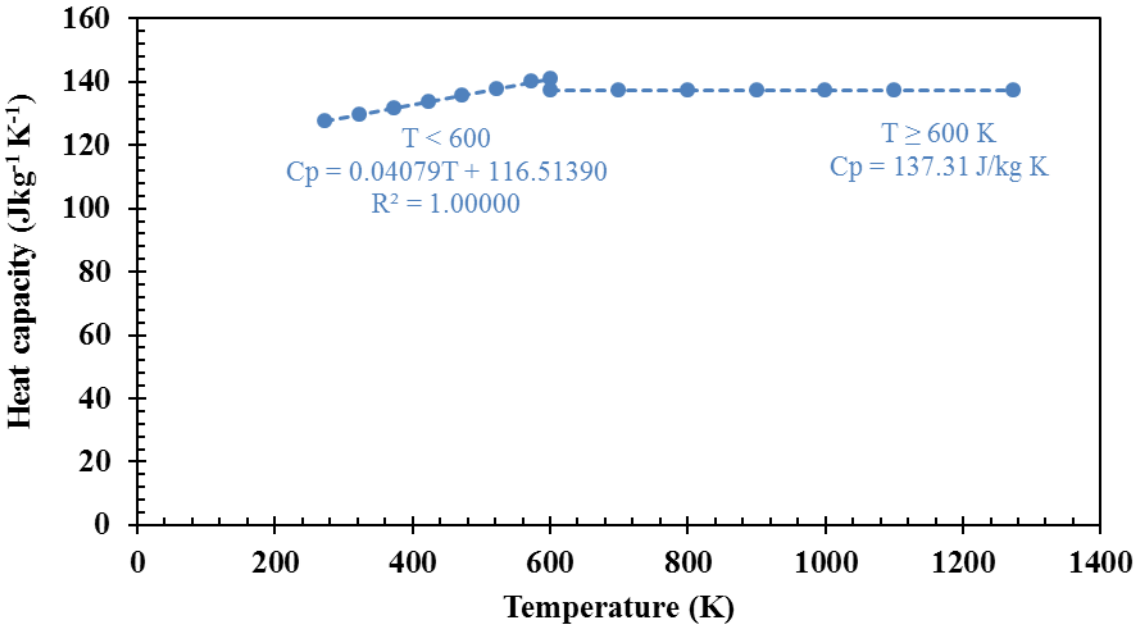

Figure E. 4: Derivation of the heat capacity for the lead tube material (Green and Perry, 2008).

APPENDIX F: VALUES OF PHYSICAL PROPERTIES USED IN THE NUMERICAL MODEL

Table F-1: Thermal properties used for solving the energy balance

Property	**$Mn+Sb_2O_3$ model**	**$Si+Pb_3O_4$ model**	**Source**
ρ_{comp}	5 920 kg/m^3	6 654.5 kg/m^3	(Green and Perry, 2008)
$\mathfrak{H}$	0.58	0.58	(WeatherBase)
ρ_{paint}	1 162 ± 34 kg/m^3	1162 ± 34 kg/m^3	(Raghu and Philip, 2006)
Cp_{paint}	2 835 ± 283 J/kgK	2 835 ± 283 J/kgK	(Raghu and Philip, 2006)
λ_{paint}	0.57 ± 0.05 W/mK	0.57 ± 0.05 W/mK	(Raghu and Philip, 2006)
ε_{paint}	0.98	0.98	(Cengel, 2006)
ℓ	100 mm	100 mm	Experimental
D_{inside}	2.803 mm	2.625 mm	Experimental
$D_{outisde}$	6.4 mm	6.4 mm	Experimental
$\rho_{packing}$	4 006.45 kg/m^3	2 388.93 kg/m^3	Experimental
φ_s	0.693	0.559	Experimental

APPENDIX G: BURN RATE MEASUREMENT RESULTS

Table G- 1: Results from the burn rate analysis study.

Composition [b)]	**Detonator Burn Rate ± Std (mms^{-1})**	**IR Camera Burn Rate ± Std (mms^{-1})**	**Thermocouple Burn Rate ± Std (mms^{-1})**
36% Mn + Sb_2O_3	6.95 ± 0.22	5.73 ± 0.22	5.47 ± 0.37
55% Si + Pb_3O_4	43.75 ± 0.87	40.70 ± 1.08	28.76 ± 2.11
50% Si + Pb_3O_4	86.93 ± 1.36	76.45 ± 1.90	59.05 ± 7.46
45% Si + Pb_3O_4	126.44 ± 1.79	113.87 ± 4.61	82.79 ± 12.88
40% Si + Pb_3O_4	156.79 ± 2.76	142.23 ± 2.50	120.91 ± 26.77
36% Si + Pb_3O_4	170.69 ± 2.13	149.05 ± 5.38	135.34 ± 1.02
30% Si + Pb_3O_4	175.55 ± 4.84	153.53 ± 4.12	120.38 ± 25.94

[b)] For each composition tested there were 6 samples tested using the industrial detonator burn test, 3 using the IR camera technique and 3 using the thermocouple technique.